

## **ABSTRACT**

ZAMBON, JOSEPH BRENDAN. *Air-Sea Interaction During Landfalling Tropical and Extra-Tropical Cyclones*. (Under the direction of Dr. Ruoying He).

Tropical and extra-tropical cyclones represent large, discrete events that result in drastic changes to the coastal shoreline, displacement of persons, damage to property and infrastructure, and deaths each year. The ability to accurately predict these events can provide advanced warnings and dramatically reduce their impacts. Several numerical models have been developed over the past 30 years that accurately model the individual environmental conditions in which these storms develop and thrive. However, these cyclones are dependent not only on the individual environmental conditions but also the interactions and feedbacks between them. Improvement to the prediction of tropical and extra-tropical cyclones, as well as the ocean environment in which they exist, is sought through development and implementation of a coupled modeling system, known as the Coupled Ocean-Atmosphere-Wave-Sediment Transport (COAWST) model.

In the first chapter, motivation and literature review is presented with the aim of demonstrating the importance of accurate prediction of the ocean, atmosphere, and wave environmental conditions in tropical and extra-tropical cyclone hindcast and forecast. Several analytical and numerical studies are researched in order to provide sufficient background into the problem, provide motivation into developing a coupled numerical model, and explain previous coupled numerical studies. Based on the existing state of knowledge, it is hypothesized that coupled modeling systems will provide improvement to the prediction of hurricane intensity, environmental states of surface waves and sea surface temperature, and atmospheric impact from precipitation distribution. This is demonstrated with 3 different tests of Hurricanes Ivan (2004), Sandy (2012), and Irene (2011).

In the second chapter, Hurricane Ivan (2004) is used as a test case for multiple uncoupled and coupled experiments into a model hindcast of the event. The methods of model coupling are presented with configurations of the uncoupled and coupled models detailed. Comparisons of simulated track, and intensity are evaluated, demonstrating improvement in prediction of the tropical cyclone intensity through coupling. The ocean and wave environments are also examined, with remote and *in situ* observations employed to show improvement with coupled applications. A heat budget is computed, based on the dynamics of the ocean model, drawing comparison to previous case studies cited in the first chapter that show the heat flux to the atmosphere is limited by the depth of the surface mixed layer with the ocean heat loss due to diffusion in shallower water and advection in deeper locations.

In the third chapter, Hurricane and Post-Tropical storm Sandy (2012) is demonstrated as a test case in order to examine coupling impacts on a storm undergoing extratropical transition. As in the Ivan case, verification data of track and intensity are used and a strength comparison is added. An examination of the environmental variables immediately prior to landfall is conducted in order to determine the relative importance of ocean coupling during extratropical transition. It is identified that in contrast to Ivan, coupling did not provide an increase in predictability of TC intensity, most likely due to the speed of the storm. But the coupling was significant to provide accurate wave simulations.

In the fourth chapter, Hurricane Irene (2011) is used as the experimental case. In this section, we demonstrate model performance through forecast (rather than hindcast) in predicting Irene's two impacts along the United States east coast. As in previous chapters, comparisons to strength and intensity will be performed. With Irene, the emphasis is shifted

towards precipitation impacts, before, during, and after landfall. Precipitation analysis will be conducted using remotely observed variables of precipitation rate and intensity.

Precipitation flux into the ocean will be examined in order to determine the impact on a salinity budget in the upper-ocean. Salinity cross-sections show the precipitation signature as the storm moves along the coast, which rapidly disappears under heavy wind. As in previous cases, comparison to ocean and wave environments is completed using multiple *in situ* data sources of 10 m wind, SLP, SST, and significant wave height.

The final chapter serves to review the discussions of the previous chapters and seeks to provide a platform for future research. The utility of coupled numerical modeling is reiterated and the success of the study highlighted that showed coupling to the ocean was significant in regions of high heat content and deep mixed layer depth but coupling to a wave model was more important for faster moving TCs. Prediction of rainfall was improved when coupling to an ocean model versus without coupling. Significant improvement of the initial condition in hindcast and forecast will be sought in future research. In addition, several questions remain in improving and examining the coupled numerical solution of a tropical cyclone. Some of these questions require datasets that examine air-sea interactions in environments of intense TCs where minimal data currently exists. In addition, existing parameterizations have not been thoroughly tested in extreme wind regimes.

Air-Sea Interaction During Landfalling Tropical and Extra-Tropical Cyclones

by  
Joseph Brendan Zambon

A dissertation submitted to the Graduate Faculty of  
North Carolina State University  
in partial fulfillment of the  
requirements for the Degree of  
Doctor of Philosophy

Marine, Earth and Atmospheric Sciences

Raleigh, North Carolina

2014

APPROVED BY:

---

Dr. Ruoying He  
(Chair of Advisory Committee)

---

Dr. John C. Warner

---

Dr. Gary M. Lackmann

---

Dr. Lian Xie

## **BIOGRAPHY**

Joseph (Joe) was born in Buffalo, NY on 26 August 1985 and attended high school at Canisius High School where he graduated in 2003. He developed an interest in meteorology at the age of six when a tornadic thunderstorm passed overhead in the summer of 1992. His mother, an avid librarian, nurtured his interest by providing a number of books on the subject. The destruction caused by Hurricane Andrew one day before his seventh birthday cemented his interest in the field.

Over the years his fascination in meteorology spread to a number of areas as his mother continued supplying him with books on a number of subjects related to earth science: from earthquakes to the atmosphere. Joe always came back to meteorology, especially during hurricane season when he would plot the locations of storms on his laminated hurricane-tracking chart, which still sits above his desk. Living in Buffalo, winter was always an active season. Joe began his young career providing Lake Effect Snow forecasts for his fellow schoolmates, advising them whether or not they should expect to be off from school the following day.

Joe continued his studies of the atmosphere at The State University of New York at Albany (SUNY) where he chose a major in Atmospheric Science and a minor in Mathematics and Statistics. Joe also nurtured his interest in computer science with a number of courses in the field, and worked for Information Technology Services with the University while attending classes. Joe concluded his studies at Albany with a B.S. in Atmospheric Science, many interesting classes, and a little research under his belt.

Joe began his studies in the Department of Marine, Earth, and Atmospheric Sciences at The North Carolina State University in August 2007. He was fortunate enough to have his thesis advisor, Dr. Ruoying He, provide him with a topic that was as broad as his interests would allow. After initially beginning with a review of the related literature, Joe dived into the coupled model as Dr. John Warner and Dr. Ruoying He were developing it. Initially his Master's research included development of an idealized tropical cyclone, and was then expanded to include hurricanes Isabel and Ivan.

After successfully defending his Master's work in July 2009, and graduating that December, Joe continued his work as a Ph.D. student. After completing classes and successfully passing written and oral preliminary exams in November 2012, Joe was admitted to Ph.D. candidacy. Continuing from his Master's work, he completed research on Hurricanes Ivan, Sandy, and Irene using coupled models and analysis. He completed and submitted his dissertation to his committee in October 2014 for a scheduled defense the following month.

During his Ph.D. research, Joe was grateful to develop and assist in the development of several journal articles, as well as attend and present at a number of conferences and workshops. At present, his CV includes 5 refereed publications with another 2 in review. Joe has written or co-written 22 abstracts for scientific conferences and meetings. In 2010, Joe received a graduate research fellowship through the NASA North Carolina Space Grant. Since 2011, Joe has been tasked with maintaining daily coupled and uncoupled nowcast/forecast models of the Ocean Modeling and Observing Group at North Carolina State University.

Getting outside of the lab, Joe has been involved in 8 different research cruises since 2008. He has studied the oceans along the United States east coast, Gulf of Mexico, Caribbean and Sargasso Seas, Barbados and (accidentally) Venezuela. Joe has also co-taught 3 graduate-level classes in ocean and atmospheric modeling.

Joe is also extensively involved in service and leadership. He has been a volunteer firefighter and EMT for 10 years, beginning while living in Albany, NY and later joined a volunteer fire department in Raleigh. Joe was President of the Marine, Earth and Atmospheric Sciences Graduate Student Association for two academic years and chaired their symposium on Numerical Modeling in 2011. Since 2008, he played for of an adult recreation ice hockey team in Raleigh, he is also currently their captain. Other interests include aviation (Joe is a licensed pilot), SCUBA diving, and is a die-hard Buffalo Bills, Buffalo Sabres, and NC State fan.

## **ACKNOWLEDGEMENTS**

I would like to thank my advisory committee: Dr. Ruoying He, Dr. John Warner, Dr. Gary Lackmann, and Dr. Lian Xie, for the opportunity to perform research in this exciting and rapidly expanding field of coupled modeling. I would especially like to thank Dr. Ruoying He for his helpfulness and patience with this extensive research project and for including me on several field campaigns. It has been a very interesting and challenging road since the summer of 2007, looking back on it I cannot even begin to quantify the amount I have learned in my experience here at North Carolina State University.

I also wish to thank my friends here in Raleigh as well as the lifelong friends I have made in my life through this point, without whom I probably would have graduated years ago. I would especially like to point out the support and assistance I have received from Jeff Willison and Kevin Hill.

I like to thank the people I have worked with in the volunteer fire departments. I would like to thank my hockey team, for 6 years of enjoyable hockey and a hard-fought championship. I would also like to thank the servers, patrons, and bartenders at BaDa Wings in Raleigh, just down the hill from Jordan Hall, for giving me a place to go after work.

Lastly, I would like to thank my fiancé and my family. My fiancé, Sarah, has been my rock through the hours spent researching. My father taught me to work hard and to always strive to complete tasks with no compromise in effort. My sisters on whose stellar example I constantly evaluate my own goals. And finally, my late mother who nurtured my interest in science from the very beginning. It was a poignant coincidence that the work detailed in second chapter of this dissertation was published this week, on her 65<sup>th</sup> birthday.

## TABLE OF CONTENTS

LIST OF TABLES \_\_\_\_\_ viii

LIST OF FIGURES \_\_\_\_\_ ix

1	Introduction	1
1.1	Motivation	1
1.2	Literature review	3
1.2.1	Methodology overview	3
1.2.2	Ocean response through idealized modeling approach	4
1.2.3	Ocean response to TC simulated through a 1-D Ocean Mixed Layer Model	10
1.2.4	Observation of ocean response to TC impacts	12
1.2.5	Ocean circulation impacts on reducing TC intensity	16
1.2.6	TC precipitation effect on ocean salinity	18
1.2.7	TC interaction with wave environment	21
1.2.8	Additional sources of TC intensity prediction errors	26
1.2.9	Review of other coupled modeling studies	27
2.	Hindcast experiments of Hurricane Ivan (2004) utilizing the Coupled Ocean- Atmosphere-Wave-Sediment Transport (COAWST) model	40
2.1	Introduction	40
2.2	Methodology	44
2.2.1	Modeling System	44
2.2.2	Model Coupling	46
2.2.3	Experimental Design	49
2.2.4	Domain and Model Configuration	50
2.3	Results and Analysis	55
2.3.1	Atmosphere	55
2.3.2	SST Analysis	56
2.3.3	Mixed Layer Prognostic Variable Analysis	60
2.3.4	Mixed Layer Heat Budget Analysis	61
2.3.5	Wave Analysis	64
2.4	Summary and Conclusions	66
3.	Investigation of the Effect of Coupling on the Extratropical Transition of Superstorm Sandy (2012)	70
3.1	Introduction	70
3.2	Methodology	75
3.2.1	Model Configuration	75
3.2.2	Experiment Design	79
3.3	Results and Discussion	80
3.3.1	Atmosphere	80
3.3.2	Ocean	87
3.3.3	Wave	88

3.4	Summary and Conclusions	89
4.	Examination of Hurricane Irene (2011) Using Coupled Model Forecast	91
4.1	Introduction	91
4.2	Methodology	94
4.2.1	Model Configuration	94
4.2.2	Experimental Design	98
4.3	Results and Discussion	99
4.3.1	Atmosphere	99
4.3.2	Ocean	104
4.3.3	Wave	110
4.4	Summary and Conclusions	111
5.	Conclusions and Future Work	117
	References	171

## LIST OF TABLES

<b>Table 1.1.</b> Configuration of various coupled models for review and comparison_____	121
<b>Table 2.1.</b> Design of 5 experiments relating to the level of ocean and wave interaction__	121
<b>Table 2.2.</b> Intensity comparisons against verification for 5 experiments over 108 h hindcast. Includes Root Mean Squared Error (RMSE), and correlation coefficient (r) for Intensity (in hPa)_____	122
<b>Table 3.1.</b> Design of 4 experiments relating to the level of ocean and wave interaction__	122
<b>Table 3.2.</b> Intensity (hPa) and Strength ( $\text{ms}^{-1}$ ) comparisons against verification for 4 experiments over first 60 hours of 132 hour hindcast as Sandy dissipated shortly after landfall. Includes Root Mean Squared Error (RMSE), and correlation coefficient (r)_____	122
<b>Table 3.3.</b> Significance testing (Student's T-test) of experiments. P-value and Confidence Interval (CI) demonstrated for differences among the 4 model experiments_____	123
<b>Table 4.1.</b> Design of 5 experiments relating to the level of ocean and wave interaction__	123
<b>Table 4.2.</b> Intensity (hPa) and Strength ( $\text{ms}^{-1}$ ) comparisons against verification for 5 experiments over 84 h hindcast. Includes Root Mean Squared Error (RMSE), and correlation coefficient (r)_____	124

## LIST OF FIGURES

- Figure 1.1.** Schematic of wind stress vector rotation with TC translation (for northern hemisphere) \_\_\_\_\_ 125
- Figure 2.1.** Diagram of 3-Way coupled model as implemented in the COAWST model for Hurricane Ivan experiments \_\_\_\_\_ 126
- Figure 2.2.** Comparison of forecast track, 5 experiments: *Static SST* (red), *Dynamic SST* (green), *WRF OML* (cyan), *2-Way* (blue), *3-Way* (magenta). NHC best track verification (black). Also shown are the location of onshore and offshore grid points (S1, S2) used for analysis in Figs. 2.7-2.10 \_\_\_\_\_ 127
- Figure 2.3.** Simulated TC position (km) and intensity (hPa) errors from initialization (12 UTC 12 September 2004) through termination (00 UTC 17 September 2004), 5 experiments: *Static SST* (red), *Dynamic SST* (green), *WRF OML* (cyan), *2-Way* (blue), *3-Way* (magenta) \_\_\_\_\_ 128
- Figure 2.4.** Simulated TC intensity from initialization (12 UTC 12 September 2004) through termination (00 UTC 17 September 2004), 5 experiments: *Static SST* (red), *Dynamic SST* (green), *WRF OML* (cyan), *2-Way* (blue), *3-Way* (magenta). NHC best track verification (black) \_\_\_\_\_ 129
- Figure 2.5.** Coupled SST comparisons for various experimental cases: *Dynamic SST* based on the Gemmill et al. (2007) SST analysis (first row). *WRF OML* based on Pollard et al. (1973) and integrated into WRF by Davis et al. (2008; second row). *2-Way*, Atmosphere-Ocean model coupling (third row). *3-Way*, Atmosphere-Ocean-Wave model coupling (fourth row). GOES SST data obtained from the JPL Physical Oceanography Distributed Active Archive Center (PODAAC; fifth row). Pre-Storm Averaged model SST (top 4 rows, left column). Post-Storm Averaged model SST (top 4 rows, middle column). Pre-Storm averaged GOES SST (bottom row, left column). Post-Storm averaged GOES SST (*bottom row, middle column*). Change in SST (right column) \_\_\_\_\_ 130
- Figure 2.6.** SST time series at 5 buoys situated inside of the Gulf of Mexico, showing *2-Way* (red line) and *3-Way* (blue line) SST, satellite derived SST (black asterisks) and in-situ SST (black line). Spatial difference in SST between *2-Way* and *3-Way* cases at conclusion of model run, along with location of buoys and *3-Way* simulated TC track (bottom right panel) \_\_\_\_\_ 131

**Figure 2.7.** Ocean model (*2-Way*) analysis at point S1 in Figure 2.2 from initialization (12 UTC 12 September 2004) through termination (00 UTC 17 September 2004). Wind stress ( $\tau$ ) in  $\text{Nm}^{-2}$  (first panel), heat flux (HF) in  $\text{Wm}^{-2}$  (second panel), temperature from surface through 100 m depth in  $^{\circ}\text{C}$  (third panel), U velocity from surface through 100 m depth in  $\text{ms}^{-1}$  (fourth panel), V velocity from surface through 100 m depth in  $\text{ms}^{-1}$  (fifth panel), W velocity from surface through 100 m depth in  $\text{ms}^{-1}$  (bottom panel)\_\_\_\_\_ 132

**Figure 2.8.** Ocean model (*2-Way*) analysis at point S2 in Figure 2.2 from initialization (12 UTC 12 September 2004) through termination (00 UTC 17 September 2004). Wind stress ( $\tau$ ) in  $\text{Nm}^{-2}$  (first panel), heat flux (HF) in  $\text{Wm}^{-2}$  (second panel), temperature from surface through 100 m depth in  $^{\circ}\text{C}$  (third panel), U velocity from surface through 100 m depth in  $\text{ms}^{-1}$  (fourth panel), V velocity from surface through 100 m depth in  $\text{ms}^{-1}$  (fifth panel), W velocity from surface through 100 m depth in  $\text{ms}^{-1}$  (bottom panel)\_\_\_\_\_ 133

**Figure 2.9.** Ocean model (*2-Way*) analysis of heat budget at point S1 in Figure 2.2 from initialization (12 UTC 12 September 2004) through termination (00 UTC 17 September 2004). Horizontal advection term in  $^{\circ}\text{C}/\text{day}$  (upper-left), vertical advection term in  $^{\circ}\text{C}/\text{day}$  (upper-right), total advection term in  $^{\circ}\text{C}/\text{day}$  (middle-left), vertical diffusion term in  $^{\circ}\text{C}/\text{day}$  (middle-right), total local rate of change term in  $^{\circ}\text{C}/\text{day}$  (lower-left), temperature in  $^{\circ}\text{C}$  (lower-right), comparison of contributions of advection and diffusion to local change in temperature integrated through 100 m (bottom panel)\_\_\_\_\_ 134

**Figure 2.10.** Ocean model (*2-Way*) analysis of heat budget at point S2 in Figure 2.2 from initialization (12 UTC 12 September 2004) through termination (00 UTC 17 September 2004). Horizontal advection term in  $^{\circ}\text{C}/\text{day}$  (upper-left), vertical advection term in  $^{\circ}\text{C}/\text{day}$  (upper-right), total advection term in  $^{\circ}\text{C}/\text{day}$  (middle-left), vertical diffusion term in  $^{\circ}\text{C}/\text{day}$  (middle-right), total local rate of change term in  $^{\circ}\text{C}/\text{day}$  (lower-left), temperature in  $^{\circ}\text{C}$  (lower-right), comparison of contributions of advection and diffusion to local change in temperature integrated through 100 m (bottom panel)\_\_\_\_\_ 135

- Figure 2.11.** *3-Way* model wave comparison from initialization (12 UTC 12 September 2004) through termination (00 UTC 17 September 2004). Observed (black) and modeled (red) significant wave heights at 5 buoy locations: 42001 (upper left), 42003 (upper middle), 42007 (upper right), 42039 (lower left), 42040 (lower middle). Inset (lower right) shows locations of buoys, simulated tracks, and wave heights at F090 (shaded). Some observations were not available due to extreme waves (e.g. buoy 42040 was torn from its mooring). For each comparison, the correlation coefficient and rms error between observed and simulated significant wave heights are given, along with the water depth information of each station \_\_\_\_\_ 136
- Figure 2.12.** 4-panel plot of the *3-Way* experiment demonstrating the atmosphere, ocean, and wave environments at the time of simulated landfall in Alabama (07 UTC 16 September 2004). The atmospheric environment is represented as quantities of SLP (upper left, shaded) and wind (upper right, shaded with vector arrows). The ocean environment is represented by SST (lower left, shaded) and surface current (lower left, vector arrows). The wave environment is represented by significant wave height (lower right, shaded) \_\_\_\_\_ 137
- Figure 3.1.** Diagram of 3-Way coupled model as implemented in the COAWST model for Superstorm Sandy experiments \_\_\_\_\_ 138
- Figure 3.2.** 4-panel plot of the *3-Way* experiment demonstrating the atmosphere, ocean, and wave environments at the time of simulated landfall in New Jersey (22 UTC 29 October 2012). The atmospheric environment is represented as quantities of SLP (upper left, shaded) and wind (upper right, shaded with vector arrows). The ocean environment is represented by SST (lower left, shaded) and surface current (lower left, vector arrows). The wave environment is represented by significant wave height (lower right, shaded) \_\_\_\_\_ 139
- Figure 3.3.** Simulated track comparison of 4 experiments: *WRF-Static* (magenta), *WRF-OML* (green), *2-Way* (blue), *3-Way* (red). The NHC Best Track product is used for verification (black). SST at initialization from the *3-Way* case is shaded. Buoys for *in situ* comparison in Figures 3.8 and 3.9 are included \_\_\_ 140
- Figure 3.4.** Simulated comparison of intensity (hPa) and strength ( $\text{ms}^{-1}$ ) of 4 experiments: *WRF-Static* (magenta), *WRF-OML* (green), *2-Way* (blue), *3-Way* (red). The NHC Best Track product is used for verification (black). First 60 hours of 132 hour hindcast are shown as Sandy dissipated shortly after landfall \_\_\_\_\_ 141

- Figure 3.5.** Simulated comparison of intensity (hPa) and strength ( $\text{ms}^{-1}$ ) residuals against verification of 4 experiments: *WRF-Static* (magenta), *WRF-OML* (green), *2-Way* (blue), *3-Way* (red). First 60 hours of 132 hour hindcast are shown as Sandy dissipated shortly after landfall. Positive (negative) indicates under-(over-) intensification/strengthening\_\_\_\_\_142
- Figure 3.6.** Analysis of bottom stress calculations (right column) based on wind speed ( $\text{ms}^{-1}$ , left column), wave height (m, middle column), and bottom stress ( $\text{ms}^{-1}$ , right column) at simulation hour 12 (00 UTC 29 October). *2-Way* experiment (top row), *3-Way* experiment (middle row), difference fields (bottom row)\_\_\_143
- Figure 3.7.** Environmental conditions prior to Sandy’s landfall (12 UTC 28 October through approximately 00 UTC 30 October). Figure includes: (a) simulated intensity (minimum SLP, hPa) every 3 h, (b) simulated strength (maximum 10 m wind,  $\text{ms}^{-1}$ ) every 3 h, (c) hourly SST ( $^{\circ}\text{C}$ ), (d) hourly ocean heat content (OHC,  $10^5 \text{kJcm}^{-2}$ ), (e) hourly vertical shear ( $\text{ms}^{-1}$ ) calculated between 850/200 hPa (red) and 850/500 hPa (blue), and (f) translation speed ( $\text{ms}^{-1}$ ) evaluated every 6 h. The *3-Way* case was analyzed with NHC best track Verification (black) every 6 h where available (a, b, f)\_\_\_\_\_144
- Figure 3.8.** Simulated SST comparisons to *in situ* buoy data collected at 5 locations along the U.S. east coast demonstrated in Figure 3.3. Verification along with 3 experiments are shown throughout the entire model simulation (132 hr). SST in the *WRF-Static* case is not shown as it is demonstrated by the initial *WRF-OML* SST across the entire time series. Remaining experiments are shown, 4 experiments: *WRF-OML* (green), *2-Way* (blue), *3-Way* (red)\_\_\_\_\_145
- Figure 3.9.** Simulated significant wave height comparisons to *in situ* buoy data collected at 5 locations along the U.S. east coast demonstrated in Figure 3.3. Verification along with the wave-coupled (*3-Way*) experiment is shown throughout the entire model simulation (132 hr). Also shown are correlation coefficients ( $r$ ) and root-mean-square error (RMSE)\_\_\_\_\_146
- Figure 4.1.** Hurricane Irene’s track through the Atlantic Ocean (black). Thinner colored lines demonstrate the forecast tracks of ensemble members ( $n=73$ ) at the time of forecast initialization (12 UTC 25 August 2011). Thicker lines through the middle of the swath denote model experiment simulations. The red dot denotes the NHC Best Track location of Hurricane Irene at forecast simulation initialization\_\_\_\_\_147

- Figure 4.2.** Hurricane Irene’s strength (black) from model initialization (12 UTC 25 August 2011) through model termination (00 UTC 29 August 2011). Thinner colored lines demonstrate the forecast tracks of ensemble members (n=73) at the time of forecast initialization (12 UTC 25 August 2011) through completion of a 120 hr forecast (12 UTC 30 August 2011). Thicker lines through the middle of the swath denote our forecast simulations and include 5 experiments: *WRF-Static* (cyan), *WRF-Filter* (pink), *WRF-Dynamic* (green), *2-Way* (blue), *3-Way* (red)\_\_\_\_\_ 148
- Figure 4.3.** Spatial SST comparison between the original 1/12° RTG-SST (Gemmill et al. 2007; left column) product and the 1-2-1 filtered SST product (middle column). The difference (Original – Filtered) between the two fields is also shown (right column)\_\_\_\_\_ 149
- Figure 4.4.** Simulated track comparison of 5 experiments: *WRF-Static* (cyan), *WRF-Filter* (pink), *WRF-Dynamic* (green), *2-Way* (blue), *3-Way* (red). The NHC Best Track product is used for verification (black). SST at initialization from the *3-Way* case is shaded\_\_\_\_\_ 150
- Figure 4.5.** 4-panel plot of the *3-Way* experiment demonstrating the atmosphere, ocean, and wave environments at the time of simulated landfall in North Carolina (17 UTC 27 August 2011). The atmospheric environment is represented as quantities of SLP (upper left, shaded) and wind (upper right, shaded with vector arrows). The ocean environment is represented by SST (lower left, shaded) and surface current (lower left, vector arrows). The wave environment is represented by significant wave height (lower right, shaded)\_\_\_\_\_ 151
- Figure 4.6.** Simulated comparison of intensity (hPa) and strength ( $\text{ms}^{-1}$ ) of 5 experiments: *WRF-Static* (cyan), *WRF-Filter* (pink), *WRF-Dynamic* (green), *2-Way* (blue), *3-Way* (red). The NHC Best Track product is used for verification (black)\_\_\_ 152
- Figure 4.7.** Track positions demonstrated as in Fig. 4.4 but with the addition of the 6 *in situ* buoys utilized for analysis in Figs. 4.8, 4.9, 4.12, and 4.24\_\_\_\_\_ 153
- Figure 4.8.** Simulated 10 m wind speed comparisons to *in situ* buoy data collected at 6 locations along the U.S. east coast demonstrated in Figure 4.7. Verification along with 5 experiments are shown throughout the entire model simulation (84 hr)\_\_\_\_\_ 154

- Figure 4.9.** Simulated SLP comparisons to *in situ* buoy data collected at 6 locations along the U.S. east coast demonstrated in Figure 4.7. Verification along with 5 experiments are shown throughout the entire model simulation (84 hr)\_\_\_\_\_155
- Figure 4.10.** Forecast simulated precipitation rate ( $\text{mm hr}^{-1}$ ) of 5 experiments compared to satellite-derived Global Satellite Mapping of Precipitation (GSMaP) product (upper-left). Included are experiments *3-Way* (upper-middle), *2-Way* (upper-right), *WRF-Dynamic* (lower-left), *WRF-Filter* (lower-middle), and *WRF-Static* (lower-right)\_\_\_\_\_156
- Figure 4.11.** Forecast simulated precipitation flux ( $\text{mm hr}^{-1}$ ) integrated over all simulated grid points. Comparison of 5 experiments to satellite-derived Global Satellite Mapping of Precipitation (GSMaP) product (black). 5 experiments: *WRF-Static* (cyan), *WRF-Filter* (pink), *WRF-Dynamic* (green), *2-Way* (blue), *3-Way* (red)\_\_\_\_\_157
- Figure 4.12.** Simulated SST comparisons to *in situ* buoy data collected at 6 locations along the U.S. east coast demonstrated in Figure 4.7. Verification along with 4 experiments are shown throughout the entire model simulation (84 hr). SST in the *WRF-Static* case is not shown as it is demonstrated by the initial *WRF-Dynamic* SST across the entire time series. Remaining experiments are shown, 4 experiments: *WRF-Filter* (pink), *WRF-Dynamic* (green), *2-Way* (blue), *3-Way* (red)\_\_\_\_\_158
- Figure 4.13.** Track positions demonstrated as in Fig. 4.4 but with the addition of the 3 point locations utilized for time series analysis of the salinity budget in Figures 4.14, 4.15 and 4.16 \_\_\_\_\_159
- Figure 4.14.** Ocean model (*2-Way*) analysis of salinity budget at point S1 in Fig. 4.13 from initialization (12 UTC 25 August 2011) through termination (00 UTC 29 August 2011). Horizontal advection term in PSU/day (upper-left), vertical advection term in PSU/day (upper-right), total advection term in PSU/day (middle-left), vertical diffusion term in PSU/day (middle-right), total local rate of change term in PSU/day (lower-left), salinity in PSU (lower-right)\_\_\_\_\_160
- Figure 4.15.** Ocean model (*2-Way*) analysis of salinity budget at point S2 in Fig. 4.13 from initialization (12 UTC 25 August 2011) through termination (00 UTC 29 August 2011). Horizontal advection term in PSU/day (upper-left), vertical advection term in PSU/day (upper-right), total advection term in PSU/day (middle-left), vertical diffusion term in PSU/day (middle-right), total local rate of change term in PSU/day (lower-left), salinity in PSU (lower-right)\_\_\_\_\_161

- Figure 4.16.** Ocean model (2-*Way*) analysis of salinity budget at point S3 in Fig. 4.13 from initialization (12 UTC 25 August 2011) through termination (00 UTC 29 August 2011). Horizontal advection term in PSU/day (upper-left), vertical advection term in PSU/day (upper-right), total advection term in PSU/day (middle-left), vertical diffusion term in PSU/day (middle-right), total local rate of change term in PSU/day (lower-left), salinity in PSU (lower-right)\_\_\_\_\_ 162
- Figure 4.17.** Track positions demonstrated as in Fig. 4.4 but with the addition of the 3 lines utilized for cross-section analysis of the upper-ocean salinity in Figures 4.18, 4.19 and 4.20\_\_\_\_\_ 163
- Figure 4.18.** Cross-section of salinity at line S1 from Fig. 4.17 for the upper 50 m of ocean. Four times are chosen to represent the initial (12 UTC 25 August 2011; upper left), storm (10 UTC 26 August 2011; upper right), relaxation (00 UTC 27 August 2011; lower left), and termination (00 UTC 29 August 2011; lower right) periods. The black line denotes the approximate intersecting track of Hurricane Irene. Bottom line plot shows the Precipitation and Evaporation difference as a mass flux ( $\text{kg m}^2 \text{s}^{-1}$ ) with red circles to denote the instantaneous mass flux at the four chosen periods\_\_\_\_\_ 164
- Figure 4.19.** Cross-section of salinity at line S2 from Figure 4.17 for the upper 50 m of ocean. Four times are chosen to represent the initial (12 UTC 25 August 2011; upper left), storm (21 UTC 26 August 2011; upper right), relaxation (14 UTC 27 August 2011; lower left), and termination (00 UTC 29 August 2011; lower right) periods. The black line denotes the approximate intersecting track of Hurricane Irene. The black line denotes the approximate intersecting track of Hurricane Irene. Bottom line plot shows the Precipitation and Evaporation difference as a mass flux ( $\text{kg m}^2 \text{s}^{-1}$ ) with red circles to denote the instantaneous mass flux at the four chosen periods\_\_\_\_\_ 165
- Figure 4.20.** Cross-section of salinity at line S3 from Figure 4.17 for the upper 50 m of ocean. Four times are chosen to represent the initial (12 UTC 25 August 2011; upper left), storm (10 UTC 27 August 2011; upper right), relaxation (00 UTC 28 August 2011; lower left), and termination (00 UTC 29 August 2011; lower right) periods. Bottom line plot shows the Precipitation and Evaporation difference as a mass flux ( $\text{kg m}^2 \text{s}^{-1}$ ) with red circles to denote the instantaneous mass flux at the four chosen periods\_\_\_\_\_ 166

- Figure 4.21.** Spatial analysis of the surface salinity budget as Hurricane Irene makes landfall (12 UTC 27 August 2011) in North Carolina, *2-Way EMINUSP* (realistic precipitation flux) experiment.. Terms of the salinity budget are horizontal advection (upper-left), vertical advection (upper-right), total advection (middle-left), vertical diffusion (middle-right), total salinity rate of change (lower left), and a snapshot of the surface salinity\_\_\_\_\_167
- Figure 4.22.** Spatial analysis of the surface salinity budget as Hurricane Irene makes landfall (12 UTC 27 August 2011) in North Carolina, *2-Way ANA\_SSFLUX* (analytical surface salt flux) experiment. Terms of the salinity budget are horizontal advection (upper-left), vertical advection (upper-right), total advection (middle-left), vertical diffusion (middle-right), total salinity rate of change (lower left), and a snapshot of the surface salinity\_\_\_\_\_168
- Figure 4.23.** Precipitation at the location of the storm center 10 hours (lag) after the forecast time. Lagged storm location is necessary as the precipitation at the storm center would not be indicative of the strongest precipitation. The best time interval of lag was determined based on the anti-correlation of these two time series (e.g. high precipitation induces low surface salinity). The difference in surface salinity is from *EMINUSP* subtracted from *ANA\_SSFLUX* (negative values denote lower salinity in *EMINUSP*). Missing data points are when the lagged storm center is located over land\_\_\_\_\_169
- Figure 4.24.** Simulated significant wave height comparisons to *in situ* buoy data collected at 6 locations along the U.S. east coast demonstrated in Figure 4.7. Verification along with the *3-Way* experiments is shown throughout the entire model simulation (84 hr). Comparison also shows the correlation coefficient ( $r$ ), Root-Mean-Square Error (RMSE; in m) and modeled depth (m) at each location\_\_170

# **1 Introduction**

## *1.1 Motivation*

Worldwide, Tropical Cyclones (TCs) represent extreme, discrete events that result in drastic consequences to the coastal environment. Within the United States (U.S.), where a large fraction of the population lives within the coastal environment, TCs are one of the costliest natural catastrophes and account for a large percentage of damage, injury and loss of life (Emanuel 2005). As considerably more people and property have aggregated to the shoreline in recent decades, the damage caused by these intense storms will continue to increase (Emanuel et al. 2004; Oey et al. 2007). The 2005 Atlantic hurricane season was the costliest on record, with 28 named storms causing nearly 1,700 direct fatalities and damages over \$100 billion in the U.S. alone (Beven et al. 2008). Unfortunately, extratropical (ETCs) and post-tropical storms have similar impact as TCs. In October 2012 Superstorm Sandy made an impact on the northeastern U.S. as a post-tropical storm, with considerable damage estimated at around \$50 Billion and 147 deaths from this single storm (Blake et al. 2013).

The impacts of climate change on TCs and ETCs is a topic still under considerable debate (e.g. Emanuel 2005; Lackmann 2014). However, there is no doubt that with the population, property, and infrastructure continuing to build along the coastal U.S., the importance of mitigating TC damage to coastal communities will only continue to increase. An important contribution to that mitigation is accurate prediction of TCs, as well as the environment in which they develop. With the utilization of faster computational resources, numerical coupled dynamical models have been recently utilized to forecast and hindcast the coastal environment. Several recent studies have been undertaken that utilize coupled

models in order to accurately simulate not only the TC within the atmosphere, but also the ocean and wave environments, which have drastic impacts as the source of energy for these storms.

An important task in simulating TCs is to aid in the prediction of these storms before, during and after landfall. Within the U.S., the National Hurricane Center (NHC) has done an excellent job of continually improving forecasts. Track forecasts of hurricanes have shown gradual improvements over the years, primarily through improvements to coarse-grid, global models (Marks and Shay 1998; Wang and Wu 2004; Goerss 2006; Bender et al. 2007; Rogers et al. 2006). Rogers et al. (2006) attributes TC forecast track improvements to several areas including improved assimilation of satellite and aircraft observations, better representation of the hurricane vortex, and improved representation of tropical physics. According to Rogers et al. (2006), the forecast of storm track from 1991-2006 improved 45% (or 3% yr<sup>-1</sup>). At the same time, intensity forecasting during that same period improved at a much smaller rate, 17% (or 1.1% yr<sup>-1</sup>) (Rogers et al. 2006; Wada et al. 2010). There are several possible causes for the limited increase of skill in developing accurate intensity forecasts needed for dissemination to emergency managers and the public.

Chen et al. (2007) attributes this problem to four distinct areas. First, there are always deficiencies in hydrodynamical models. These deficiencies are continually being improved upon through process studies in other areas. Second, there is a problem of insufficient grid resolution. This problem is addressed through increased efficiency of computational resources, which roughly follows Moore's law – a doubling in computing power approximately every two years. Third, inadequate understanding and representation of

physics in surface and boundary layer formulations are partly to blame. This problem is being addressed through other approaches utilizing observations and modeling. Fourth, a lack of coupling to a dynamic ocean, which is the topic of this dissertation. Another distinct area seeking improvement is in TC initialization (Davis et al. 2008; Gentry and Lackmann 2009), which we will briefly examine through experiments in Chapter 2.

Morey et al. (2006) describes air-sea interaction associated with a TC is critical to understanding the development and life cycle of these storms. The result of which would be to improve intensity and track forecasting. Shen and Ginis (2003) note that it is well-established that hurricane intensity over the open ocean may be significantly reduced due to sea surface cooling due to air-sea interaction.

The goal of this dissertation is to examine air-sea interaction through use of a newly developed Coupled Ocean-Atmosphere-Wave-Sediment Transport (COAWST; Warner et al. 2010) model. In doing so, we demonstrate that coupled modeling systems will provide improvement to the prediction of hurricane intensity, environmental states of surface waves and sea surface temperature, and atmospheric impact from precipitation distribution.

## *1.2 Literature Review*

### *1.2.1 Methodology overview*

Air-sea interaction features a sampling of publications, articles and books, which describe the intricate processes that occur between the atmosphere and ocean. This literature review is an attempt to summarize some of those materials in order to better understand the processes occurring through examination of the case studies in later chapters. A number of

these reviews are carried over from my earlier M.S. thesis work in Zambon (2009), and are included here for the sake of completion. Review of atmosphere-ocean-wave coupled models would easiest be served by discretizing these environments into their component parts (e.g. atmosphere, ocean, wave). However, this is difficult as feedback mechanisms occur continually between these parts, spilling over from section to section. As a result, this chapter will serve to review studies individually, without splitting component parts. Future chapters of individual case studies will better separate the environments (atmosphere, ocean, wave) while exploring the feedback mechanisms between.

### *1.2.2 Ocean response through idealized modeling approach*

Price (1981) was one of the first to provide very detailed presentation of the dynamics of upper ocean circulation through idealized numerical modeling. His efforts provided a review of basic components contributing to upwelling and downwelling features in the deep ocean and are an excellent place to start an understanding of the ocean dynamics beneath TCs. At the time, an empirical examination of historical observations involving hurricanes passing over a buoy or otherwise data-rich section of the ocean suggests an obvious result – intense, slow moving hurricanes cause the greatest variation in Sea Surface Temperatures (SSTs).

The greatest change in SSTs ( $\Delta$ SST) occurs on the right side of hurricanes. This relationship was mentioned and studied initially in Price (1981) and was investigated in detail through real cases and through use of an ocean model described below. In several cited cases, the difference between the  $\Delta$ SST on the right and left side varied by several

degrees Celsius. Originally discussed in Ooyama (1969), Leipper and Volgenau (1972), and later detailed extensively by Emanuel (1986), numerous numerical simulations of TCs demonstrate that the essential importance of latent and, by a few factors less, sensible heat flux is from the sea surface. These papers, among others, demonstrate the importance that SST has on the intensity and track of TCs. This cross-track  $\Delta$ SST change is an important mechanism as both the TC intensity, and to a lesser extent TC track, is dependent on the location of the warm water beneath the storm.

To look into this phenomenon in greater detail, Price (1981) constructed a simple ocean model around the following physical approximations: Coriolis is held constant, pressure is hydrostatic, Boussinesq's approximation is made throughout, and diffusive processes (not including entrainment) are excluded. Density is computed from a linear equation of state. The sea surface is treated as a rigid lid. The subthermocline ocean is taken as infinitely deep and unable to sustain a pressure gradient. Temperature and salinity are assumed to have linear depth dependence and vertical density gradients are held constant.

This simple ocean model was initialized with in-situ observations of the ocean prior to the passage of Hurricane Eloise (1981). The initial environment that was constructed was based off of several buoy and ship reports in the path of Eloise in the two weeks preceding the event. To simplify things further, the hurricane's winds were taken to be symmetric, and the hurricane was stationary. The purpose to leaving the ocean stationary was to challenge a pre-existing notion that the higher  $\Delta$ SST values on the right hand side of the hurricane were due to the higher winds on that side of the storm. This well known phenomenon is due to the summation of winds and forward motion of the storm in the right-front quadrant of TCs.

Important conclusions from the Price (1981) paper include that the reason the  $\Delta$ SST values are higher on the right side have to do with the wind stress turning clockwise on the right side of the storm, thereby creating positive feedback to the inertial currents in the Northern Hemisphere (as demonstrated in Fig. 1.1). With inclusion of an experiment where the storm was stationary, Price (1981) was able to make this conclusion over the previously accepted theory that the sea surface experienced greater cooling on the right hand side of the track due to the stronger relative winds. The simple ocean model also confirmed the trivial result that  $\Delta$ SST response was largest for strong, slow moving hurricanes.

Within the same article, Price (1981) considered the contributions to  $\Delta$ SST by comparing the values of heat flux due to interaction with the atmosphere and heat flux due to entrainment. The model resolved a  $0.2 \times 10^2 \text{ }^\circ\text{C m}^{-2}$  heat flux between the air and sea. The net heat entrainment value within the ocean dwarfed this result at  $1.3 \times 10^2 \text{ }^\circ\text{C m}^{-2}$ . Therefore, heat entrainment into the mixed layer accounted for approximately 85% of the heat exchange in the idealized model from Price (1981). This process will be further investigated in a realistic case in Chapter 2.

Following this, additional experiments were undertaken to understand the effect the depth of the mixed layer and the effect of the temperature gradient in the thermocline would have on the SST during and after the passage of a TC. Price (1981) took this model and applied it to a few geographic areas of interest. First  $16^\circ\text{N } 20^\circ\text{W}$ , near the eastern boundary current where there is a sharp thermocline, shallow (30 m) mixed layer, and strong temperature gradient. The  $\Delta$ SST response here was estimated to be approximately  $-2.9^\circ\text{C}$ . Another numerical experiment was performed, with a temperature profile similar to  $16^\circ\text{N } 55$

°W, where the western boundary current has a deep thermocline and mixed layer, with a low temperature gradient. Here, the  $\Delta$ SST was estimated to be much smaller, about  $-0.3$  °C.

These processes will also be further investigated in a realistic case in Chapter 2.

This study concludes by stating that the important characteristics of the numerical simulations on the atmospheric solution are based on the strength, translation velocity (speed) and overall size of the TCs. For oceans, the important characteristics are based on initial mixed layer depth, the temperature gradient, and the local inertial period. Somewhat surprisingly, experiments into the Price (1981) model determined that the maximum mixed layer current is insensitive to just about everything except hurricane strength winds and even then only fluctuates about  $1.1 \pm 0.2$   $\text{ms}^{-1}$ . Another equally surprising conclusion from this study is that the  $\Delta$ SST response is insensitive to hurricane size and the local inertial period. As a result of this, larger hurricanes may lower the SST over a larger area, but it was found that the magnitude of the  $\Delta$ SST is minimally different.

Adding further complexity, Price et al. (1994) continued upon the findings in the Price (1981) paper by executing the model for a moving hurricane over an ocean domain. These simulations examined the forcing and stress caused by a hurricane translating above the upper layers of the ocean. It specifically examines the forced stage response during actual storm passage.

According to Price et al. (1994), the forced stage is defined as the local (depth and time dependent) response of the ocean to the very strong wind stress of the hurricane. Included in this response are mixed layer currents, substantial cooling of the mixed layer and SSTs, as well as a barotropic response which includes a geostrophic current and an

associated trough in Sea Surface Height (SSH). Conversely, he describes the relaxation stage as an inherently nonlocal (three-dimensional and time dependent) baroclinic response to the wind stress curl of the hurricane.

The forced stage response was studied in Price et al. (1994) by examining three hurricane events – Norbert (1984), Josephine (1984), and Gloria (1985). These hurricanes were introduced into a three-dimensional ocean model. The model was the same as Price (1981), however it had to be modified when the varying speed and direction of the hurricane paths (Norbert, Josephine, and Gloria) resulted in systematic phase errors. Experimentation revealed that this would result whenever there was either 30° or greater shift in direction or a change in residence time greater than 2 hours. This problem was dealt with by initializing the hurricane well outside of the domain, then moving it along the correct track and speed until it reaches the central point of the domain. The model was then stopped and computations were integrated and saved to determine the resulting effect. The mixed layer depth in Price (1981) was significantly deeper than observed. The issue was resolved in Price et al. (1994) by adopting a hybrid mixed layer formulation that allows for possible mixing below the mixed layer.

As Emanuel (1986) discussed, the air temperature at the surface of the TC was generally 1-3 °C cooler than the temperature of the sea surface. Considering this, Price et al. (1994) defined air and dew point temperatures at the surface to be 3 °C and 4 °C less than the initial SST, respectively. This resulted in a 600 W m<sup>-2</sup> surface heat flux into the atmosphere.

NOAA P3 aircraft deploying 15 AXBTs (Airborne eXpendable BathyThermographs) collected verification and initialization data roughly 40-km apart in a star-like pattern across

the area of the three hurricanes. These AXBTs were able to collect temperature data, surface wave information, and current velocity to an error of  $0.2 \text{ m s}^{-1}$  RMS. The initial upper-ocean currents in the data analysis were treated as random noise under the assumption that hurricane induced currents would be much larger. For model initialization, the initial currents were set to zero.

As to be expected from Price (1981), there was a significant change in mean ocean layer transport in the horizontal structure during TC passage. Again demonstrated here was a rightward bias in transport values,  $120 \text{ m}^2 \text{ s}^{-1}$  versus  $25 \text{ m}^2 \text{ s}^{-1}$  to the left. This bias in strength of transport was confirmed in the AXBT data from verification as well. As shown in Price (1981) and in Fig. 1.1, the turning wind stress vectors remain mostly aligned with the clockwise turning of the currents in the northern hemisphere, which contributed to the additive effect. The opposite is true of the left side of the track, the turning of wind stress vectors and the inertial currents were in opposite phase. The net result was that the transport vectors never get very large on the left side of the track.

Comparison of the Price et al. (1994) model to the observations from the AXBT data suggests a high skill in simulation of mixed layer currents. There was however significant deviation in regions where the observed current speed was  $<0.7 \text{ m s}^{-1}$  and suggests either imprecise instrumentation on behalf of the AXBTs (based on the RMS error of  $0.2 \text{ m s}^{-1}$ ) or a model failure in those regions.

Upwelling was considered to be the most important mechanism of density change in the hurricane response. The model data in Price et al. (1994) was estimated in these cases by the displacement of  $14 \text{ }^\circ\text{C}$  isotherm. Minimal upwelling and pressure coupling was found in

the forward section of hurricanes. As a result, the currents in the forward half were trapped within the mixed layer and the transition layers. Vertical current and temperature profiles were given both from the AXCP data and from the model run, these diagrams showed skill by the model in both temperature change and current velocity with depth.

The Price et al. (1994) paper demonstrated that near-inertial currents in most cases dominated the upper ocean response, a finding that was supported by Price (1981). Also of importance, the vertical mixing is very intense during the forced stage and could penetrate below the mixed layer. Despite this intense vertical mixing, it was also found that the surface mixed layer depth varies only slightly.

The extent of the relaxation stage after hurricane passage will briefly reference Brink (1989). Data and conclusions from this study suggest that with time, the thermocline-depth currents will become gradually more intricate during the relaxation phase. This was demonstrated with moored buoy data. The study also found that direction change grew to more than half a cycle a week after the hurricane passage. Some of these characteristics of relaxation stage response are demonstrated in Chapter 2 and referred for further investigation in Chapter 3.

### *1.2.3 Ocean response to TC simulated through a 1-D Ocean Mixed Layer Model*

There have been considerable efforts to resolve ocean SST while simultaneously considering the additional computational expense that would be required to run a fully three-dimensional ocean model. One of those studies, Davis et al. (2008) utilizes a one-dimensional ocean mixed layer (OML) model from Pollard et al. (1972). The focus of this

study was to reduce over-intensification errors in numerical models by cooling the sea surface dynamically. Other additional considerations were features, including, improved surface-entropy-flux formulation, with a constant drag coefficient for winds greater than  $30 \text{ m s}^{-1}$ . This formulation, from Donelan (2004) emphasizes that above a certain threshold, wind-induced waves begin to “flatten out”. As waves continually build in heavy wind, the crests eventually begin to blow over causing foam to overtop and limit the amount of drag induced by surface waves. Some laboratory studies, and even a few field observations (which are obviously rare in this wind regime), demonstrate that this effect may actually reduce the drag coefficient (Powell et al. 2003; Moon et al. 2004a; Drennan et al. 2005; Liu et al. 2010). The effect of this actually produced the most realistic results in simulating Hurricane Katrina (2005; Davis et al. 2008).

Davis et al. (2008) investigate the effects of utilizing smaller grid spacing to represent the inner core, reducing the inner grid spacing from 4 km to 1.33 km. This impact was substantial, causing the “spin up” period after initialization of Hurricane Katrina (2005) to be substantially reduced, however impacts on track prediction were minimal.

The impact of concern to this dissertation, that of the coupling to an ocean mixed layer model demonstrates some of the aforementioned oceanic impacts that were discussed above. Primarily, the right-side track bias of SST cooling was able to be reproduced to roughly the same magnitude discussed in (Price 1981; Price et al. 1994). The authors also state that capturing the ocean thermal state is an important consideration for accurate modeling of the ocean condition. Their results describe improvement with realistic mixed layer (ML) depth and deep-layer stratification.

The results of Davis et al. (2008) utilizing the Pollard et al. (1972) are significant to this dissertation as comparisons to this model will be drawn in Chapters 2 and 3 in order to discern the importance of utilizing coupling to a fully three-dimensional ocean model.

#### *1.2.4 Observations of ocean response to TC impacts*

An examination of the numerical modeling component of evaluating TC impact on the coastal and deep ocean environment would be remiss without discussion of observations before, during, and after TC events. Discussion of this response features both remote and in situ observations from various platforms. The impacts of TCs on the ocean for this dissertation are broken down into three areas: currents, temperature, and salinity. There are other impacts as well, for example Walker et al. (2005) demonstrated 3 to 4 day lagged response in generating 2 large chlorophyll-*a* blooms, as observed by satellite.

One of the earliest studies of TC impacts on upper-ocean currents, Church et al. (1989) describes observations taken in the wake of Hurricane Gay (1985) through *in situ* and remotely derived measurements aboard the R/V Thomas G. Thompson. These observations included conductivity-temperature-depth (CTD) and acoustic Doppler current profiler (ADCP) sampling of currents. The study found strong asymmetric response, with stronger currents to the right side of the track and weak or disorganized currents to the left, concurrent with Price (1981). The currents were also fairly uniform with depth, through roughly 100 m.

The Naval Research Laboratory (NRL) had deployed fourteen ADCPs in the northern Gulf of Mexico (GOM), as part of the Shelf Energetics and Exchange Dynamics (SEED) project. These ADCPs included six deployed along the outer continental shelf and slope

(depths ranging from 60 m to 90 m) and an additional eight deployed further off the shelf (depths ranging from 500 m to 1000 m). During the period of deployment, Hurricane Ivan (2004) moved over this ADCP array. The results were examined by Mitchell et al. (2005) and Teague et al. (2007), demonstrating 4 phases of ocean response. The first stage was represented as the time when the front half of the storm generated downwelling favorable wind conditions. Stage two occurred when the radius of maximum winds (~40 km of Hurricane Ivan) crossed the outer shelf. Stage three occurred when the rear half of the storm behind the eyewall crossed the outer shelf. Stage four was the relaxation stage as described in Price et al. (1994).

Stage one response was dictated as when the front half of the storm generated downwelling favorable wind conditions. Easterly winds ahead of the eye caused the Ekman transport vector to point towards the shoreline. Water moving towards the shoreline resulted in downwelling and this period was characterized by onshore advection in the upper water column and offshore advection of the lower water column across all six moorings. Given Ivan's average translation speed of  $6.3 \text{ m s}^{-1}$  in the Gulf of Mexico, stage one was estimated to be about fifteen hours. Some data of the wind stress component showed a linear decrease along with an increase in bottom temperature, suggesting pre-storm downwelling. Fifteen hours prior to eyewall arrival, temperatures increased at a greater rate due to downwelling. The fifteen hours of enhanced downwelling resulted in bottom temperatures rising about  $3 \text{ }^{\circ}\text{C}$  at all six stations.

The response to stage two (when the radius of maximum winds, or eyewall, crossed the outer shelf) included a rapidly deepening surface Ekman layer that extended nearly to the

bottom. Ekman layer thickness depends on friction velocity, which in turns depends on the magnitude of stress applied at each boundary. The wind stress increased monotonically until the eyewall moved over the outer shelf and then decreased. As a result, surface velocities increased and the Ekman layer thickened as the eyewall approached. As the surface wind stress dwarfed the bottom stress by an order of magnitude (1 hPa to 0.1 hPa), the Ekman layer took only four hours to deepen through to the bottom. Bottom velocities turned offshore at which point bottom temperatures increased about 4 °C due to downwelling. This study concluded that horizontal and vertical advection resulted in this rapid temperature increase.

The dominant response during stage 3 (when the rear half of the storm outside the eyewall crossed the outer shelf) was characterized near-bottom onshore flows with near-bottom temperature decreases. The rapid rotation of the surface wind stress vector to the left of the eye was a result of the translation of the storm, and eventually slowed surface currents greatly. As stage 3 progressed, the wind stress decreased and the surface Ekman layer thinned, but the bottom currents continued unaffected and rotated clockwise – which resulted in a strong onshore flow that decreased temperatures 11 °C in only six hours. In areas where the eye did not directly pass, the surface Ekman layer remained thicker and the currents became aligned along-shelf.

Stage four began after the hurricane passed but its termination was hard to discern. Immediately following Ivan was Hurricane Jeanne and then Ivan's circuitous track caused it to impact the GOM again, as a tropical depression. The storm speed was close to the inertial period for this area, and strong asymmetric across-storm-track inertial motions were the

result (Teague et al. 2007). Peak currents during this TC event were measured in excess of  $200 \text{ cm s}^{-1}$ . The relaxation stage response of inertial currents are demonstrated in Chapter 2 and referred for further investigation in Chapter 3.

One of the earliest studies of the response of SST to TCs utilizing satellite-derived infrared (IR) images of the western North Atlantic was undertaken by Cornillon et al. (1987) with Hurricane Gloria (1985) as the storm. As a very late-season storm, with the region composed mostly of a shallow and compressed seasonal thermocline, Gloria's impacts on SSTs were very pronounced. North of the Gulf Stream, in the Mid-Atlantic Bight (MAB), cooling was the most significant, up to  $5 \text{ }^\circ\text{C}$  was observed. The Sargasso Sea, further to the south, has a much thicker and diffused thermocline and the change in SST ( $\Delta\text{SST}$ ) was much less pronounced ( $\sim 3 \text{ }^\circ\text{C}$ ). Along the coastal waters, beyond the 20 m isobaths, the water column was mostly mixed and the impact of SST cooling was barely discernable. As demonstrated in Price (1981) with Hurricane Eloise (1981), the cross-track bias of  $\Delta\text{SST}$  was observed, with the left side featuring as much as a factor of 4 increase in  $\Delta\text{SST}$ .

Walker et al. (2005) demonstrated upwelling and *chlorophyll-a* enhancement in the wake of Hurricane Ivan (2004) utilizing composite GOES-12 nighttime images. Several pre-existing cyclonic eddies were located in the GOM, confirmed by measurement of SSH from altimeter data provided by Jason-1. After TC passage, the cyclonic eddies intensified and  $\Delta\text{SST}$  in these areas were enhanced, with maxima of  $-5.9 \text{ }^\circ\text{C}$  and  $-7.4 \text{ }^\circ\text{C}$  found along Ivan's track. Additional wind input from the TC contributed to increase cyclonic circulation, resulting in SSH changes of -5 to -20 cm between 9 September and 17 September (roughly capturing the pre- and post-storm periods). This drastic change in ocean condition occurred

over a large swath of ocean, approximately 38,000 km<sup>2</sup>. These measurements and methods will be utilized in comparison to experiments conducted with Hurricane Ivan in Chapter 2 of this dissertation. While the biological impacts of coupled modeling are not discussed in this dissertation, the impacts of TC-induced upwelling had significant impacts on the production of new phytoplankton to the surface, an area of future study.

#### *1.2.5. Ocean circulation impacts on reducing TC intensity*

So far, the impacts TCs have been demonstrated to reduce SST in the ocean domain through entrainment of cooler water and surface fluxes. However, the three-dimensional structure of ocean currents and eddies can further complicate the heat and momentum flux exchange between the ocean and hurricane (Walker et al. 2005; Rogers et al. 2006; Liu et al. 2012b). Bender et al. (2007); Shay et al. (2008); Wada et al. (2010; 2013; 2014) suggest the importance of initializing coupled models with realistic warm and cold ocean features in the global oceans. Wada et al. (2014) and Ma et al. (2013) use a simplified atmosphere-ocean coupled model and idealized TC to quantify the effects of ocean eddies on TC intensity

Oey et al. (2006; 2007) investigate the impacts of Hurricane Wilma (2005) translating through the Yucatan Strait into the GOM. Wilma originated from a region of extremely high ocean heat content (OHC). This variable is described in Leipper and Volgenau (1972) as

$$OHC = \rho_0 C_p \int_{Z_{26}}^{\eta} (T - 26) dz, T \geq 26 \text{ } ^\circ\text{C}$$

where  $Z_{26}$  (greater than 0 m) is the depth of the 26 °C isotherm,  $\eta$  is the SSH,  $\rho_0$  is the density of the sea water, and  $C_p$  is the specific heat of the sea water. Regions of OHC greater

than  $60\text{-}90 \text{ kJ cm}^{-2}$  have been found to be conducive to storm intensification Oey et al. (2007).

This value is dependent on the dynamics of the upper-ocean. Upwelling and vertical mixing both contribute to raise the depth  $26^\circ\text{C}$  isotherm ( $Z_{26}$ ) and reduce the value of the temperature at the surface (T), thereby reducing the value of OHC. Flow divergences (and convergences) are demonstrated in Oey et al. (2006; 2007) to have drastic impacts on hurricane intensity. Hurricane Wilma (2005) maintains the record as the most intense TC on record in the Atlantic basin, with a minimum central pressure of 882 hPa (Pasch et al. 2006; Beven et al. 2008), in part due to the vast supply of energy it obtained from high OHC (Pasch et al. 2006; Oey et al. 2006; 2007).

Oey et al. (2006; 2007) utilized an ocean model driven by atmospheric winds to demonstrate the ocean effect of Hurricane Wilma. The model used was the Princeton Regional Ocean Forecast System (PROFS), based off of the original Princeton Ocean Model (POM; Blumberg and Mellor 1987). The initialization wind field was pulled from the Global Forecast System (GFS) winds rerun using analyzed winds from the Hurricane Research Division of the NHC (H\*WIND, Powell et al. 1996; 1998). In his configuration, PROFS utilizes wind stress from a wind-speed limited drag coefficient ( $C_d$ ), similar to that used in Donelan (2004), Davis et al. (2008), Liu et al. (2010) and Moon et al. (2004b) in order to compensate for wave de-coupling in high wind regimes. The wind-speed limited drag coefficient ( $C_d$ ) is calculated by the following function,

$$\begin{aligned}
C_d \times 10^3 &= 1.2, |u_a| \leq 11 \text{ms}^{-1} \\
&= 0.49 + 0.065|u_a|, 11 < |u_a| \leq 19 \text{ms}^{-1} \\
&= 1.364 + 0.0234|u_a| - 0.00023158|u_a|^2, 19 < |u_a| \leq 100 \text{ms}^{-1}
\end{aligned}$$

where  $|u_a|$  represents the magnitude of wind speed. The model used in Oey et al. (2006; 2007) did not feature any surface fluxes, so any simulated shelf cooling was due to upwelling and mixing.

Utilizing this model, Oey et al. (2006; 2007) removed the Loop Current from the simulation. In analyzing the experiment versus the control simulation, the experiment demonstrated the Loop Current was responsible for advecting a substantial amount of ocean water with high OHC away from the storm. Without this high OHC water, Hurricane Wilma weakened significantly after moving through the Gulf of Mexico and would have impacted Florida as a much more intense storm. This is one example of how the general circulation of the ocean has an impact on storm intensity, an impact that would not be possible to simulate without coupling to a three-dimensional ocean model. Bender et al. (2007) notes that in addition to utilizing a three-dimensional ocean model, the realistic initialization of the three-dimensional density and velocity fields in the ocean model is critical for proper simulation of the ocean response, as SST response to TC winds is sensitive to upper-ocean structure (Ginis 2002).

#### *1.2.6 TC precipitation effect on ocean salinity*

The introduction of precipitation to the ocean surface imparts a fresh layer of water to the first few layers of the ocean surface. Fresh water, with a lower density, has the effect of

creating a stable layer at the ocean's surface (Price 1979). The result of this could be to reduce the overall mixing that occurs to the sea surface, which would have an impact on feedback to the atmosphere. At the same time, the fresh water precipitation to the ocean surface would likely be cooler than the surface water, especially in the tropics. Price (1979) describes a shallow (<20 m) rain-formed mixed layer which is thoroughly stirred and homogenous in density while rapidly deepening.

Bao et al. (2003) utilizes the POM model with high vertical resolution in the surface layers, as small as 1 m. This vertical grid spacing is necessary as the ocean's response to the surface atmospheric forcing by precipitation occurs within in the upper few meters of the ocean. Running an idealized simulation, with  $15 \text{ mm hr}^{-1}$  of precipitation falling over 5 hours in a 100 km circle, Bao et al. (2003) found a maximum salinity anomaly of -0.3 to -0.35 psu within the top 2-3 m in five hours, and with a small (-0.05 psu) anomaly contour reaching below 10m depth. The stable layer gradually mixed over the course of few hours decreasing the magnitude of the anomaly but spreading it to a depth of 11-13 m. This modeled data correlates well with observations taken during a similar storm that took place during the Tropical Ocean Global Atmospheres/Coupled Ocean Atmosphere Response Experiment (TOGA/COARE) in the western Pacific warm pool, at  $156^\circ\text{E } 2^\circ\text{S}$ .

In order to examine the impact of this stable, fresh water layer, Bao et al. (2003) utilized the model conditions to determine the impact of a  $200 \text{ W m}^{-2}$  downward shortwave radiation head flux applied directly to the surface. These results are compared to a control case where there is no precipitation-induced stable layer. The findings of Bao et al. (2003) determined that increased SST anomaly of  $0.13^\circ\text{C}$  is noted in the case with the precipitation-

induced stable layer, nearly three times larger than the case with no precipitation-induced stable layer (0.035 °C). Likewise, the warming of the upper-layers of the ocean lasted longer in the case where there was a precipitation-induced stable layer. As a result, the rainfall-induced fresh layer responds to warming much more rapidly than the rest of the ocean.

The Bao et al. (2003) study concludes that the upper-ocean responds to surface forcing from the atmosphere much more rapidly when precipitation has formed a stable layer at the surface. However, it notes that a two-way coupled model including ocean-to-atmospheric feedback would be necessary to further study the phenomenon.

In a study of rain-induced surface salinity anomalies, Asher et al. (2014) utilizes observations of the surface and 1-2 m beneath to determine the extent of salinity anomalies in the near-surface. This study was undertaken due to freshwater input effecting salinity gradients reducing the sea surface salinity reported by satellite L-band microwave radiometers such as SMOS and Aquarius. The freshwater flux to the ocean surface is a key component of the global water cycle. Understanding the spatial variability of sea surface salinity is an important component of determining precipitation flux to the ocean. Comparing satellite-derived salinity to ARGO floats normally produces agreement to within ~0.1psu, however in the region of recent precipitation, this number can increase to as much as a few tenths of PSU.

A surface following towed profiler, positioned well away from the wake of the ship, was able to determine the surface salinity gradient in the first few meters of ocean. Asher et al. (2014) determined that rain-induced salinity anomalies could impact remote sensed salinity measurements within the first few meters of the ocean. However, with the

introduction of a moderate wind speed ( $\sim 5\text{-}7\text{ ms}^{-1}$ ), the appearance of an upper-ocean salinity gradient did not last for more than a few hours.

Rain-induced surface salinities also have an effect on the sea surface roughness, especially at low wind speeds. Boutin et al. (2014) has shown this to cause inaccuracy in determining satellite-derived salinity retrievals, freshening the surface salinity by as much as 0.7psu. Boutin et al. (2014) compared surface drifters, measuring salinity at 45 cm of depth with satellite-derived surface salinity across several bins of wind ranges. In the  $>15\text{ m s}^{-1}$  bin, of interest to TC study, demonstrate  $\sim 0.5\text{psu}$  of freshening in the upper 45cm of water with  $\sim 8\text{ mm hr}^{-1}$  of rainfall, when compared to satellite-derived surface salinity. As a result, despite mixing induced by high winds, a moderate  $\sim 8\text{ mm hr}^{-1}$  precipitation event is enough to generate a salinity gradient in the upper meter of ocean. The impact of precipitation and wave-induced mixing on ocean salinity will be explored in Chapter 4.

### *1.2.7 TC interaction with wave environment*

The accurate prediction of the wave environment is also of importance in the numerical simulation of a TC because it improves prediction of wind speeds, fluxes, and oceanographic mixing (Chen et al. 2007; Moon et al. 2007; Wada et al. 2010; Liu et al. 2010; 2012a; Chen et al. 2013; Wada et al. 2014). These wave environment feedback mechanisms are crucial to resolving a moving TC in the atmosphere and oceans. Uncoupled wave models have demonstrated good skill, so long as the wind forcing fields are accurate (Fan et al. 2009). However, the variable swirling winds in a TC can be difficult to capture using coarse global meteorological models, which are used by global wave models for surface forcing. In

addition, most wind-wave models treat their surface roughness as a scalar quantity (Bao et al. 2000; Doyle 2002). In the TC environment, the winds are highly variable and the surface stress vector is not always aligned with the local wind vector (Chen et al. 2007, 2013), therefore the surface roughness has a directionality component. The coarse grid spacing of the utilized wind fields and the treatment of surface roughness as a scalar quantity result in poor accuracy from uncoupled wave models.

The wave environment has a large effect on the surface heat, moisture and momentum fluxes to the TC as well as energy input into the ocean velocity field (Liu et al. 2010; 2012a; Chen et al. 2007; Warner et al. 2010; Olabarrieta et al. 2012; Kumar et al. 2012). Uncoupled models do not consider wave height, period, and length as variable over the spatial domain. Large, steep waves increase the surface roughness length, which results in a larger surface area from which the TC is able to transfer fluxes of heat, moisture, and momentum to the ocean (Chen et al. 2007; Liu et al. 2010).

An examination of wave impacts is conducted using the coupled atmosphere-wave-ocean modeling system (CAWOMS; Liu et al. 2010; 2012a) Building a wave state results in frictional effects on the TC wind field, which has two effects: decrease the strength of the wind speed, and modify the sensible heat flux. The modification to sensible heat flux has both positive and negative contributions. The extreme winds found in a TC have an effect on sensible heating, caused by the frictional force of the wind itself on the ocean surface through a process known as dissipative heating. Dissipative heating in the lower atmosphere results in increased heat, increasing overall sensible heat flux. To examine the negative feedback

mechanism, first an examination of the sensible heat flux is conducted by review of Csanady (2001).

Sensible heat fluxes passed from the atmosphere to the ocean are primarily a result of two factors: air temperature and wind. The effect of air temperature on the ocean surface is evident as the difference in temperature between the air and ocean surface is paramount in determining the rate of most other fluxes. When a stronger gradient of temperature exists between the sea surface and air, there is more active diffusion of heat and moisture across this boundary. This is expressed in the following equation (Csanady 2001),

$$\rho c_p \frac{\partial \theta}{\partial t} = - \frac{\partial Q}{\partial z}$$

where  $\rho$  is the density,  $c_p$  is the specific heat at constant pressure,  $\theta$  is the temperature,  $t$  is time,  $Q$  is the heat flux,  $z$  is the height of the interface. This formulation can be expressed in a force-flux relationship, which is more useful for our purposes as,

$$Q = -k_t \frac{\partial \theta}{\partial z}$$

where  $k_t$  is the air-sea interface conductivity. The difference in temperature therefore has drastic effects on most other fluxes. An increase in air temperature due to dissipative heating would therefore increase the gradient of temperature down to the sea surface, reducing sensible heat flux.

From Liu et al. (2012a), the equation for dissipative heat introduced per unit time is expressed as,

$$\frac{dT}{dt} = \frac{\nu_a u_*^2}{C_p z_1}$$

where  $C_p$  is the air specific heat at constant pressure,  $z_1$  is the height of the model surface layer,  $V_a$  is the wind speed at the lowest semi- $\sigma$  layer, and  $u^*$  is the frictional velocity. As demonstrated in the equation, the introduction of dissipative heat is a function of the cube of wind stress. As a result, minor fluctuations in wind stress can yield drastic differences in the dissipative heat generated.

In addition to providing additional frictional effects (Chen et al. 2007; Liu et al. 2010; 2012a), sensible heating (Liu et al. 2010; 2012a), and dissipative heating, additional latent heating could be provided by contributions of sea spray from the wave environment (Liu et al. 2010; 2012a). A brief review of latent heating from Csanady (2001) follows from the review of sensible heating. At the interface, the transfer of moisture is dependent on the differential of temperature as well as moisture content. While similar to the air-sea temperature flux, the flux of moisture is dependent on the differential of moisture between the atmosphere and ocean. It is obvious that the ocean is saturated; therefore, the transfer of moisture to the atmosphere is dependent on the content of moisture in the atmosphere. A dry lower atmosphere enhances this flux. The amount of moisture transmitted to the atmosphere as vapor then warms the atmosphere after condensation. The latent heat source to the atmosphere is what strengthens and maintains the TC. The opposite effect is found in the ocean, the transfer of latent heat to the atmosphere depletes the ocean of heat.

Another source of heat loss to the atmosphere is due to sea spray. In the extreme wind environment of the TC, large breaking waves result in sea foam and spray. Research into this additional source of latent heating has resulted in many recent publications (Chen et al. 2013; Liu et al. 2012a; Bao et al. 2011; Liu et al. 2010; Xie et al. 2010; Liu et al. 2008;

Bender et al. 2007; Chen et al. 2007; Wang and Wu 2004; Moon et al. 2004b,a; Fairall et al. 2003; Powell et al. 2003; Andreas and Emanuel 2001; Bao et al. 2000). Tiny droplets of water from the ocean are introduced to the atmosphere, and may evaporate in the lower layer, turning into vapor. However, Andreas and Emanuel (2001) is careful to note that spray cannot affect the net enthalpy transfer, and that the marine boundary layer must supply the latent heat required to evaporate the spray (Bao et al. 2000). As a result, some of the spray may not evaporate and some may fall back into the sea as re-entrant droplets to the ocean. Spray that does evaporate does so at the latent heat of vaporization, which results in lower air temperature that in turn enhances the sensible heat flux of the warm ocean to the atmosphere. This process depletes the ocean of additional heat and is an important consideration in coupled modeling studies of TCs.

Having investigated sensible and latent fluxes due to wave interaction, the remaining flux is momentum. Uncoupled wave models are less reliable in environments of strong wind forcing. The variable swirling winds in a TC can be difficult to capture using global meteorological models, which are used by global wave models for surface forcing (Chen et al. 2007, 2013). In the TC environment, the winds are highly variable and the surface stress vector is not always aligned with the local wind vector (Chen et al. 2007; 2013). As a result, the challenges in accurate wave prediction using uncoupled wave models is the poor resolution of the wind fields generated for the wave model, as well as the treatment of surface roughness as a scalar quantity. Fan et al. (2009) finds that a growing surface wave field can take a significant fraction of the momentum flux from the air. Translating down through the water column, dissipating wind momentum to build waves resulted in as much as

a 6% reduction in subsurface currents. This had the consequence of reducing the sea surface cooling to the right of the storm track.

Wave interaction also applied changes to ocean currents, demonstrating the importance of the accurate prediction of the wave environment in the numerical simulation of the ocean condition beneath a TC (Chen et al. 2007; Liu et al. 2010; 2012a; Kumar et al. 2012; Fan et al. 2009). Fan et al. (2009) uses a coupled wind-wave-current model in order to examine the interaction between these environments. Inclusion of wave-current interaction had the effect of reducing the momentum into the ocean in the right-rear quadrant of the TC by 6%, where the wave field had the largest spatial gradients. The wave field was significantly reduced in the right-front quadrant of the TC, from 17.0 m to 14.7 m. Also, in this quadrant of the storm, wind-current interaction resulted in the subtraction of the surface current velocity from the wind speed when the wind and current vectors are closely aligned produced a reduction of  $\sim 0.2 \text{ ms}^{-1}$  in current speed.

#### *1.2.8 Additional sources of TC intensity prediction errors*

A review of impacts on TC intensity prediction errors would be remiss without mentioning several additional sources of TC intensity forecasting error. These include poor representation of inner-core dynamical processes (such as eyewall replacement cycles) and poor model initial conditions (Wang and Wu 2004; Davis et al. 2008; Fowle and Roebber 2003; Done et al. 2004; Gopalakrishnan et al. 2012). Improvements in the representation of inner-core dynamical processes are a multi-scale problem, as the TC inner-core interacts with the larger-scale environment (Wang and Wu 2004; Davis et al. 2008). Resolving the inner-

core of a TC with a grid spacing of less than 4 km has been shown to allow the use of explicit representation of convection, which has resulted in better structure of the TC (Fowle and Roebber 2003; Done et al. 2004). Gopalakrishnan et al. (2012) demonstrates the improvement in TC intensity forecasts by decreasing nested grid spacing from 9 km to 3 km, which the current Hurricane Weather Research and Forecasting (HWRF) operational model uses. Intensity also suffers from poor initial conditions and is a result of poor initial TC structure (Gopalakrishnan et al. 2012). Improvement of the initial structure of TCs is currently being examined through the use of data assimilation (Davis et al. 2008).

#### *1.2.9 Review of other coupled modeling studies*

In addition to the aforementioned coupled model studies, there have been several published in the last decade of coupled model simulations of TCs, including: (Bao et al. 2000; Bender and Ginis 2000; Bender et al. 2007; Chen et al. 2013; Khain et al. 2000; Lee and Chen 2014; 2012; Liu et al. 2012a; 2010; 2008; 2012b; Wada et al. 2013; Xie et al. 2010; Yablonsky and Ginis 2009). These studies are organized with their component coupled parts in Table 1.1. As a broad review of these numerous studies, we will attempt to separate them first by complexity of coupling (e.g. ocean-atmosphere, atmosphere-wave, ocean-atmosphere-wave) and then by modeling system (e.g. COAMPS, GFDL, CAWOMS, etc) when multiple papers are available for the same model.

Khain et al. (2000) utilized a coupled primitive equation model consisting of an eight-layer atmosphere and a seven-layer primitive ocean model in order to study the motion and evolution of binary TCs. Twelve TCs were separated by 640 km, 800 km, or 1440 km and at

15 °N. Ocean coupling was activated in four of the models. Interestingly, through ocean coupling, this study was able to demonstrate influence in storm tracks as a result of decreasing the mutual orbiting velocities of the TC pairs. Ocean coupling also resulted in decreasing the difference in intensities by reducing the intensity of the stronger storm of the pair. Ocean interaction with the interacting TCs also created differences in their type of interaction (partial or complete merging, mutual straining, complete straining, or elastic interaction).

Bender and Ginis (2000), Bender et al. (2007), and Yablonsky and Ginis (2009) utilized the NOAA Geophysical Fluid Dynamics Laboratory (GFDL) hurricane model described in Kurihara et al. (1995) coupled with the POM developed by Blumberg and Mellor (1987). The GFDL hurricane model described in Kurihara et al. (1998) was used to model the TC. The model is a primitive equation model formulated using latitude, longitude, and sigma ( $\sigma$ ) coordinates (18 levels in the vertical). A triply nested movable mesh (of 1°, 1/3°, 1/6° grid spacing, respectively) was used with the GFDL to represent TC features on a finer scale. The parent domain was set based on the TC's initial and 72 hour locations, the two child domain meshes follow the storm center. The GFDL model was run using a cumulus parameterization scheme described in Kurihara (1973) with some changes from Kurihara and Bender (1980), appendix C. Surface flux calculation was done by using the Monin and Obukhov (1954) scheme. A level-two turbulence closure scheme from Mellor and Yamada (1974) was applied with a background diffusion coefficient added.

The POM (Blumberg and Mellor 1987) was chosen for use in Bender and Ginis (2000), Bender et al. (2007), and Yablonsky and Ginis (2009) due to highly accurate

representation of upper ocean mixed layer physics, a requirement for accurately reproducing the horizontal and vertical mixing processes under a TC. It is a three-dimensional, primitive equation model with thermohaline dynamics. The vertical levels are based on a terrain-following sigma ( $\sigma$ ) coordinate. The second-order turbulence closure scheme described in Mellor and Yamada (1982) is employed to provide mixing parameters so that surface mixed layer dynamics are well represented. One of two ocean domains were specified based on the case they were studying (in the GOM or the western Atlantic). A  $1/6^\circ$  grid spacing was used for both ocean domains. 21 and 23 vertical layers were specified for the GOM and western Atlantic domains, respectively. Two land-ocean lateral boundaries were closed using a no-slip condition in the velocity field. The two open lateral boundaries utilized transport and thermal observations available at the time.

Utilizing this GFDL-POM coupled configuration, Bender and Ginis (2000) examined four realistic cases: Hurricanes Opal (1995) and Gilbert (1988) in the GOM, and Hurricanes Felix (1995) and Fran (1996) in the western Atlantic. Several experiments were run comparing uncoupled and coupled model cases. The initial atmospheric fields for the GFDL hurricane model were derived using a scheme from Kurihara et al. (1995; 1998). The NCEP T126 global analysis and storm messages from the NHC were merged to provide the best wind field generation. Producing axisymmetric and symmetric components of the TC within the environmental fields from the global analysis is a technique known as producing a bogus vortex (Singh et al. 2005). Lateral boundaries for the hurricane model were established using the NCEP global model.

Hurricane Gilbert (1998) made landfall on the eastern edge of the Yucatan peninsula, and quickly re-entered the Gulf of Mexico over the northern edge. After re-entering the Gulf, Gilbert experienced a slight 4 hPa deepening to 946 hPa as it translated westward before making landfall in Mexico 48 hours later. The operational GFDL forecasting model, without ocean coupling, had incorrectly deepened the storm 25 hPa to 934 hPa over that same period, an over-intensification of 22 hPa (Bender and Ginis 2000). Utilizing the coupled model in Bender and Ginis (2000), the forecast was much closer to the observed with the storm deepening about 10 hPa to 940 hPa, over-intensifying it merely 6 hPa.

Simulations of Hurricane Opal (1995) in Bender and Ginis (2000) suffered from time incongruity to verification, the modeled storm moving too quickly and making landfall too soon. Comparing forecast intensity to a time-shifted verification also demonstrates that the model's  $1/6^\circ$  resolution was not able to deepen Opal as intensely as the verification provided. Ocean coupling had the most important effect on Opal during the initial part of the forecast, when Opal drifted to the north at a slow rate of speed. During this period, as Opal moved slowly through the GOM the SST decreased rapidly underneath the storm. As a result, the coupled solution most closely represented the intensity of the storm, as the uncoupled storm intensified much quicker than realized.

Simulations of Hurricane Felix (1995) in Bender and Ginis (2000) demonstrated better timing than Opal across all experiments. The coupled model resolved cross-path SST changes well, with a strong rightward bias apparent but weakening as the storm's translation speed slowed in the Sargasso Sea. After a 72 hour forecast, the minimum sea level pressures were 963 hPa (verification), 960 hPa (coupled) and 945 hPa (uncoupled). This SST cooling

due to the storm's slow translation speed through the Sargasso Sea led to a decrease in intensity in verification and the coupled solution. Clearly, the uncoupled solution had over-intensified the storm.

Hurricane Fran (1996) was unique in the Bender and Ginis (2000) study because Fran followed in the wake of another major hurricane, Hurricane Edouard (1996). As a result of the cold wake from Hurricane Edouard, Fran only deepened to 963hPa. The coarse grid spacing of the National Center for Environmental Prediction (NCEP) SST analysis, utilized in the operational model, was unable to resolve the cold wake generated by Edouard. As a result, the operational uncoupled GFDL model incorrectly deepened Fran to 941 hPa in 72 hours, an over-intensification of 22 hPa. Another uncoupled simulation was executed, this time correctly resolving the cooler SSTs from Edouard, and the model intensified Fran to 951 hPa, an over-intensification of 12 hPa. A similar result was achieved by running the coupled model utilizing the sparse NCEP SST data. The closest result was when the coupled model was run with Edouard's wake resolved, which resulted in Fran having a 957 hPa minimum pressure after 72 hours.

Bender et al. (2007) is a summary paper describing major upgrades to the GFDL hurricane forecasting model from 1998 through 2006. Upgrades to the GFDL system during this period (date indicated as operational in parentheses) included coupling to the POM (2001), major physics upgrades (2003 and 2006), increases to vertical grid spacing (2003) and horizontal grid spacing (2002 and 2006). During a GFDL coupled model forecast, the POM is initialized by a diagnostic and prognostic spin up of the ocean circulation using available real-time and climatological ocean data, implemented as in Bender and Ginis

(2000). The upgraded GFDL model (including coupling to POM) performed much better in simulating the active 2004 and 2005 hurricane seasons. Marked improvement to forecasts were found in Bender et al. (2007) by reducing positive intensity bias by 5% to 22%.

The final paper examined that utilized GFDL coupled to POM is from Yablonsky and Ginis (2009). This study examines differences in SST cooling as a result of using one-dimensional and three-dimensional configurations of the POM. The one-dimensional configuration of POM removes advection and pressure gradient terms so that there is no interaction among surrounding grid points in the horizontal. The result is a one-dimensional model similar to the OML in Pollard et al. (1972) and Davis et al. (2008), except the one-dimensional POM is treated as a level model instead of a layer model (Ginis 1995). The result in Yablonsky and Ginis (2009) demonstrates a drastic impact for slow moving storms. As a result of not resolving upwelling (in the one-dimensional configuration), SST cooling is not accurately captured for storms moving  $<5 \text{ m s}^{-1}$ . For very slow moving storms,  $<2 \text{ m s}^{-1}$ , the storm-core SST cooling is reduced by more than half. As more than half of the TCs in the North Atlantic basin translate at speeds  $<5 \text{ m s}^{-1}$ , this result is significant to resolving SST cooling in this region.

Lee and Chen (2014), Chen et al. (2013), and Lee and Chen (2012) utilize the University of Miami Fully Coupled Atmosphere-Wave-Ocean Modeling system (UMCM, introduced by Chen et al. 2007) which includes components for atmosphere, surface wave, and ocean circulation models. The atmospheric model may either be configured as the fifth-generation Pennsylvania State University–National Center for Atmospheric Research Mesoscale Model (MM5; Grell et al. 1994) or the Weather Research and Forecasting (WRF;

Skamarock et al. 2008) model. The ocean model is the three-dimensional Price-Weller-Pinkel (3DPWP) upper-ocean model from Price et al. (1994). The wave model is WAVEWATCH III (WW3) from Tolman (1991).

Lee and Chen (2014) utilizes the atmosphere-ocean (WRF-3DPWP) coupled configuration of UMCM in order to examine the physical processes that occur within the atmospheric boundary layer of TCs by using Supertyphoon Choi-Wan (2009) as a test case. The results in Lee and Chen (2014) indicate that while the SST cooling due to ocean coupling would reduce TC intensity, a persistent stable boundary layer is found to form over the cold wake within the TC's right-rear quadrant. This stable boundary layer influences TC structure by suppressing convection in rainbands downstream of the cold wake and enhancing the boundary inflow into the inner core by increasing inflow angles over strong SST and pressure gradients. Air in the stable boundary layer stays in the boundary layer longer and gains extra energy from surface heat and moisture fluxes. In addition, enhanced inflow helps transport this high-energy air in the stable boundary layer into the eyewall and TC core, increasing storm efficiency. Lee and Chen (2014) find that without ocean coupling and a TC-induced cold wake and an stable boundary layer, the air in the right-rear quadrant within the boundary layer tends to rise into local rainbands.

Chen et al. (2013) uses the atmosphere-ocean-wave (MM5-3DPWP-WW3) configuration of the UMCM model in order to investigate improvements to coupled parameterizations sought through the Coupled Boundary Layer Air-Sea Transfer (CBLAST)-Hurricane field program (2004; Chen et al. 2007; 2013). Part of Chen et al. (2013) is into integrate a directional wind-wave coupling algorithm to include the directionality component

of winds and waves in hurricanes, rather than just utilize the traditional roughness scalar. Hurricane Frances (2004) featured the most data acquired during the CBLAST-Hurricane project and is utilized as a test case. Results in Chen et al. (2013) demonstrate that the uncoupled atmosphere model overintensified the TC, and the atmosphere-ocean coupled model produced the best intensity. The fully-coupled atmosphere-wave-ocean configuration in Chen et al. (2013) produced the most accurate wind field, lending some credence to the argument for wind-wave directional coupling. A case examining the same storm but with comparison to the Donelan (2004) treatment of surface roughness with a WRF-3DPWP-WW3 configuration is referred for future study.

Lee and Chen (2012) configures the UMCM model with atmosphere-ocean-wave (MM5-3DPWP-WW3) coupling, as in Chen et al. (2013) but without the directionality component of wind-waves taken into account. Utilizing this configuration of the coupled model, Lee and Chen (2012) investigate the upper ocean and air-sea interface connection to the atmospheric boundary layer in TCs. As in Chen et al. (2007; 2013), Hurricane Frances (2004) is used as a test case with comparisons to data acquired during the CBLAST-Hurricane project (2004; Chen et al. 2007; 2013). This study found that atmosphere-ocean coupling reduces the mixed-layer depth in the right-rear quadrant due to storm-induced SST cooling, whereas the wind-wave coupling enhances boundary inflow outside the radius of maximum wind. The fully coupled atmosphere-wave-ocean model produced the best storm intensity and structure in terms of the wind, surface values, and vertical profiles of  $\theta_v$  and  $\theta_e$ . According to Lee and Chen (2012), the complex, three-dimensional asymmetric structure in both thermodynamic and dynamic properties of the hurricane boundary layer indicate that it

would be difficult to parameterize the effects of air–sea coupling without a fully coupled model. The results in Lee and Chen (2012) are validated by dropsonde observations and surface wind fields observed by NOAA WP-3D aircraft research flights during the CBLAST field campaign (Chen et al. 2007; 2013).

One of the earliest ocean-atmosphere-wave coupled models was utilized in Bao et al. (2000), featuring coupling between the POM, MM5, and a surface gravity wave model (ocean wave model, WAM; The WAMDI Group 1988). Hurricane Opal (1995) is used as a test case to investigate the scenario of a TC passing over an initially warm water surface. Utilizing ocean cooling, the modeled environment is not sufficient to maintain an intense TC. Introduction of sea spray in Bao et al. (2000) had an additive effect of enthalpy transfer under extreme wind conditions, resulting in the intense storm maintaining itself throughout the simulation. However, Bao et al. (2000) is careful to note that the sea spray parameterization was utilized for a single case and that without observations, may or may not be accurate.

The only instance of atmosphere-wave coupling demonstrated in this review is from Liu et al. (2008). This coupled atmosphere-wave model uses WRF-WW3 coupling in order to investigate the impacts wave state has on sea spray generation, dissipative heating, and resultant heat flux. Experiments featuring increased surface roughness affected by wave state and sea spray reduced the idealized TCs intensity by 6 hPa and decreased significant wave height by 6%, however maximum 10 m wind was increased by 2% due to decreased drag coefficient. Including dissipative heating increased the air-sea heat flux by 16% resulting in increases of 13% to the surface wind speed and 9% to the significant wave heights. With full atmosphere-wave coupling, the idealized TC in Liu et al. (2008)

intensified by 10.7 hPa, strengthened by 14% and had significant wave heights that were 4% greater.

Xie et al. (2010) utilized the Coupled Regional Ocean and Weather Numerical (CROWN) modeling system in order to examine ocean-TC interaction. This model was comprised of WRF, POM, and WW3 and used Hurricane Katrina (2005) as a test case to examine impacts to the TC, surface waves, and simulated storm surge. Xie et al. (2010) demonstrate important contributions from coupling of the air-sea and wind-wave interactions, as well as impacts to simulated TC intensity, storm surge and waves. The storm surge predicted by the model was well simulated, however largely under-estimated due to the large grid spacing (12 km) of the atmospheric model. Also, the coupled configuration featuring storm surge from POM did not utilize simulation of SST and surface salinity fields, the WRF model utilized analyzed SST fields from GFS data.

Liu et al. (2012b) also uses a WRF-POM-WW3 configured model, however not under the same framework as the Xie et al. (2010) CROWN model. Liu et al. (2012b) investigate the impact of ocean coupling on wind-current interaction, using Typhoon Kaemi (2006) as a test case. Liu et al. (2012b) demonstrates improvement to TC prediction by preventing excessive momentum fluxes from being transferred into the upper ocean. A consequence of this is a reduced turbulent kinetic energy (TKE), horizontal and vertical diffusivity, and horizontal advection. As a result, the SST cooling from wind-current interaction is reduced and does not begin to make an impact on storm intensity until the TC reaches its peak and begins to upwell water from beneath the thermocline. In Liu et al. (2012b), the reduced SST cooling due to inclusion of wind-current interaction results in a better simulation of the TC.

Liu et al. (2010) developed the Coupled Atmosphere-Wave-Ocean Modeling System (CAWOMS), later used in Liu et al. (2012a). As in CROWN (Xie et al. 2010), the model features coupling between the WRF and POM models. However, instead of WW3, CAWOMS uses the Simulating Waves Nearshore (SWAN; Booij et al. 1999) to simulate surface waves. In Liu et al. (2010), the authors use an idealized TC in order to examine the impact of sea spray and wave state on sea surface roughness, sea spray on heat fluxes, and dissipative heating in atmosphere-wave coupling. Liu et al. (2010) concludes that the impact of atmosphere-wave coupling strengthens the TC due to wave-state-dependent drag coefficient reduction with the introduction of sea spray. The inclusion of sea spray and dissipative heating increases air-sea heat flux, increasing the entropy to the TC. Atmosphere-ocean coupling has the impact of reducing the heat flux to the atmosphere (dependent on the thickness of the mixed layer), reducing TC intensity and strength.

Liu et al. (2012a) follows Liu et al. (2010) using the same configuration of CAWOMS in order to investigate the wind-wave effects on the intensity and strength of an idealized TC. Liu et al. (2012a) demonstrated weakening of the TC due to increasing surface roughness by using a sea surface roughness that accounts for sea spray and wave state, rather than the Charnock (1955) relation. The results are similar to Liu et al. (2010), where atmosphere-wave coupling increased area-averaged (latent) heat flux 22% (31%) beneath the TC, increased the intensity of the uncoupled TC by 16.4 hPa, the maximum wind speed by 31%, and the significant wave height by 4%.

The final coupled modeling study features a regional atmosphere-wave-ocean coupled model from Wada et al. (2013). This study, using Typhoon Choi-wan's (2009)

transit through the Kuroshio Extension system, featured coupling between the nonhydrostatic atmosphere mesoscale (NHM) model, a multilayer ocean model based on Bender et al. (1993) and developed at the Meteorological Research Institute (MRI), and a third-generation wave model developed by MRI (MRI-III) and the Japan Meteorological Agency. Without use of field observation data from the middle latitudes of the North Pacific, Wada et al. (2013) do not make comparisons to verification data, but rather examines results of sensitivity experiments. Utilizing different combinations of initial ocean conditions, Wada et al. (2013) demonstrate minor change in TC track, but ~10 hPa difference in simulated intensity. Where there was data to be validated against, a single buoy within the Kuroshio Extension (hundreds of kilometers off of the coast of Japan), the model performs poorly, with minimal improvement to changing initial conditions in the ocean state.

Through careful review of previous studies in air-sea interaction, TC dynamics, and coupled modeling systems the motivation for this dissertation work is strengthened. The remaining chapters will discuss coupling through the Coupled Ocean-Atmosphere-Wave-Sediment Transport (COAWST; Warner et al. 2010) model. Sediment transport will not be discussed, however it is enabled through use of the Community Sediment Transport Model coupled to ROMS.

Based on the existing state of knowledge, it is hypothesized that coupled modeling systems will provide improvement to the prediction of hurricane intensity, environmental states of surface waves and sea surface temperature, and atmospheric impact from precipitation distribution. This is demonstrated with 3 different tests of Hurricanes Ivan (2004), Sandy (2012), and Irene (2011). Chapter 2 will discuss interaction with Hurricane

Ivan (2004), Chapter 3 will discuss the tropical and extratropical cyclone Sandy (2012), and Chapter 4 will describe modeling experiments with Hurricane Irene (2011). This will wrap up with broad conclusions from this literature review and case studies in Chapter 5.

## **2 Hindcast experiments of Hurricane Ivan (2004) utilizing the Coupled Ocean-Atmosphere-Wave-Sediment Transport (COAWST) model**

### *2.1 Introduction*

In this chapter we investigate the impacts of ocean coupling to the accuracy of hurricane track and intensity prediction using a series of numerical investigations of increasing complexity by adding more coupling components and physics. Due to its extreme intensity, breadth of data in the atmosphere-ocean-wave environments, and large economic and environmental impacts, Hurricane Ivan was chosen as the first case study of this dissertation to employ the Coupled Ocean-Atmosphere-Wave-Sediment Transport (COAWST) model (Warner et al. 2010). The COAWST model has been used to study several other coastal storms and their effects on the atmosphere, ocean, and wave environments. These cases include simulations of TCs (Warner et al. 2010), strong Nor'easters (Nelson and He 2012), as well as storms undergoing extra-tropical transition (Olabarrieta et al. 2012). The work contained in this chapter is carried over from Zambon (2009), with key improvements to the storm hindcast and new analysis and has been published in Zambon et al. (2014).

This TC was an extremely intense Saffir-Simpson Category-5 (winds  $\geq 70 \text{ ms}^{-1}$ ) hurricane when it moved through the Caribbean Sea, weakening slightly to a strong Saffir-Simpson Category 3-4 (wind speeds  $50\text{-}70 \text{ ms}^{-1}$ ) hurricane as it moved through the Gulf of Mexico (GOM) in September 2004, devastating the oil and natural gas industry (Teague et al. 2007). This was a unique hurricane in that it intensified rapidly (maximum wind speed increase of  $> 15 \text{ ms}^{-1}$  within 24 h) at a relatively low latitude ( $9.7^\circ\text{N}$ ), experienced many

rapid intensification and decay cycles over the course of its lifetime, and made two landfalls along the Gulf coast (Stewart 2005). This study focuses on its development prior to its first and much more intense landfall, which occurred at 0650 UTC 16 September, just west of Gulf Shores, Alabama (AL). Hurricane Ivan presents a unique case for model hindcast as the intensification and decay cycles over the course of its lifetime made it very difficult to forecast (Stewart 2005). The challenge of simulating this GOM hurricane transitioning onto the shelf and making landfall while maintaining an extreme intensity was sought in contrast to the comparatively weak hurricanes studied in previous studies (Warner et al. 2010; Olabarrieta et al. 2012).

A synopsis of Hurricane Ivan is provided by Stewart (2005) and is summarized. Ivan developed from a large, disorganized tropical wave departing the west coast of Africa on 31 August. Despite the lack of organized convection, strong upper-level outflow and a surface pressure system allowed convective bands to begin to develop around a low pressure area on 1 September. The storm that would become Ivan then encountered favorable upper-level outflow and an environment of low shear. Rapid development of this disorganized system followed, with a tropical depression forming around 18 UTC 2 September. This rapid intensification continued and Ivan became a named tropical storm just 12 h later. Rapid intensification continued at a low latitude and Ivan became the southernmost major (3+ Category on the Saffir-Simpson scale) hurricane on record. However, over the next 24 h, Ivan weakened almost as rapidly due to mid-level dry air that was wrapped into the circulation.

Following this weakening period, Ivan again rapidly intensified to Category-3 strength on the Saffir-Simpson scale as the storm passed to south-southwest of Grenada. During this period, the storm featured an extremely small (~15 km in diameter) eye. Passing Grenada, the storm maintained Category-3 intensity until 18 UTC 8 September when the storm rapidly intensified yet again. Ivan attained Category 5 strength on the Saffir-Simpson scale for the first time 12 h later, the first of 3 times the storm reached the highest level on the Saffir-Simpson scale.

As Ivan moved across the Caribbean Sea towards Jamaica, the west-northwestward motion began to decrease to less than  $5 \text{ ms}^{-1}$  on 11 September due to weakening of steering winds and despite the presence of a large subtropical ridge to the north. An eyewall replacement cycle was partly to blame for Ivan's slight weakening during this time. At 18 UTC 11 September, Ivan reintensified rapidly as it translated through an area of low shear, again reaching Category-5 intensity on the Saffir-Simpson scale. Another brief cycle of weakening and reintensification carried Ivan through 13 September. At this point, Ivan's forward speed slowed to  $\sim 4 \text{ ms}^{-1}$  due to a weakened subtropical ridge. Ivan moved into a region of upper-tropospheric outflow, an approaching trough, and extremely warm SSTs strengthening the storm to Category-5 (Saffir-Simpson) intensity for over 30 h. A small eye (~40 km) and low radius of maximum winds (RMW) kept the most intense winds at sea as Ivan passed through the Yucatan strait on 14 September.

After entering the GOM, Ivan's track began to curve northward and there was a steady weakening of the storm due to increasing vertical shear. Weakening continued as Ivan moved northward, encountering shear of  $>15 \text{ ms}^{-1}$  and advection of dry air into Ivan's

core. As the storm moved into a region of cooler waters and underwent several eyewall replacement cycles, it weakened only slightly. Ivan made landfall as a Category-3 hurricane on the Saffir-Simpson scale at 0650 UTC 16 September near Gulf Shores, AL. The strongest winds at landfall were found near the southern AL-western Florida (FL) panhandle due to the eye diameter expanding to ~80 km. After making landfall, Ivan weakened rapidly, losing hurricane strength and becoming a tropical storm around 18 UTC 16 September. Weakening continued as Ivan became a tropical depression on 00 UTC 17 September, and becoming an extratropical low around 18 UTC 18 September.

The center of circulation emerged from the coast and turned back around, crossing FL into the GOM and making a second landfall in southern Louisiana (LA) around 02 UTC 24 September. While the focus of our study is the first and much more intense landfall, this characteristic makes Ivan an exceptionally unique storm. This extremely long-lived storm was characterized with a 22.5 day duration, >10,000 km track, rapid intensification and weakening periods, and experienced an extremely warm ocean condition.

This chapter is organized as follows: Section 2 provides a brief description of COAWST modeling system, the methods used to couple the three independent models together, the fields that are exchanged to each individual model, and the five sensitivity experiments we completed to examine the effect of model coupling with increasing complexity in hindcasting Hurricane Ivan. Results and Analysis are given in Section 3, which demonstrate the improvements in model accuracy through coupling by comparing our five experiments to a combination of *in situ* and remote observations of the atmosphere, ocean, and wave environments. This is followed by a Summary and Conclusions in Section 4.

## *2.2 Methodology*

### *2.2.1 Modeling System*

The COAWST model (Warner et al. 2010) was designed from three state-of-the-art advanced numerical models representing the atmosphere, ocean and wave environments. Representing the atmosphere is the Weather Research and Forecasting (WRF) version 3.2 model using the Advanced Research WRF (ARW) dynamical core (Skamarock et al. 2008). The WRF model is a nonhydrostatic, quasi-compressible atmospheric model with a number of boundary layer schemes, as well as both explicit and parameterized physics. These options allow simulations to be run on different scales ranging from synoptic to mesoscale.

Representing the ocean environment is the Regional Ocean Modeling System (ROMS) version 3.3. ROMS is a free-surface, terrain-following numerical model that is able to solve the three-dimensional Reynolds-averaged Navier-Stokes equations using hydrostatic and Boussinesq approximations (Shchepetkin and McWilliams 2005; Haidvogel et al. 2008). ROMS can be run using multiple advection schemes, turbulence models, lateral boundary conditions, surface and bottom boundary layer schemes.

Representing the wave environment is the Simulating WAVes Nearshore (SWAN) version 40.81 model. The SWAN model is a spectral wave model that solves the spectral density evolution equation (Booij et al. 1999). SWAN is able to simulate wind wave generation and propagation in coastal waters. SWAN also includes many physical processes that can be enabled or disabled including refraction, diffraction, shoaling, and wave-wave interactions. Wave dissipation is available from the physical processes of whitecapping, wave breaking, and bottom friction.

In addition to these numerical models, the Community Sediment Transport Model (CSTM) can be coupled to the ocean model and provide the hydrodynamic model with simulated erosion and deposition across many different types and sizes of sediments (Warner et al. 2010). The CSTM is not used in this study; however, a previous study into the transfer of sediments during TCs has been completed with Hurricane Isabel (2003) as a test case (Warner et al. 2010).

These separate models communicate via the Model Coupling Toolkit (MCT; Larson et al. 2004; Jacob et al. 2005; Warner et al. 2008), which is a fully parallelized system that uses the Message Passing Interface (MPI) to exchange model state variables. First, the master program initializes MPI and distributes each model component onto different sets of processors. Each individual model enrolls into MCT and configures its own domain, dynamics and physics parameters as defined by their respective documentation. Data exchange occurs by MCT at initialization between the models, after which the models integrate by their specified time step to a defined synchronization point. At that instance data are exchanged between the models. Model integration then continues until the next synchronization point where data are exchanged again. This process is repeated through the end of the models' integrations, during which data are output at the individual models' predetermined intervals. At the end of the models' iterations, the master program finalizes the MCT and MPI and terminates the program.

### 2.2.2 Model Coupling

The COAWST modeling system allows exchange of prognostic fields between the various components. Variables that are exchanged in the fully coupled experiment are shown in Fig. 2.1. While the SST is passed from ROMS to WRF, sea surface stresses ( $\tau$ ) and net heat flux are passed from WRF to ROMS. WRF passes winds at 10 m above the sea surface ( $U_{10}$ ) directly to SWAN, which are used in the computation of significant wave height, average wavelength, and relative peak period to be passed back to WRF.

Without wave coupling, surface roughness is computed in WRF based on the Charnock (1955) relation of roughness length to wind stress

$$z_0 = z_{Ch} \frac{u_*^2}{g},$$

where  $z_0$  is the roughness length,  $z_{ch}$  the Charnock parameter (a dimensionless value of 0.018),  $u_*$  the friction velocity (in m/s), and  $g$  the acceleration due to gravity ( $9.81 \text{ m/s}^2$ ).

With the addition of wave coupling, we have a choice of three different parameterizations of sea surface roughness. In our simulations of Hurricane Ivan, the most accurate choice of sea surface roughness was determined by comparison of intensity and wave heights that most closely resembled verification. Based on our comparisons (not shown), we chose to use the Taylor and Yelland (2001) parameterization

$$\frac{z_0}{H_s} = A_1 \left( \frac{H_s}{L_p} \right)^{B_1},$$

where  $H_S$  is the Significant Wave Height (in m) and  $L_p$  the Wave Period (in s).  $A_1$  and  $B_1$  are constants calculated in Taylor and Yelland (2001) to be 1200 and 4.5 (both are dimensionless values), respectively.

Although the use of a simplified drag formulation coefficient based on the Charnock (1955) relationship has been shown to over-estimate drag in high-wind regimes, Moon et al. (2007) demonstrates that there is only a ~10% increase in strength, and minimal effect on intensity through use of a drag limiter. To investigate this further we completed additional coupled experiments (not shown) utilizing modified surface bulk drag coefficients according to Donelan (2004) and enthalpy flux coefficients according to Garratt (1992). Through use of these formulations, our simulations show increased wind speeds but similar intensity and track, in agreement with Moon et al. (2007), Wada et al. (2013), and Wada et al. (2014). In the modified bulk and enthalpy flux experiments, the SST across the domain was similar to our experiments (within 0.5 °C at all *in situ* locations), and the stronger wind field resulted in a ~15% increase in wave heights. These additional experiments demonstrated that the limited drag coefficient approach has an effect and modified enthalpy fluxes in the high-wind regime should be examined in future study of coupled models in TC environments. However, based on our results demonstrating minimal difference, Hurricane Ivan may not be the most appropriate case for these investigations.

As in SWAN-WRF coupling, sea surface wave parameters passed from SWAN to ROMS include significant wave height, average wavelength, and relative peak period. Surface wave direction, bottom wave period, bottom orbital velocity, percentage of breaking waves and dissipation energy are also transferred. Sea Surface Height (SSH) is passed from

ROMS to SWAN, as well as east and north currents computed as a vertical distribution of the current profile based on the method of Kirby and Chen (1989). The authors recognize the importance of wave-current interaction in TC forecasting, and we refer interested readers to recent publications from Olabarrieta et al. (2011, 2012), and Kumar et al. (2012). These papers examine wave-current interaction by using the COAWST model for a number of case studies, in addition to ongoing research by the authors for future publication.

The sea surface momentum and heat fluxes for the ocean model can be computed in one of two ways. The original method utilized a bulk flux formulation of Fairall et al. (1996, 2003) and required from WRF 10-m wind vectors ( $\bar{U}_{10}$ ), air temperature ( $T_{\text{air}}$ ), atmospheric pressure ( $P_{\text{air}}$ ), humidity, downward long wave radiation, and net shortwave radiation. The wave (SWAN) model exchanges variables of significant wave height, average wavelength, and relative peak period to ROMS. From these variables, bulk fluxes of surface stress ( $\tau$ ) and heat flux ( $hf$ ) are computed and used by the ocean model.

However, there are potential problems for use of this configuration in our case. First, their utility in the high wind scenarios is subject to further investigation. Second, the combined use of bulk fluxes and in-model parameterizations could result in inconsistent flux calculations between the models. Therefore, we use a second option, which uses the momentum and buoyancy fluxes computed by WRF to directly drive the ocean model. This ensures a consistent forcing between the two models and does not allow for parameterizations to be made in both WRF and ROMS, which could differ significantly, especially in a hurricane environment.

### 2.2.3 Experimental Design

As described in the introduction, Hurricane Ivan was an extremely intense Saffir-Simpson Category 5 (winds  $\geq 70$  m/s) hurricane when it moved through the Caribbean ocean, weakening slightly to a strong Saffir-Simpson Category 3-4 (wind speeds 50-70 m/s) hurricane as it moved through the GOM in September 2004. We use five different coupling configurations of COAWST to investigate model sensitivity to varying complexity in air-sea-wave interaction and feedback (Table 2.1).

In the first experiment (*Static SST*), the WRF model iterates with an unchanging SST condition based on the Real Time Global (RTG) SST analysis provided by Gemmill et al. (2007) interpolated to the model initialization time. This represents a case of no ocean feedback to the atmospheric model, and hence no SST cooling signature appears in the ocean model during and after Hurricane Ivan's passage through the GOM. In the second experiment (*Dynamic SST*), the WRF model executes with the SST input from daily RTG SST analysis (Gemmill et al. 2007), interpolated every 6 h, from initialization to completion. Unlike the *Static SST* experiment, a cooling signature trailing Hurricane Ivan is present in this simulation. The third experiment (*WRF OML*) utilizes a 1-dimensional ocean mixed layer (OML) model based on Pollard et al. (1972) and integrated into WRF by Davis et al. (2008). In *WRF OML*, the OML has been set to a constant 40 m across the domain with a  $0.14 \text{ }^{\circ}\text{C m}^{-1}$  lapse rate. The fourth experiment (*2-Way*) enables coupling between WRF and ROMS exclusively. The fifth and final experiment (*3-Way*) demonstrates complete coupling within all of the components of the COAWST model as demonstrated in Fig. 2.1.

#### 2.2.4 Domain and Model Configuration

The WRF model domain (encompassing the entire geographic area of Fig. 2.2) is chosen to incorporate the entire ROMS and SWAN model domains. The WRF domain is significantly larger than the collocated ROMS and SWAN domains. This is designed such that additional grid points are available in order to provide Hurricane Ivan sufficient model space in order to develop and strengthen after initialization. The WRF model has a horizontal grid spacing of 8 km in the outer domain. ROMS and SWAN grids are collocated, having a horizontal grid spacing of 5 km. As in Warner et al. (2010), grid points had to be interpolated before model initialization for proper data exchange by the MCT Larson et al. (2004). Interpolation weights were utilized in order for the models to exchange information across their spatial domains. The Spherical Coordinate Remapping Interpolation Package (SCRIP) was used to implement a conservative remapping scheme for this purpose (Jones 1999; Warner et al. 2010). The weights are computed using a nearest neighbor bilinear interpolation and then are read in during initialization for use during the models' iteration.

The best initialization time for our model hindcast was determined based on several *Static SST* runs (not shown). From this ensemble, we chose the model run whose track and intensity most closely represented the National Hurricane Center best track data (hereafter Verification) was selected. The simulation that performed best was initialized at 12 UTC 12 September and terminated at 00 UTC 17 September, for a total run time of 4.5 days (108 h). This simulation had a slight eastward track error, but demonstrated similar translation speed and timing for landfall compared to verification as well as the best comparison to observed intensity. Accurately representing the intensity of strong hurricanes at model initialization

has posed a significant hurdle for TC modeling from the atmospheric perspective (Rogers et al. 2006). With the models initialized from a coarse 1° Global Forecasting System (GFS) model solution, the simulated TC had an intensity of 986 hPa, whereas Verification demonstrates that Hurricane Ivan had an intensity of 919 hPa at the time. As a result, there was a significant intensity deficit at initialization across all model runs

Multiple approaches were investigated to alleviate this initial intensity deficit from Zambon (2009) while maintaining an accurate comparison to the 108 h hindcast track. Initialization was attempted from analysis with finer 32 km grids, such as NARR, or using a bogus (simulated vortex) TC modeled on a combination of NHC best-track and H-Wind data. In either case, the TC structure and track were not well reproduced. We attribute this issue to the problem discussed in Kurihara et al. (1993, 1995), where the bogus vortex was out-of-balance with the large scale forcing. To correct this problem, we adopted the GFDL bogus vortex scheme developed by Kurihara et al. (1993, 1995), which divides the large-scale analysis into environmental flow and vortex circulation. The vortex circulation is then divided into axisymmetric (derived from the axisymmetric perturbation over the prior 12 h) and symmetric components, which are then included in the environmental background flow. Combining the intense and balanced vortex provided by the GFDL product with the large scale environmental forcing provided by the GFS, we obtain a track that was superior to simulations using GFS alone. There was a more profound change to the initial intensity, greatly reducing the initial gap. The GFS-only simulation initialized TC featured intensity 67 hPa weaker than verification, compared to the blended initialization with intensity 8 hPa stronger than verification. After initialization, the simulation is free to develop and is run

without any nudging throughout the 108 h hindcast. The boundary conditions are derived from the GFS solution alone and are updated every 6 h. Completing the hindcast without the added benefit of data assimilation, nudging, etc. was essential to isolating the effects of coupling, one of the primary goals of this study. As a result, the simulations do not provide an exact hindcast of Hurricane Ivan, rather we focus on examining the effect of different complexity of couplings on the hindcast.

To better resolve the TC, the WRF model downscales using a 2-way vortex-following moving nested grid. The co-located ROMS/SWAN grids do not feature a nested grid. Halliwell et al. (2011) studied ocean response from Hurricane Ivan utilizing atmospheric forcing from the Coupled Ocean-Atmosphere Mesoscale Prediction System (COAMPS; Hodur 1997) merged with 10 m vector wind fields (H\*WIND; Powell et al. 1998). This study asserts that decreasing horizontal grid spacing below ~10 km in the ocean model grid results in negligible changes to the ocean model result. The WRF outer grid dimensions were 500 (east-west) by 450 (north-south) with 31 vertical levels and 8 km grid spacing. The inner grid is spaced at 2.6 km (a 1-to-3 grid spacing ratio) measuring 301 (east-west) by 301 (north-south) grid points with 31 vertical levels. This inner-nest was required to resolve the TC structure of the eye and eyewall in the atmospheric model (Hill and Lackmann 2009; Gentry and Lackmann 2009; Gopalakrishnan et al. 2012). In addition, Halliwell et al. (2011) argues that atmospheric forcing that is able to resolve the eye and eyewall of the storm (<10 km horizontal grid resolution in the atmospheric model) is essential in modeling the ocean response. The WRF model time step was defined as 24 s on the outer grid, 8 s on the inner grid. Grid resolved precipitation on both grids was computed using the WRF Single-Moment

6-class microphysics scheme (WSM-6) from Hong and Lim (2006). This first-order microphysics scheme features water vapor, cloud water, cloud ice, rain, snow, and graupel. On the 8 km outer grid, the Kain-Fritsch CP scheme (Kain 2004) was used to parameterize precipitation processes on a sub-grid scale. For the inner grid, the 2.6 km mesh was able to resolve precipitation adequately on a grid scale and no cumulus parameterization was necessary. Longwave and shortwave radiation physics were computed using the Rapid Radiative Transfer Model (RRTM) (Mlawer et al. 1997) and the Dudhia (1989) scheme, respectively, called every 8 minutes on the outer grid and 2 minutes on the inner grid. The Eta surface layer scheme (Janjić 1990; 1996) based on similarity theory (Monin and Obukhov 1954) physics option was used along with the Noah land surface model (Chen and Dudhia 2001) for both grids. The Mellor-Yamada-Janjic turbulent kinetic energy planetary boundary layer (PBL) model (Mellor and Yamada 1982; Janjić 1990; 1996; 2002) was called every time step on both WRF domains.

The ROMS/SWAN domain (bordered by the blue box in Fig. 2.2) was on a rotated rectangular grid with a horizontal grid spacing of 5 km. The ROMS model utilized 36 stretched terrain-following vertical levels with a finer vertical grid near the surface and bottom in order to better resolve the ocean boundary layers (Hyun and He 2010). A 25 s baroclinic time step was used. Open boundaries along the eastern and southern portions of the domain are specified with values from the 1/12°, global HYbrid Coordinate Ocean Model with Naval Research Lab (NRL) Coupled Ocean Data Assimilation (HYCOM/NCODA) solutions, which assimilate satellite SSH and SST as well as *in situ* observations from expendable bathythermographs (XBTs), ship board conductivity-temperature-depth (CTD),

and ARGO floats (Chassignet et al. 2007). The model was initialized using these boundary conditions, constrained by climatological averaging as well as the incorporation of tidal data through a 10-day spin-up before coupling was introduced.

We followed the scheme of Marchesiello et al. (2001), whereby Orlandi-type radiation conditions were used in conjunction with relaxation (with timescale of 0.5 days on inflow and 10 days on outflow) to pass HYCOM/NCODA tracer (salinity and temperature) and 3-d velocity fields to ROMS. For the free surface and depth-averaged velocity boundary conditions, we adopted the method of Flather (1976) with the external values defined by HYCOM/NCODA, updated every day. In our ROMS setup, we used Mellor and Yamada (1982) to compute vertical turbulent mixing, as well as the quadratic drag formulation for the bottom friction specification.

The SWAN model was solved on the same grid as the ROMS model. Boundary conditions were derived from solutions of the global WaveWatch 3 (WW3) model [Available: <http://polar.ncep.noaa.gov/waves/index2.shtml>] and are updated every 3 h. In our SWAN setup, directional space was utilized with 36 directional bins and 24 frequency bins of 1 s width between 1 s and 25 s. Nonlinear quadruplet wave interactions were activated in the model. Wave bottom dissipation was parameterized using the Madsen et al. (1988) formulation, with an equivalent roughness length scale of 0.05 m. The depth-induced breaking constant, e.g., the wave height to water depth ratio for breaking waves, was set to 0.73. Wind-wave growth was generated using the Komen et al. (1984) formulation. A backward-in-space, backward-in-time advection scheme was used for iteration.

## 2.3 Results and Analysis

### 2.3.1 Atmosphere

The simulated storm tracks from each of the 5 experiments, along with verification, are compared in Fig. 2.2. Variations in Hurricane Ivan's track with coupling scheme are relatively minor and consistent with the earlier assertion that track is largely dependent on large-scale atmospheric circulation processes and less influenced by ocean-atmosphere interaction on the time and spatial scales of the models. Position error (Fig. 2.3, top-panel) is computed as the difference between NHC best track locations of the storm center at 12 h intervals and the model location of the minimum sea level pressure. The run that best represented the TC track consistently was the *2-Way* experiment. However the difference between the track error among the experiments is quite small throughout the forecast: within 20 km through the first 60 h, and within 40 km after that.

As far as simulating Hurricane Ivan's intensity (Fig. 2.4), strong differences between modeled TCs begin to show almost immediately after the TC enters the ROMS/SWAN domain (approximately 8 h after initialization). The difference in modeled intensity against verification is shown in Fig. 2.3 (bottom panel), where positive (negative) values denote overintensification (underintensification). While the introduction of the ocean model resulted in underestimation of TC intensification, the magnitude of error of intensity is reduced in both coupled cases compared to the three uncoupled cases. In addition, the root-mean-square error (RMSE) and correlation coefficient ( $r$ ) of TC intensity (Table 2.2) demonstrates that the 2 coupled experiments were more accurate in representing Ivan's intensity than the uncoupled experiments.

As shown in Fig. 2.4, the temporal evolution and trends present in observed intensity are not present in the uncoupled runs. This lack of trend is found even when including ocean feedback through use of a hindcast SST condition (*Dynamic SST*) or integrating a 1-D OML model (*WRF OML*; Pollard et al. 1972; Davis et al. 2008). The coupled models most accurately resolved the trends of TC intensity throughout the run, especially when Ivan experienced rapid weakening as it entered the GOM. Given that the storm evolution was better predicted using a coupled model, the complexity of the ocean condition, specifically the spatial distribution of SST within the GOM, would need to be examined before and after Ivan's passage.

### 2.3.2 SST Analysis

The spatial variation of modeled SST in the GOM is shown in Fig. 2.5 for the WRF-only *Dynamic SST* and *WRF OML* cases, the COAWST *2-Way* and *3-Way* coupled experiments, and the Geostationary Operational Environment Satellites (GOES) SST data. The GOES SST data were obtained from the JPL Physical Oceanography Distributed Active Archive Center (PODAAC). The *Static SST* case is intentionally left out, as it is represented by the pre-storm condition of the *Dynamic SST* case throughout the model run.

Due to cloud cover associated with hurricane, GOES SST data were obscured over a large swath of the West Florida Shelf immediately before model initialization time. In order to provide an initial analysis, GOES SST was averaged over three days before model initialization (12 UTC 9 September through 12 UTC 12 September), hereafter referred to as the Pre-Storm SST. Likewise, cloud cover required averaging of the daily GOES SST

observations from 00 UTC 17 September through 00 UTC 18 September (hereafter Post-Storm SST). To be consistent, a similar averaging procedure was done for model simulated SST fields for comparison.

As previously mentioned, a number of factors result in fluctuations of hurricane intensity. These include but are not limited to SST below the storm, eyewall replacement cycles, wind shear, formation of a stable boundary layer in the SST cold wake, and synoptic-scale atmospheric forcing (Fowle and Roebber 2003; Done et al. 2004; Wang and Wu 2004; Rogers et al. 2006; Chen et al. 2007; Davis et al. 2008; Lee and Chen 2012; 2014). For the purposes of our experiments, the only difference between the simulations is the variation in ocean SST and sea surface roughness to the atmospheric model. Therefore, everything else being equal, the atmospheric model resolves TCs with vastly different intensities based on differences in SST and sea surface roughness. We examine these different intensities using the SST as the mechanism driving the differences and we offer a chronological explanation of the intensity variation using SST as the primary indicator of storm intensity for our experiments.

At model initialization, 12 UTC 12 September, the location of Ivan in a region of 30 °C SST south of Cuba helped the storm to intensify to 919 hPa. From this point until F36 (00 UTC 14 September) relatively constant temperatures along the storm track resulted in minimal changes to Ivan's intensity. As Ivan crossed the Yucatan Strait and into the GOM, cool SSTs are coincident with a sharp reduction of intensity. This signal is apparent in observations, from F36 through F48 (Fig. 2.4). From F48 through F60, there is some very slight intensification, as Ivan is passing a region where Pre-Storm SSTs are shown to be

above 29 °C. The crossing of Ivan over cold water on 15 September corresponds to the 13 hPa weakening from F60 to F72. Just prior to landfall, Ivan passed over warmer water on 16 September, concurrent with an observed 10 hPa intensification from F72-F84 (Fig. 2.4), followed by rapid weakening with landfall.

None of the uncoupled runs (*Static SST*, *Dynamic SST*, and *WRF OML*) in Fig. 2.4 reflect any of these fluctuations with spatial variation of SST. The coupled model runs do accurately demonstrate this weakening, with a distinct decrease in intensity at F36-F72 in the *2-Way* and *3-Way* coupled cases. This diminished intensity coincides with the TC cooling the waters in the GOM as resolved by ROMS. In the uncoupled cases, significant decreases in intensity are absent until landfall. Even with the inclusion of a 1-dimensional OML model, the *WRF OML* case demonstrated increasing intensity from F36 until landfall, against the trend shown in observations. As a result, the coupling of a fully 3-dimensional ocean model to WRF is necessary to correctly resolve the source of energy on which TCs intensify or weaken.

Of concern in the coupled model cases is the comparison of the modeled Pre-Storm SST to the GOES SST, which shows a 0.5-1.5 °C warm bias in the model (Fig 2.5). In Fig. 2.6, *in situ* buoy data at 5 locations are used to compare the coupled (*2-Way* and *3-Way*) SST, satellite derived SST, and *in situ* SST. At each of the five locations along Ivan's track in the GOM, the *in situ* data show the satellite SST data tend toward a cold-bias in the Pre-Storm environment. As a result, while the satellite-derived SSTs of the Pre-Storm environment in Fig. 2.6 are colder than model results, the *in situ* measurements indicate this discrepancy may be a result of GOES SST cold-bias.

When comparing the change in SST during Ivan's passage, the spatial distribution of SST change ( $\Delta$ SST) demonstrated in Fig. 2.5 is similar between the coupled models, GOES SST, as well as previous studies (Walker et al. 2005; Prasad and Hogan 2007). The uncoupled experiments, including the *WRF OML* case, do not demonstrate ocean eddies and other complex circulation structures that can only be resolved with a coupled model (Halliwell et al. 2011; Jaimes et al. 2011). Both coupled models demonstrate larger magnitude and breadth of deep-ocean cooling along the right-side of the track when compared to the satellite derived  $\Delta$ SST. Buoy time series (Fig. 2.6), which shows that model-derived SSTs on the right side of the track (e.g. Station 42003) are cooler than the *in situ* measurements, also indicating an overestimate in cooling in the model on this side of the storm track. Station 42039, also located on the right side of the storm track, demonstrates a model cold bias on the continental shelf, although much less severe. This greater cooling of SSTs partly explains the underintensification of the TC in the coupled cases (in agreement with Lee and Chen (2012), and it is more significant in the *3-Way* coupled case, compared to the *2-Way* coupled case. This effect is also demonstrated in Wada et al. (2010) and is largely due to the enhanced mixing of the ocean provided by effects introduced by wave modeling.

The spatial extent of the SST cooling demonstrates that the right-side cooling bias is enhanced in the *3-Way* coupled simulation when compared to the *2-Way* simulation (Fig. 2.5). This difference is confirmed in the *in situ* time series (Fig. 2.6). To investigate this, we examined the surface stress (not shown) as the intensity, strength, and surface roughness formulation of the experiments differ. For the *3-Way* experiment, the surface stress was higher (lower) on the right (left) side of the TC track. The SST was lower (higher) on the

right (left) side of the track, partly owing to this difference in surface stress. For this study, this was a minor effect as the difference in SST cooling was within 0.25 °C in all *in situ* time series comparisons and was within 1 °C throughout the domain. While negligible for our case, further examination of the inclusion of wave effects on SST in this complex ocean-atmosphere-wave coupled environment is subject to further study.

### 2.3.3 Mixed Layer Prognostic Variable Analysis

In order to investigate the SST difference between stations on the continental shelf and in the deep-ocean, we conduct a time series analysis similar to Prasad and Hogan (2007) of the sea surface stress ( $\tau$ ) and heat flux, mixed layer (ML) temperature, and 3-dimensional currents were examined at two locations along with the modeled track (S1 and S2 shown in Fig. 2.2). S1 was chosen to represent a point on the continental shelf, and S2 was selected to represent the temperature and heat budget of the deep ocean. As the *2-Way* and *3-Way* SST results are similar (Figs. 2.5 and 2.6), only analysis for the *2-Way* case is provided to simplify the analysis to specifically demonstrate the impacts of ocean dynamics, without the inclusion of wave effects.

Analysis at point S1 (Fig. 2.7) demonstrates the response of the OML on the continental shelf to Ivan's passage. Surface wind stress ( $\tau$ ) gradually builds up, peaks, changes direction, and rapidly falls off as Ivan moved over the location. The net heat flux (positive indicating flux into the ocean) is dominated by short wave solar radiation demonstrating a clear diurnal cycle throughout the model run. When Ivan tracked through this location on 16 September, the ocean released heat to the TC (atmosphere). This, along

with limited the solar radiation due to cloud cover, produced a negative net heat flux. The stronger surface wind stress enhanced mixing, resulting in a cooler surface temperature and eroded thermocline. Positive U represents eastward motion, positive V represents northward motion, and positive W represents motion towards the ocean bottom. The U and V currents clearly demonstrate an inertial oscillation after the TC's passage with a period of approximately 1 day.

At the offshore point S2 (Fig. 2.8), the temperature distribution with depth is very different than for S1. The thicker ML prevents complete erosion, and the thermocline remains established well below the surface. While temperatures near the surface drop significantly as Ivan passes (also demonstrated in Figs. 2.5 and 2.6), they remain well above the 26 °C critical value for TC development (Leipper and Volgenau 1972). As at point S1, a strong negative heat flux exists during the storm passage and the ocean velocity fields (U, V, and W) demonstrate an inertial oscillation after the TC passes.

#### 2.3.4 Mixed Layer Heat Budget Analysis

The ML heat budget can be diagnosed by piecing out the relative contribution of each term in the heat budget equation

$$\frac{\partial T}{\partial t} = -u \frac{\partial T}{\partial x} - v \frac{\partial T}{\partial y} - w \frac{\partial T}{\partial z} + \frac{\partial}{\partial z} \left( k \frac{\partial T}{\partial z} \right)$$

where  $-u \frac{\partial T}{\partial x} - v \frac{\partial T}{\partial y}$  is the horizontal advection,  $-w \frac{\partial T}{\partial z}$  is the vertical advection,

$-u \frac{\partial T}{\partial x} - v \frac{\partial T}{\partial y} - w \frac{\partial T}{\partial z}$  represents total advection,  $\frac{\partial}{\partial z} \left( k \frac{\partial T}{\partial z} \right)$  is vertical diffusion, and  $\frac{\partial T}{\partial t}$  the

local rate of change in temperature measured in °C/day. We neglected horizontal diffusion terms because they are orders of magnitude smaller. These terms are calculated as diagnostic variables, derived directly from output of the ocean model.

At the onshore point S1, before the storm's passage, the weak diurnal oscillations in U, V, and W are found in both the horizontal and vertical advection terms of Fig. 2.9. In the Pre-Storm environment (12 UTC 12 September through 00 UTC 15 September), the horizontal advection terms and vertical advection terms oscillate but are out of phase and therefore cancel each other out (shown in the total advection term). Immediately prior to the eyewall passage (00 UTC 15 September through 15 UTC), cooling due to upwelling is negated by horizontal advection at the surface. Below 30 m, there is a warming trend due to horizontal advection, which creates a positive total advection term in this part of the ML. As the TC passes through, there is strong cooling due to horizontal advection through the entire water column that is negated in the upper 40 m by downwelling. Afterwards, the wind stress is reduced with TC passage, although horizontal advection begins to warm the entire water column, the upper 60 m is negated by cooling from vertical advection.

The contribution of the vertical diffusion term to the heat budget is small until the arrival of strong surface wind stresses (00 UTC 15 September to 15UTC). The temperature diffusion is strongly negative at the surface and positive below 40 m. Throughout the storm event, the total heat flux becomes very negative at the surface due to losses to the atmosphere. As a result of the combination of these factors, just before the eyewall passes, the ML is deepened and the surface temperature is reduced.

As the eyewall passes and the wind shifts (15 UTC 15 September through 00 UTC 16 September), horizontal and vertical advection near the surface are both extremely strong but, as in the pre-storm period, opposite in phase, cancelling each other out above 20 m. There is also strong heat loss to the atmosphere through diffusive fluxes near the surface. Below 20 m, intense upwelling causes the advection term to be strongly negative. As a result, there is great heat loss throughout the entire water column as the TC passes, cooling the ML and eroding the thermocline. The contributions of heat loss during this period are approximately evenly split between advection and diffusion. As the storm winds subside (00 UTC 16 September), there is an inertial oscillation of U, V and W causing the ML to be alternately cooled and warmed with a period of approximately 1 day. Time series (Fig. 2.9, bottom panel) of each heat budget term averaged over the mixed layer depth (MLD, roughly upper

100 m)  $\frac{\int_{MLD} f(z) dz}{MLD}$  show that contributions from ocean entrainment and diffusion are

equally responsible for the cooling trend of the continental shelf ocean during the passage of the storm.

At the deep ocean point, S2 (Fig. 2.10), ocean advection plays a larger role than diffusion in changing the thermodynamic profile of the ML throughout the storm event. Prior to Ivan's passage, the horizontal and vertical advection terms are roughly equivalent in the upper 20 m of the profile. However, as Ivan treks to this point, there is significant transport of warm water below the surface. This is a signature of Ivan pushing warm water northward to this location, an effect similar to what has been shown in Oey et al. (2006) with Hurricane Wilma introducing warm water to the loop current.

There is a strong upwelling signature before the passage of the TC eye (around 12 UTC 14 September). This upwelling is weakly relaxed by horizontal advection in the upper 50 m but strongly negated in the lower 50 m. Cooling by vertical advection in the upper 50 m, along with warming by horizontal advection in the lower 50 m, cause the ML to initially deepen before the wind shift at 21 UTC 14 September. After the wind shift, the contributions of vertical and horizontal advection reverse and there is brief warming near the surface and cooling below. The thermocline is then almost completely eroded through to the surface. As with the nearshore point, after the winds diminish, there is an inertial oscillation of U, V and W with a period of approximately 1 day causing the ML to fluctuate between warming and cooling.

Diffusion plays a much less significant role at this offshore location, demonstrating only a modest contribution from negative diffusion at the surface and warming below as the eyewall passes at 21 UTC 14 September. In contrast to the shallow water point, the vertically averaged heat transfer time series demonstrates that entrainment of cooler water accounts for a much larger proportion of heat transfer in the deep ocean, which is consistent with Price (1981).

### *2.3.5 Wave Analysis*

To examine the results from the wave model, we compared significant wave heights available from the National Data Buoy Center (NDBC) during this storm event. The same five buoys from the earlier SST comparison were used for spatial and temporal comparison

of the waves produced with the *3-Way* experiment. The results, shown in Fig. 2.11, demonstrate overall good agreement with *in situ* observations.

Despite the eastward deviation in track, modeled results at most of the offshore buoys compared well with observations as demonstrated by the RMSE and correlation coefficients. The worst performing comparison, at buoy 42007, is in close proximity to the shoreline (having a model-resolved depth of 12 m). The comparison suffers due to complicated shorelines and bathymetry, which are not well resolved by the 5 km horizontal grid spacing of the model. On the continental shelf, we examine results from buoys 42040 and 42039. At 42039, the solution suffered somewhat as the wave heights reduced more rapidly with Ivan's passage in the model than in the observations. This resulted in the model underestimating the waves after the peak at approximately F085, which increased the RMSE. At 42040, the temporal comparison is very good, with both the model and observations demonstrating increasing wave heights at approximately the same time. With the eastward deviation in track, the model did not resolve the peak of significant wave heights to the extreme level that was observed. The greater than 15 m waves were so intense that they tore the buoy from its mooring (Teague et al. 2007), and wave heights were no longer reported after 00 UTC 16 September.

Off the shelf, two buoys 42001 and 42003 were considered. They are roughly equidistant from the observed and modeled track in the GOM. At 42001, off to the west of the storm track, the peak of the simulated waves is delayed compared to the observations. In addition, the eastward deviation of the modeled TC causes the significant wave height of the simulated waves to be slightly less than observed. At 42003, the eastward deviation in

modeled track cause the waves to build up more quickly than observed. However, the peak magnitude of the simulated waves is very close to what was observed. A RMSE of 0.93 and correlation coefficient of 0.97 is demonstrated at this location.

The results of the fully-coupled 3-*Way* coupled system are shown in Fig. 2.12. The simulation predicted landfall almost exactly in agreement with the verified 0650 UTC 16 September. Immediately prior to the intense TC making landfall, strong winds and shown driving strong currents which result in enhanced upper-ocean mixing. This, along with sensible and latent heat fluxes to the storm, lowers the SST, particularly on the right side of the track. Large waves are also generated which impact the shoreline before, during, and after landfall.

#### *2.4 Summary and Conclusions*

Large-scale, global models representing the atmosphere have gradually improved track prediction of TCs over the last several years (Goerss 2006). However, prediction of TC intensity still leaves much to be desired, leading to errors in surface forcing for ocean and wave models. Deficiencies in TC prediction are attributed to, among other causes, lack of coupling to an ocean model (Chen et al. 2007). The newly developed Coupled Ocean-Atmosphere-Wave-Sediment Transport (COAWST) model couples three state-of-the-art numerical models: WRF (atmosphere), ROMS (ocean), and SWAN (wave). The methods of model coupling, physical parameterizations, and development of initial and boundary conditions for each of the three individual numerical models were discussed.

We applied COAWST model to hindcast Hurricane Ivan (2004), Several model sensitivity experiments were conducted to examine effects of different levels of coupling among atmosphere, ocean, and wave environments. Model cases with coupling between the atmosphere, ocean, and waves demonstrate modest improvement in track but significant improvement in intensity when compared to the uncoupled cases.

For the coupled cases, ocean and wave model output were compared to *in situ* and remote observations. It shows that the coupled models represent the SST well, to within 1 °C, at 4 of the 5 *in situ* buoy stations. However, for the interior of the GOM on the right side of the track, both the remote and one *in situ* time series of observations (at buoy 42003) demonstrate a significant model cold bias. This cold bias is likely due to the excessive mixing produced by the ocean model, a topic we will investigate and report in future research. Analyses of the heat budget illustrating the modeled effects of a strong TC interacting with the ocean are consistent with observed and theorized ocean dynamics in a hurricane environment. Likewise, coupled wave model results compare favorably to significant wave height measurement by buoys.

With the addition of wave coupling in the *3-Way* case, treatment of the surface roughness length had a definite effect on the maximum wind speed derived in the simulations, and is an area needing more study and refinement. Here we chose to use the Taylor and Yelland (2001) scheme to calculate surface roughness length based on the significant wave height and wave period. The COAWST system provides two other parameterizations for surface roughness: that in Oost et al. (2002) and in Drennan et al. (2005). None of these sea surface roughness parameterizations are universally “best”, and the

choice should be made for each specific case. For instance, in an examination of Hurricane Ida and Nor'easter Ida using the COAWST modeling system, Olabarrieta et al. (2012) found that the Oost et al. (2002) sea surface parameterization provided the best solution for that particular storm. Future study examining observations and model sensitivity of different wave coupling schemes in generating the roughness length  $Z_0$  and mixing induced by waves is clearly needed.

It is also important to note that future study of the fully-coupled COAWST modeling system should include increased wave-atmosphere fluxes of latent and sensible heating caused by dissipative heating and sea spray. Bao et al. (2011) demonstrated that sea spray has a significant impact as 10-m winds climb above 30 m/s by increasing the enthalpy exchange coefficient ( $C_k$ ) and reducing the 10 m neutral drag coefficient ( $C_D$ ).

While a slight deviation of simulated TC track and intensity cause some difference in the comparisons to observations, the ability of the fully-coupled model to resolve the atmosphere, ocean, and wave environments was shown. The use of a fully-coupled model allows a detailed examination of simultaneous interactions among ocean, atmosphere, and wave environments. In a forecast situation, this model would provide very useful and comprehensive environmental conditions (of atmosphere, wave, and ocean) to agencies and emergency managers in the event of a landfalling hurricane.

Our results show a fairly accurate 108 h simulation of the atmosphere, ocean, and wave environments can be archived without the added benefit of data assimilation, ensemble forecasting, downscaling, or other computationally expensive methods that could degrade the investigation of the dynamics within a coupled model. Future studies including these

techniques may further improve the overall skill of model predictions. Contributions to the TC environment from the effects of improved drag formulations, dissipative heating and sea spray are possible with inclusion of feedback from the wave model, but are left for future study.

### **3 Investigation of the Effect of Coupling on the Extratropical Transition of Superstorm Sandy (2012)**

#### *3.1 Introduction*

As demonstrated in the previous chapters through introduction and with Hurricane Ivan, TCs represent large, discrete events that have dramatic effects on the marine environment. In addition to TCs, storms undergoing extratropical transition and extratropical cyclones (ETCs) also can have devastating impacts to populated coastlines. These impacts are not only dependent upon strength (represented by maximum 10 m wind) and intensity (represented by minimum sea level pressure) of the storm, but also storm size (Merrill 1984; Hill and Lackmann 2009). As considerably more people and property have aggregated to the shoreline in recent decades, the damage caused by these intense storms will continue to increase (Emanuel 2005). The work contained in this chapter has been accepted for publication in Zambon et al. (in press).

On 22-31 October 2012, the U.S. east coast was under the direct impact of a massive ETC. Record storm surges were observed in highly populated areas of New Jersey (NJ), New York (NY), and Connecticut (CT). Combining devastating flooding with hurricane-force winds, the massive hurricane and extratropical storm that became known as Superstorm Sandy was the second-costliest cyclone on record to impact the United States (U.S.), behind Hurricane Katrina (2005; Blake et al. 2013). Sandy made landfall in NJ, approximately two hours after becoming an extratropical system. The distinction between tropical and extratropical storm proved to be extremely important for claims made to insurance

companies. Thousands of families found their insured homes not covered as they were victims of a “flood” and not a “hurricane” (Smith 2012).

Sandy has a complex synoptic history, which is summarized from Blake et al. (2013). The origins of Sandy begin with a tropical wave, which left the west coast of Africa on 11 October. The broad area of thunderstorms encountered strong shear from 12-13 October inhibiting development. Following in the wake of Hurricane Rafael in the tropical Atlantic, this band of thunderstorms likely encountered upper-level convergence, further inhibiting development through 17 October. On 18 October, the tropical wave entered the eastern Caribbean Sea with increasing disorganized convection on 19 October in an environment of moderate westerly shear.

Through the central Caribbean Sea, the environment was rapidly improving for development (Blake et al. 2013; Galarneau et al. 2013; Shen et al. 2013; Munsell and Zhang 2014). Some rainbands began to appear on 20 October as deep convection increased and pressures began to fall. A broad low-pressure area formed south of Haiti and moved to the west on 21 October with a strong high pressure system established over the Gulf of Mexico (GOM) and southwestern Atlantic. Shear continued to reduce as the low pressure area moved towards an upper-level anticyclone that was building over the southwestern Caribbean Sea. The circulation continued to close and convection intensified as the storm became a tropical depression in the southwestern Caribbean Sea at 12 UTC 21 October, then became a tropical storm just 6 h later.

After becoming a tropical storm, further development was slow, the storm strength increasing another  $5 \text{ ms}^{-1}$  over the next 24 h. A nearby middle- to upper-level trough

accelerated Sandy to the north-northeast as the storm strengthened to a hurricane at 12 UTC 24 October and formed a visible eye. The center of Hurricane Sandy made landfall with  $35\text{ms}^{-1}$  winds between Kingston and South Haven, Jamaica at 19 UTC and continued to intensify after encountering the warm waters to the south of Cuba. Hurricane Sandy continued to strengthen with winds exceeding  $50\text{ms}^{-1}$ , becoming a late-season major hurricane (Category 3+ on the Saffir-Simpson scale).

Sandy made landfall in Cuba at 0525 UTC 25 October and crossed eastern Cuba over 5 h before entering the Atlantic Ocean south of the Bahamas. Weakening occurred during its initial transit through the Atlantic, due to its impact on Cuba and southwesterly shear. Gradually weakening, slowing, and spreading out, Hurricane Sandy moved through the Bahamas on 26 October while losing hurricane strength but doubling the average radii of tropical storm force winds since making landfall in Cuba. This change in structure is attributed to interaction with an upper-level trough, warm advection aloft, increasing upper-level divergence, and movement into a modified continental airmass.

Tropical Storm Sandy's interaction with a mid-tropospheric trough over the central U.S. caused it to accelerate northward while regaining hurricane strength. As a hurricane, Sandy featured some unusual characteristics including a large ( $>150\text{km}$ ) radius of maximum winds and the strongest winds were located to the western (left) side of the track. In addition, frontal structures began to form closer to the center of circulation, enhancing convection, particularly on the left side of the track. Passing offshore of North Carolina (NC) on 28 October, the storm regained tropical structure with the dissolution of frontal structures and the brief appearance of an eye. On 29 October, a blocking pattern over the

North Atlantic caused Sandy's track to bend northward with the trough over the central U.S. moving into the southeast. This trough resulted in reduced shear and provided baroclinic forcing for Sandy which, aided by warm waters from the Gulf Stream, re-intensified the storm. At 12 UTC 29 October, Sandy reached a secondary peak intensity of  $>40 \text{ ms}^{-1}$  while just 400 km southeast of Atlantic City, NJ. Six hours later, the storm reached its lowest central pressure of 940 hPa.

The trough over the southeastern U.S. accelerated Sandy towards the northwest, bending the track towards NJ with an average forward speed of  $10 \text{ ms}^{-1}$ . Sandy's tropical characteristics began to disappear as the storm moved into cooler water north of the Gulf Stream, as well as a cold continental air mass. The National Hurricane Center (NHC) determined the hurricane to have become extratropical at 21 UTC 29 October with the storm just 80 km offshore of Atlantic City, NJ and still rapidly heading towards land. Landfall occurred 1.5 h after the storm was defined as extratropical, near Brigantine, NJ. Post-tropical storm Sandy made landfall with  $35 \text{ ms}^{-1}$  winds and a minimum central pressure of 945 hPa. This pressure was noted by several agencies as the lowest pressure ever recorded in the U.S. north of NC. After landfall, Sandy moved through southern NJ, Delaware (DE), and Pennsylvania (PA). Its track became ill-defined after 12 UTC 31 October and the remnants of the storm moved northwestward over Ontario, Canada.

The landfall into southern NJ was devastating to the northeastern U.S. Peak wind gusts were recorded near  $40 \text{ ms}^{-1}$  with hurricane-force wind gusts reported in 7 states. Record storm tides, the combination of storm surge and astronomical tide, were measured by National Ocean Service (NOS) tidal gauges in the New York City, NY area. Water level

records going back to 1920 at the Battery (in New York City, NY) show a Mean Lower Low Water (MLLW) storm tide of 4.29 m, 1.32 m higher than the previous record set in December 1992. This storm tide was 1.38 m higher than reported during Hurricane Irene's impact a year earlier.

Sandy is characterized as an erosive event, in contrast to Hurricane Irene (2011). Rising storm surge and large waves from the Atlantic Ocean met rising water from back bays in NJ, such as Barnegat Bay and Little Egg Harbor. Barrier islands were almost completely inundated in some areas, breached in others. This resulted in the most catastrophic damage ever recorded in NJ. Flooding from storm surge was recorded as far north as Albany, NY. Rainfall was extensive to the southern (left) side of the track, with 120-180 mm of rain reported in eastern Maryland (MD), Virginia (VA), southern DE. The most rain reported was 326 mm of rain in Bellevue, MD.

In the aftermath of the storm, Sandy became the second costliest cyclone to impact the U.S. with over \$50 billion in damage. 147 deaths were attributed directly to the storm. 72 deaths were reported in the mid-Atlantic and northeastern U.S., the most since Hurricane Agnes in 1972. 650,000 homes were either damaged or destroyed by the storm, mostly as a result of storm surge and/or waves.

The timing of the loss of tropical characteristics of Sandy is highly debatable. At the earliest, NHC forecasts issued at 03 UTC 27 October described Sandy as having characteristics of hybrid cyclone, with the appearance of an occluded low but with a deep warm core and no significant surface temperature gradient (Beven 2012). Galarneau et al. (2013) performs an investigation into the extratropical transition of this storm, which begins

at 00 UTC 29 October as Sandy interacted with a polar trough, and completed near 21 UTC 29 October.

As with Ivan, this chapter utilizes the Coupled Ocean-Atmosphere-Wave-Sediment Transport (COAWST) modeling system (Warner et al. 2010) to simulate Sandy and its impact on the ocean and wave environments as it made landfall in the northeast U.S. The COAWST modeling system has been utilized in the past to examine intense hurricanes (Warner et al. 2010), strong Nor'easters (Olabarrieta et al. 2012), and winter cyclones (Nelson and He 2012). The purpose of this case study is to utilize the COAWST model to examine the effects the atmosphere, ocean, and wave environments had on Sandy as it completed tropical to extratropical transition.

## *3.2 Methodology*

### *3.2.1 Model Configuration*

COAWST couples three state-of-the-art numerical models representing the ocean, atmosphere, and wave environments. For this case study, the models are the Regional Ocean Modeling System (ROMS) version 3.3 (Shchepetkin and McWilliams 2005; Haidvogel et al. 2008), the Weather Research and Forecasting (WRF) model version 3.4 (Skamarock et al. 2008), and the Simulating Waves Nearshore (SWAN) model version 40.81 (Booij et al. 1999), respectively.

For the WRF model, we utilized a TC-following nested atmospheric grid to resolve the inner eyewall processes of Sandy (Hill and Lackmann 2009; Gentry and Lackmann 2009; Gopalakrishnan et al. 2012). The outer grid encompassed the entire U.S. east coast with a

grid spacing of 9 km, while the inner grid was scaled down to 3 km. The WRF model time step was defined as 24 s on the outer grid and 8 s on the inner grid. Grid-resolved precipitation on both grids was computed using the WRF Single-Moment 6-class microphysics scheme (WSM-6) from Hong and Lim (2006). This first-order microphysics scheme features water vapor, cloud water, cloud ice, rain, snow, and graupel. On the 9 km outer grid, the Kain-Fritsch CP scheme (Kain 2004) was used to parameterize precipitation processes on a sub-grid scale. Examination of the dependence on cumulus parameterization on this storm was examined in Bassill (2014) demonstrating vast differences in forecast track due to use of different cumulus parameterizations. An excellent simulation with 4 days of lead time utilizing the Tiedtke (1989) scheme was very recently published in Lackmann (2014). For the inner grid, the 3 km mesh was able to resolve precipitation adequately and no cumulus parameterization was necessary. Longwave and shortwave radiation physics were computed using the Rapid Radiative Transfer Model (Mlawer et al. 1997) and the Dudhia (1989) scheme, respectively. The Eta surface layer scheme (Janjić 1990; 1996; 2002) based on similarity theory (Monin and Obukhov 1954) physics option was used along with the Noah land surface model (Chen and Dudhia 2001) for both grids. The Mellor-Yamada-Janjić turbulent kinetic energy planetary boundary layer model (Mellor and Yamada 1982; Janjić 1990; 1996; 2002) was called every time step on both WRF domains. The initial and boundary conditions for the WRF model are derived from the 1° NCEP FNL Operational Model Global Tropospheric Analyses (National Centers for Environmental Prediction, National Weather Service, NOAA, U.S. Department of Commerce 2000). The product was

used to initialize WRF approximately 35 h before landfall (12 UTC 28 October) with boundary conditions updated every 6 h.

The ROMS/SWAN domain is spatially collocated with the WRF outer domain, with the exception of small lateral boundaries placed on all sides to ensure WRF forcing exists for the entire ROMS/SWAN domain. This domain features grid spacing of 7 to 10 km, small enough to resolve atmospheric forcing from tropical cyclones (Halliwell et al. 2011). The ROMS domain has 36 stretched, terrain-following vertical coordinates, with finer grid spacing used closer to the ocean surface. A 25 s baroclinic time step was used. We followed the scheme of Marchesiello et al. (2001), whereby Orlandi-type radiation conditions were used in conjunction with relaxation (with timescale of 0.5 days on inflow and 10 days on outflow) to downscale daily tracer (salinity and temperature) and 3D velocity fields of global HYCOM/NCODA (HYbrid Coordinate Ocean Model with Naval Research Lab (NRL) Coupled Ocean Data Assimilation HYCOM/NCODA; Chassignet et al. 2007) solutions, which also provided the initial ocean conditions. For the free surface and depth-averaged velocity boundary conditions, we adopted the method of Flather (1976) with the external values also defined by daily HYCOM/NCODA. Our ROMS setup used the Mellor and Yamada (1982) method to compute vertical turbulent mixing, as well as the quadratic drag formulation for the bottom friction specification.

In the SWAN setup, we use the same spatial grid as the ROMS model where directional space was utilized with 36 directional bins and 24 frequency bins between 1 s and 25 s. Nonlinear quadruplet wave interactions were activated in the model. Wave bottom dissipation was parameterized using the Madsen et al. (1988) formulation, with an equivalent

roughness length scale of 0.05 m. The depth-induced breaking constant, i.e., the wave height to water depth ratio for breaking waves, was set to 0.73. Wind-wave growth was generated using the Komen et al. (1984) formulation. A backward-in-space, backward-in-time advection scheme was used for iteration. SWAN was initialized in stationary mode with surface forcing provided by WRF. Boundary conditions were updated every 3 h from solutions of the global WaveWatch 3 (WW3) model (<http://polar.ncep.noaa.gov/waves/index2.shtml>).

As a result of wave coupling, the treatment of the surface roughness length had a definite effect on the maximum wind speed derived in the simulations, and is clearly an area needing more research and refinement. Here we chose to use the Taylor and Yelland (2001) parameterization to calculate surface roughness length

$$\frac{z_0}{H_s} = A_1 \left( \frac{H_s}{L_p} \right)^{B_1},$$

where  $H_s$  is the significant wave height (in m) and  $L_p$  the wave length (in m).  $A_1$  and  $B_1$  are constants calculated in Taylor and Yelland (2001) to be 1200 and 4.5 (both are dimensionless values), respectively. The COAWST system provides two other parameterizations for surface roughness: that in Oost et al. (2002) and in Drennan et al. (2005). Our sensitivity experiments show that the Taylor and Yelland (2001) parameterization provided the best simulation overall among the three, based on comparisons to NHC track, intensity, strength, and *in situ* buoy comparisons of SST and wave heights (not shown).

Our COAWST hindcast for Sandy initialized at 12 UTC 28 October, and ran through 00 UTC 3 November for a simulation time of 132 h. This longer simulation time was

intended to simulate the relaxation period after storm passage, and for *in situ* data comparisons.

### 3.2.2 Experiment Design

Four experiments were performed, with increasing complexity, to explore the ocean-wave-atmosphere dynamics during Sandy. These experiments are shown in Table 3.1. The first experiment (*WRF-Static*) utilized a WRF-only simulation with a sea surface temperature (SST) condition that was unchanged after initialization. The second experiment (*WRF-OML*) featured a one-dimensional ocean mixed layer model from Pollard et al. (1972) and integrated into WRF by Davis et al. (2008). For the *WRF-OML* experiments, utilizing a  $-0.14$   $^{\circ}\text{C m}^{-1}$  lapse rate and a 50 m mixed layer throughout the entire ocean domain. The third experiment (*2-Way*) featured coupling between the WRF and ROMS models, such that the SST was passed from ROMS to WRF and sea surface stresses ( $\tau$ ) and net heat flux were passed from WRF to ROMS. The fourth experiment (*3-Way*) included full coupling (Fig. 3.1) between the WRF, ROMS, and SWAN models. This allows WRF to pass winds at 10 m above the sea surface directly to SWAN, which used them in the computation of significant wave height, average wavelength, and relative peak period; these were then passed back to WRF and ROMS. Surface wave direction, bottom wave period, bottom orbital velocity, percentage of breaking waves, and dissipation energy also were transferred from SWAN to ROMS. Sea Surface Height (SSH) and east and north currents computed as a vertical distribution of the current profile based on the method of Kirby and Chen (1989), were passed from ROMS to SWAN.

### 3.3 Results and Discussion

#### 3.3.1 Atmosphere

The fully-coupled *3-Way* case at time of landfall is demonstrated in Fig. 3.2. Simulated landfall in the Sandy case was determined to be roughly 1.5 h before observed, at 22 UTC 29 October. Visible is an extremely intense storm with winds  $\sim 30 \text{ ms}^{-1}$  and a minimum central pressure of  $\sim 945 \text{ hPa}$ . The track of the storm through the Gulf Stream and into the cooler waters of the Mid-Atlantic Bight (MAB) are well-resolved. The extremely strong waves impacting the northeastern U.S. are also visible.

A comparison of numerical simulations of Sandy's track to the National Hurricane Center's (NHC) best track (Verification; Blake et al. 2013) shows that all experiment results are similar to Verification through landfall (Fig. 3.3). Sandy maintained a similar track in all simulations before its landfall. Twelve hours after landfall, the simulated tracks began to diverge from verification. This is in part a consequence of the tracking algorithm, which follows the location of lowest central pressure whereas the best-track locates the center of storm. As Sandy moved inland, the storm became disorganized and the center of circulation was not consistent with the location of lowest central pressure. While this is similar to the NHC Best Track analysis, the vortex-tracking algorithm used was not able to find a reasonable center of circulation after 00 UTC 31 October, 12 h before NHC was unable to continue tracking the storm.

The comparison of the simulated intensities against Verification likewise shows similar values (Fig. 3.4, top). The correlation coefficient ( $r$ ) and Root-Mean-Square Error (RMSE) of minimum central sea level pressure (SLP; Table 3.2) indicate that the *3-Way*

coupled simulation had the best correlation (0.938) and significantly reduced RMSE (6.9 hPa) among all cases. The worst performing simulation was *WRF-OML*, with  $r$  of 0.91 and RMSE of 9.0 hPa.

Greater variance appeared between the simulated strength of all four experiments and verification (Fig. 3.4, bottom). The wave-uncoupled models all yielded similar results with the greatest differences occurring with the wave-coupled experiment, a consequence of the parameterization of surface roughness in the *3-Way* simulation. The *3-Way* experiment showed the lowest correlation coefficient (0.80; Table 3.2), the largest RMSE ( $9.6 \text{ ms}^{-1}$ ) and the greatest variability of all the experiments. As previously stated, model results are sensitive to parameterization of the surface roughness in wave-coupled models, an important factor in coupled TC modeling that deserves more research.

In order to examine why the differences between intensity and strength exist, a Student's T-test of significance is used in order to determine the statistical significance of the results (Table 3.3). Unfortunately, due to initialization 48 hours before landfall, and verification available every 6 h, the number of verification points ( $n=8$ ) are too few to determine statistical significance of the simulation error. As a result, we cannot analyze the statistical significance of the residuals versus verification.

A look at the statistical significance between simulations (Table 3.3) determined that they are all significant in examining differences in simulated SLP. Examining differences in simulated maximum wind, *Static* vs *2-Way* ( $p=10.58\%$ ) and *OML* vs *2-Way* ( $p=9.37\%$ ) were determined to be statistically insignificant, the rest of the differences were determined to be

statistically significant. This indicated that the differences in the strength demonstrated by the *3-Way* to other model configurations case are statistically significant.

In order to examine the errors (residuals), these are plotted these for the first 60 h of the simulation (Fig. 3.5). First, examining the SLP error (Fig. 3.5, top) before landfall (occurring around 36 h), the errors in SLP prior are minimal after initialization. There is slight ( $\sim 1-3$  hPa) over-intensification (low SLP) during this period. During and after landfall, the simulated storm weakens slower than verification, resulting in a more intense simulated storm compared to verification. Overall, the residuals demonstrate over-intensification of the simulated storm with miniscule differences prior to landfall, getting worse after landfall. The examination of why the intensity decreased after landfall faster than verification is outside the scope of this study of ocean coupling and wish to focus instead on the evolution of the storm prior to and during landfall, where our simulations performed well against verification.

Next, examining the strength error (Fig. 3.5, bottom), there is no significant pattern of the residuals. At initialization, the residual demonstrates a weaker storm than verification, owing partly to the global-scale model from which the atmospheric solution is initialized. Within 6 h, the storm strengthens to match verification and then over-strengthens until 12 h prior to landfall. Examining the differences among the experiments, which are statistically significant, we can see that the *3-Way* coupled case represents an outlier, with  $17\text{ms}^{-1}$  over-strengthening at its peak.

Examining the differences in bottom stress calculation (Fig. 3.6) we see that the bottom stress fields at this time of peak over-strengthening (00 UTC 29 October) paint a

complicated picture of the interaction between the atmosphere and ocean surface. At this particular time, we demonstrate wind speed (left column), significant waves (middle column; only available for the *3-Way* coupled experiment), bottom stress (right column) and the difference between these values (bottom row).

Within the rain bands wrapping the storm, there are significant differences that are attributed to the difference in bottom stress calculation (via the roughness length,  $z_0$ ). The largest difference, where the *3-Way* model had  $>15 \text{ ms}^{-1}$  increase in wind speed ( $38.2 \text{ ms}^{-1}$  resolved by the *3-Way* simulation versus  $23.1 \text{ ms}^{-1}$  resolved by the *2-Way* simulation) was found to the southwest of the eye, close to the eyewall. Examining this region, the waves were relatively small (5.63m), as the result one would expect the bottom stress to also be small. However, the bottom stress calculation at this grid point is significantly higher ( $1.66 \text{ ms}^{-1}$  versus  $1.11 \text{ ms}^{-1}$ ), owing to the feedback faster winds have on the bottom stress. To demonstrate variability, I have also noted the bottom stress at these locations 1 hour before. At this same grid point, one hour previous, the *3-Way* simulation bottom stress was half of this value ( $0.83 \text{ ms}^{-1}$ ) and was less than the *2-Way* experiment ( $0.98 \text{ ms}^{-1}$ ) at the time.

This variability is demonstrated to show that point-to-point calculations of wind speed are highly variable in both time and space, owing to many simulation characteristics. As a result, the calculation of storm strength, based simply on the largest wind speed found in the area of the storm's eye, is highly variable. Therefore, comparisons of our simulated strength to verification (only available every 6 h) suffer in some instances despite accurate representation of intensity. Wind speed variation as the result of wave feedback, boundary layer interaction and surface roughness parameterization in intense storms is an area of

current study, and a complicated process that is deferred to other investigations. As demonstrated by the aforementioned temporal variability, this investigation would require frequent output intervals to investigate the surface roughness parameterization and effects on the bottom boundary layer and wave impacts to heat fluxes, which is outside the scope of this study of ocean coupling impacts on extratropical transition.

A number of marine environmental variables of potential importance to tropical and extratropical cyclones were examined (Fig. 3.7). Observations were not available consistently, as remote-sensed or *in situ* data were missing during the storm (e.g., satellite SST data obscured by cloud cover). Our 3-Way coupling experiment provided temporally and spatially continuous modeled data time series for analysis. This analysis began at model initialization (12 UTC 28 October) and continued until just after landfall (00 UTC 30 October).

As previously analyzed to determine our simulated storm track, positions for the grid points of lowest SLP were used to determine the locations of the storm center, then extracted SST, ocean heat content (OHC) and vertical wind shear at these locations to examine how they changed as the storm center moved (Fig. 3.7) from open ocean to the coast. OHC was calculated using a formula similar to (Leipper and Volgenau 1972)

$$OHC = \rho c_p \int_{T=16^{\circ}\text{C}} [T(z) - 16] dz ,$$

where  $\rho = 1025 \text{ kg m}^{-3}$ ,  $c_p = 3850 \text{ J kg}^{-1} \text{ }^{\circ}\text{C}^{-1}$ , and temperature anomaly (relative to  $16 \text{ }^{\circ}\text{C}$ ) is integrated with depth relative to the  $16 \text{ }^{\circ}\text{C}$  isotherm. The  $26 \text{ }^{\circ}\text{C}$  isotherm used in Leipper and Volgenau (1972) was too warm for our analysis, as underlying SST during Sandy repeatedly

fell below this value after Sandy crossed the Gulf Stream. In addition, the method of Rhome et al. (2006) is followed to calculate the atmosphere shear values: an annulus around the storm center was created, with an inner radius of 200 km and an outer radius of 800 km. The vertical vector differences of the annulus at two levels were then used to compute the shear.

In particular, analyzing the shear between 850 and 500 hPa, i.e.,  $|\vec{U}_{850-500}| = |\vec{U}_{850} - \vec{U}_{500}|$

(Rhome et al. 2006) as well as between 850 and 200 hPa, i.e.,  $|\vec{U}_{850-200}| = |\vec{U}_{850} - \vec{U}_{200}|$

(Emanuel et al. 2004), as both have been demonstrated to correlate well with time-dependent variations in storm intensity (minimum SLP) and strength (maximum 10 m wind). The translation speeds were estimated using the model-simulated and NHC-observed tracks until after Sandy made landfall, when the center of rotation became less well defined.

The minimum SLP simulated by the *3-Way* coupled model and the Verification minimum SLP (Fig. 3.7a) both demonstrate a slow increase (decreasing SLP) until 5.5 h before landfall (2330 UTC 29 October; Blake et al. 2013). The *3-Way* simulation resolved landfall about 1.5 h earlier. NHC best track wind speed gradually increased, peaked at 12 UTC 29 October (11.5 h before landfall), and then declined as the storm exited the Gulf Stream, made landfall, and headed inland (Figs. 3.7b,c,d). The temporal inconsistency between the increasing intensity and decreasing strength immediately prior to landfall is demonstrated in verification, as well as our experiments. The reason the strength diminishes prior to landfall is likely due to the storm impacting coastline. Sandy was unique in that the strongest winds of the storm were found in the western side of the track. In addition, Sandy's impact track was extremely unique, Hall and Sobel (2013) determined this to be an event

with a 714 year return period. The combination of these unique factors resulted in the strongest winds impacting the shoreline before the eye made landfall. As a result, the 10 m winds were reduced due to impacting the shoreline well before the eye crossed onto land, reducing storm strength.

SST at the storm center stayed relatively constant ( $\sim 25$  °C) as Sandy moved from the Sargasso Sea and crossed the Gulf Stream. This is shown spatially at model initialization in Fig. 3.3 and track-following in Fig. 3.7c. The sharp decline of SST occurred as the storm center moved northwest of the Gulf Stream and encountered cooler shelf water approximately 12 h before landfall. Correspondingly, the OHC (Fig. 3.7d) at the storm center increased steadily as Sandy moved over the Sargasso Sea and Gulf Stream waters, then decreases sharply as it entered the shelf waters with lower SSTs and thinner mixed layers.

Concurrent with the gradual decrease in minimum SLP (Fig. 3.7a) and increase in maximum wind speed (Fig. 3.7b), both shear parameters (Fig. 3.7e) gradually decreased until just prior to landfall. Although, this signal was much more subtle for the 850-500 hPa shear parameter. As the storm moved across the coastal ocean, interaction with an upper-level trough approaching the East Coast of the U.S. (Blake et al. 2013; Galarneau et al. 2013; Shen et al. 2013; Munsell and Zhang 2014) resulted in the significant deep-layer shear present in our simulations. The presence of this deep-layer shear with continued intensification confirms the assertions of Galarneau et al. (2013). Increasing baroclinicity and frontogenesis were keys to the secondary intensity maximum shortly before landfall. Before landfall, the storm was non-tropical to the extent that the substantial vertical shear would not be expected to cause weakening. However, somewhat paradoxically, if the storm was

completely extra-tropical as described in Galarneau et al. (2013), a reduction in shear should weaken the storm. Our results demonstrate that the storm continued to intensify through landfall, in a region of decreasing shear. This result calls into question the degree to which the simulated storm may have been tropical or extra-tropical, and the result is demonstrated regardless of coupling complexity.

The translation speed (Fig. 3.7f) almost doubled (from  $5 \text{ ms}^{-1}$  to  $10 \text{ ms}^{-1}$ ) until just prior to landfall, resolved in both the *3-Way* simulation and the NHC best track. As a result of increased translation speed of Sandy, among the aforementioned uncoupled processes (Galarneau et al. 2013; Shen et al. 2013; Munsell and Zhang 2014; Blake et al. 2013), the effect of a cooler SST was negligible towards the minimum SLP and maximum winds of the storm in the hours leading up to landfall.

### 3.3.2 Ocean

Along-track ocean variables (SST and OHC) were analyzed in discussion of the storm's extratropical transition in the previous section. In addition to these variables, comparisons between simulated and observed SST were also used to evaluate model performance in resolving the ocean condition. The five buoys selected (shown in Fig. 3.3) featured data over the entire storm event with minimal gaps. Three buoys were chosen to the south and two to the north of the storm track in order to discern any cross-track bias. One buoy was chosen off of the shelf (41004). Only the model experiments with time-dependent variables were considered for these comparisons (i.e., the *WRF-Static* experiment was excluded from the SST comparison). Statistical analysis to determine the correlation

coefficient and RMSE were completed over the entire simulation (12 UTC 28 October through 00 UTC 3 November). This resulted in 133 temporal points of comparison at each buoy, although some small gaps from missing *in situ* data are present.

For the SST analysis (Fig. 3.8), the worst performing simulation was the *WRF-OML*, with an average correlation coefficient at all five locations of 0.62 and RMSE of 1.70 °C. The *2-Way* and *3-Way* cases performed similarly to each other, with average correlation coefficients of 0.85 and 0.81 and RMSE of 0.98 and 0.96 °C, respectively. At the buoy well to the south of the storm track (44099), the *2-Way* and *3-Way* simulations had correlation coefficients of 0.99 and 0.98, and RMSE values of 1.17 and 0.71 °C, respectively. At this location, the *3-Way* simulation performed markedly better than the *2-Way* experiment.

### 3.3.3 Wave

The five buoys selected (shown in Fig. 3.3) featured data over the entire storm event with minimal gaps. In order to examine *in situ* comparisons to wave fields, three buoys were chosen to the south and two to the north of the storm track in order to discern any cross-track storm bias. One buoy was chosen off of the shelf (41004). Only the wave-coupled experiment (*3-Way*) featured significant wave heights and was considered for these comparisons. Significant wave height comparisons showed good agreement with buoy data at the three northern stations, suggesting the *3-Way* coupled simulation provided an excellent wave field as Sandy moved onshore (Fig. 3.9). The worst comparison was at buoy 44099, located farthest south from the storm track. At this location, the correlation coefficient was still good: 0.95. However, the model overestimated the waves with the RMSE of 1.60 m. The

resolution of the ocean grid (7 km), plus unresolved nearby shoreline and the shallow depth (18.35 m), are likely culprits for the deficiency at this location. The best performing location was at buoy 44097, the farthest to the northeast and the deepest on the shelf (50.83 m), where the correlation coefficient ( $r$ ) was 0.96 and RMSE was 0.66 m.

### *3.4 Summary and Conclusions*

Superstorm Sandy made its way up the coast as a hurricane, interacting with ocean features in the Sargasso Sea, Gulf Stream and shelf waters of the western North Atlantic Ocean before transitioning into an extratropical system mere hours before landfall. Utilizing the COAWST modeling system to quantify evolutions of marine environmental changes during this transition, we found that, regardless of coupling complexity, model simulated tracks were all similar to the observations, suggesting the storm track was largely determined by large-scale synoptic atmospheric circulation, rather than by local processes resolved through model coupling. The translation speed also significantly increased (doubled) as Sandy moved across the shelf. As a result, ocean coupling did not have a drastic effect on simulated intensity and strength.

Including wave coupling in the *3-Way* (ocean-atmosphere-wave) coupled configuration produced the most significant differences in the storm strength comparisons. These differences were attributed to the atmospheric boundary layer interactions with surface roughness, calculated with consideration to wave heights. More research on wave-induced surface roughness parameterizations is needed.

Together, the environmental conditions of Sandy prior to its landfall demonstrate that decreasing SST and OHC directly below the eye contributed to the storm losing its tropical characteristics several days prior to landfall. Despite that, Sandy had slight increases in strength and intensity concurrent with reduced atmospheric shear as it accelerated towards the coastline while becoming a powerful extratropical system. Such a tropical-to-extratropical transition is crucial for storm classification during landfall, because the difference between naming a storm a hurricane or an extratropical cyclone has great implication for insurance claims. More research and observations are needed to better characterize the tropical to extratropical transition process of future storms similar to Sandy.

Comparisons between simulated and observed SST time series at five buoys located on the U.S. mid-Atlantic coastal shelf showed the simulation of WRF coupled to a simple 1-D ocean mixed layer model (*WRF-OML*) had the largest errors. The *3-Way* ocean-atmosphere-wave coupled model reproduced well the observed wave heights at four of the five locations; the one outlier was located in the shallowest water and closest to shore. A higher grid resolution ocean/wave model is needed to better resolve the wave dynamics there.

## **4 Examination of Hurricane Irene (2011) Using Coupled Model Forecast**

### *4.1 Introduction*

Hurricane Irene was a significant TC that made landfall twice on the east coast of the United States (U.S.; Avila and Cangialosi 2011). This hurricane made a tremendous impact over those two landfalls. The first landfall, near Cape Lookout, North Carolina (NC) resulted in widespread damage to homes and trees on the Outer Banks of NC. Surge and flooding from Irene resulted in multiple breaches along Highway 12, similar to breaching found during Hurricane Isabel (2003; Warner et al. 2010). The next landfall occurred near Atlantic City, New Jersey (NJ) approximately 22 hours later. The second U.S. landfall was significantly weaker than the first. However, intense flooding and storm surge damage was reported across several states. Record-breaking crests were reported in NJ and eastern Pennsylvania (PA) along with major flooding due to torrential rain. Along the NJ coastline there was widespread flooding along with extensive beach erosion.

In contrast to Superstorm Sandy, New York City, New York (NY) was spared the brunt of strong winds and surge. The strongest winds during the second landfall were located to the east of the storm path, over water. Nevertheless, recorded storm surge of 1-2 m resulted in hundreds of millions of dollars in damage across the southern portion of NY. After translating into northern NY and New England (NE), intense rainfall was maintained for days resulting in the most significant flooding to this region since 1927. In this area, over 2400 roads, 800 buildings, 300 bridges were damaged or destroyed by severe flooding. Three towns in the Catskill Mountains of NY were rendered uninhabitable.

In summary, Irene's 2 landfalls in the U.S. east coast made the storm the 7<sup>th</sup> costliest TC to impact the U.S. Insured losses accounted for \$4.3 billion in damage, doubling for estimated uninsured loss the total storm loss was \$8.6 billion. 49 lives were claimed due to the direct impacts of this storm, 41 deaths occurred in the mid-Atlantic and northeastern U.S. While relatively weak at landfall (Saffir-Simpson category 1 of tropical storm intensity), this was a very significant storm characterized by intense flooding to several areas of the east coast of the U.S. from South Carolina (SC) northward.

The synoptic history of Hurricane Irene began as a tropical wave off of the west coast of Africa and became a tropical storm near 00 UTC 21 August 2011. After gaining hurricane strength while transiting the Caribbean Sea, Irene reached a peak strength of  $55 \text{ ms}^{-1}$  with an intensity of 957 hPa at 12 UTC 24 August. Irene's west-northwestward track then shifted eastward on 24 August as a result of a mid-tropospheric trough that developed over the eastern U.S. During the next few days, Irene's winds decreased in strength but the storm broadened and continued to intensify, reaching a minimum central pressure of 942 hPa on 06 UTC 26 August. The radius of hurricane winds continued to expand during this period, reaching 150 km in the northeast quadrant.

Irene weakened up until its first landfall at Cape Lookout, NC on 12 UTC 27 August. Saffir-Simpson category 1 winds were reported along the Albemarle and Pamlico Sounds and Outer Banks of NC. After passing through NC, Irene weakened slightly while moving north-northeastward along the east coast until making a second landfall at Brigantine Island, New Jersey at 0935 UTC 28 August. The storm continued north-northeastward through eastern

NY and NE, becoming extratropical on 29 August. The wide breadth of the remaining rainbands resulted in severe and extensive flooding to northern NY and NE.

Compared to the previous five years of NHC TC track forecasts, Hurricane Irene's forecast demonstrated improvement to previous tropical systems. Fig. 4.1 demonstrates agreement between a 73-member ensemble of track forecasts available from the Global Ensemble Forecast System (GEFS) at NHC. However, climatology and persistence models were also improved, demonstrating that the hurricane was not difficult to forecast.

Compared to the previous five years of NHC TC strength forecasts, Hurricane Irene's strength forecast was worse. This was in spite of climatology and persistence models demonstrating lower forecast error in previous years. The storm forecast showed a consistent over-strengthening bias through the first landfall in NC, especially with higher-resolution regional scale models. Fig. 4.2 demonstrates the wide spread of a 73-member ensemble of strength forecasts from the GEFS. Overall, the coarser scale global (regional) models tended to overestimate (underestimate) Irene's forecasted strength. As our Hurricane Ivan study in Chapter 2 demonstrated a reduction of this over-strengthening bias due to ocean interaction, Hurricane Irene appeared to be a good forecast case for application of the COAWST model.

Precipitation has an obvious impact on ocean salinity beneath moving TCs. As a result of freshwater input through intense precipitation, the upper-ocean should experience some freshening and cooling. As fresh water is less dense than saline water, a reduction in salinity has been demonstrated to have a stabilizing impact due to increasing the density stratification in the first few meters of the ocean (Asher et al. 2014). One plausible impact of

this is that the increase in salinity stratification would result in reduced mixing, resulting in stronger TCs due to reduced SST cooling.

This chapter is organized as follows: Section 2 provides the model configuration and used to couple the three independent models together, the fields that are exchanged to each individual model, and the five uncoupled and coupled experiments completed to examine the effect of model coupling with increasing complexity in forecasting Hurricane Irene. Results and Discussion are given in Section 3, the experiments conducted with Hurricane Irene as a test case focus on two areas. The first area is demonstrating improvement in forecast track and strength through coupling to an ocean model through the COAWST modeling system. The second area is to examine the salinity impact the TC has on the upper ocean. Concluding remarks in Section 4 follows this.

## *4.2 Methodology*

### *4.2.1 Model Configuration*

As in previous case studies, the Coupled Ocean-Atmosphere-Wave Sediment Transport (COAWST; Warner et al. 2010) model was used. The COAWST configuration for our Irene experiments utilized the Weather Research and Forecasting (WRF) atmospheric model version 3.2.1 (Skamarock et al. 2008), Regional Ocean Modeling System (ROMS) ocean model version 3.3 (Shchepetkin and McWilliams 2005; Haidvogel et al. 2008), Simulating Waves Nearshore (SWAN) wave model version 40.81 (Booij et al. 1999).

We utilize the USEast domain (Nelson and He 2012) for this case. The WRF domain encompasses the entire U.S. East coast on a 225x236 grid with spacing of 15 km. An inner

vortex-following 5-to-1 nest encompasses the entire TC on a 3 km grid measuring 301x301. This inner-nest was required to resolve the TC structure of the eye and eyewall in the atmospheric model (Hill and Lackmann 2009; Gopalakrishnan et al. 2012; Fowle and Roebber 2003; Done et al. 2004) as well as in the ocean model (Halliwell et al. 2011). The time-step of the outer (inner) domain is 50 s (10 s). Both parent and nested domains feature 31 terrain-following hydrostatic pressure vertical coordinates (Skamarock et al. 2005). As in the Sandy case, our ROMS and SWAN domains are located inside of the WRF domain with a minimal space between the boundaries of the WRF and ROMS/SWAN domains. The ROMS and SWAN domains are collocated with 7-10 km grid spacing on grids of 773x831 grid points. The ROMS model utilizes 30 terrain-following vertical coordinates and a 120 s baroclinic time-step. Open boundaries are found in the ROMS domain in the south and east. In our SWAN setup, directional space was utilized with 36 directional bins and 24 frequency bins of 1 s width between 1 s and 25 s. The co-located ROMS/SWAN grids do not feature a nested grid as they are not necessary (Halliwell et al. 2011).

As in our Ivan and Sandy studies, grid points had to be interpolated before model initialization for proper data exchange by the MCT. Interpolation weights were utilized in order for the models to exchange information across their spatial domains. The Spherical Coordinate Remapping Interpolation Package (SCRIP) was used to implement a conservative remapping scheme for this purpose (Jones 1999; Warner et al. 2010). The weights are computed using a nearest neighbor bilinear interpolation and then are read in during initialization for use during the models' iteration. Model fields were exchanged every 10 minutes.

One of the goals of this particular case study is to demonstrate the impact of ocean coupling on TC forecasting. As a result, forecast fields are utilized for the atmospheric model. Unfortunately forecast fields for the ocean and wave environments were not available due to logistical problems. During the course of the storm evolution, 0.5° Global Forecast System (GFS) fields were captured and saved for the entire 192 hr forecast period available. This forecast data was retrieved for 10 days, from 00 UTC 20 August through 00 UTC 30 August, as part of the North Carolina State University (NCSU) integrated operational nowcast/forecast system of the South Atlantic Bight (SAB) and Gulf of Mexico (SABGOM; Xue et al. *in press*). A number of simulations were run, in order to determine the best initialization time for a forecast simulation of Hurricane Irene utilizing a WRF-only configuration. Results of track, strength and intensity were compared to NHC Best Track (Avila and Cangialosi 2011) data within a month after the storm. In addition to reasonable comparisons, advanced lead time was sought.

Based on these uncoupled, WRF-only, model comparisons balancing agreement with NHC Best Track data and reasonable lead time, the initialization time for our experiments was determined to be 12 UTC 25 August, approximately 48 hr before landfall along the Outer Banks of NC and approximately 68 hr before landfall in NJ. After determining the best initialization time for the uncoupled simulation, hindcast fields were gathered for the ROMS and SWAN models. The 1/12°, global HYbrid Coordinate Ocean Model with Naval Research Lab (NRL) Coupled Ocean Data Assimilation (HYCOM/NCODA) solutions were utilized for ROMS model spin-up and boundary conditions. The HYCOM/NCODA model assimilates satellite SSH and SST as well as in situ observations from expendable

bathythermographs (XBTs), ship board conductivity-temperature-depth (CTD), and ARGO floats (Chassignet et al. 2007). The SWAN model was initialized from a null state, allowing waves to build over the first few hours of iteration, while the TC was far from shore.

Boundary conditions for the SWAN model were derived from the WaveWatch 3 global wave model [Available: <http://polar.ncep.noaa.gov/waves/index2.shtml>] and updated every 3 hr.

The WRF model physics include grid resolved precipitation using the WRF Single-Moment 6-class microphysics scheme (WSM-6; Hong and Lim 2006) on both grids. This first-order microphysics scheme features water vapor, cloud water, cloud ice, rain, snow, and graupel. On the 15 km outer grid, the Kain-Fritsch CP scheme (Kain 2004) was used to parameterize precipitation processes on a sub-grid scale. The inner 3 km mesh was able to resolve precipitation adequately on a grid scale and no cumulus parameterization was necessary (Molinari and Dudek 1992). Longwave and shortwave radiation physics were computed using the Rapid Radiative Transfer Model (RRTM; Mlawer et al. 1997) and the Dudhia (1989) scheme, respectively, called every 15 (3) minutes on the outer (inner) grid. The Eta surface layer scheme (Janjić 1996; 2002) based on similarity theory (Monin and Obukhov 1954) physics option was used along with the Noah land surface model (Chen and Dudhia 2001) for both grids. The Mellor-Yamada-Janjic turbulent kinetic energy planetary boundary layer (PBL) model (Mellor and Yamada 1982; Janjic 1990, 1996, 2002) was called every time step on both WRF domains.

For the ROMS model, in order to pass HYCOM/NCODA tracer (salinity and temperature) and 3-d velocity fields across the boundaries to ROMS, Marchesiello et al. (2001) was utilized for the open boundaries to the south and east of the domain. In this

scheme, Orlanski-type radiation conditions were used in conjunction with relaxation (with timescale of 0.5 days on inflow and 10 days on outflow) of the tracer fields. Flather (1976) was used for the free surface and depth-averaged velocity boundary conditions with the external values defined by HYCOM/NCODA, updated every day. Mellor and Yamada (1982) was used to compute vertical turbulent mixing, as well as the quadratic drag formulation for the bottom friction specification.

The SWAN model utilized nonlinear quadruplet wave interactions. Wave bottom dissipation was parameterized using the Madsen et al. (1988) formulation, with an equivalent roughness length scale of 0.05 m. The depth-induced breaking constant, e.g., the wave height to water depth ratio for breaking waves, was set to 0.73. Wind-wave growth was generated using the Komen et al. (1984) formulation. A backward-in-space, backward-in-time advection scheme was used for iteration.

#### *4.2.2 Experimental Design*

In order to examine the impact ocean/wave interaction has on the TC, 5 experiments were conducted, shown in Table 4.1. These experiments were designed to include increasing complexity in resolving the ocean environment. The first experiment, *WRF-Static*, iterates the WRF model alone and utilizes the Real Time Global SST (RTG-SST; Gemmill et al. 2007) condition at initialization that remains unchanged throughout the course of the model run. The second experiment, *WRF-Dynamic*, is the same as in the *WRF-Static* case except featuring 6 hr interpolation of the RTG-SST product. The third experiment, *WRF-Filter*, follows from *WRF-Dynamic* utilizing the 6 hr interpolated RTG-SST product. In the *WRF-*

*Filter* case, we utilize the method of Minobe et al. (2008) and perform a 1-2-1 filter in zonal and meridional directions in order to remove high resolution features from the RTG-SST product. As in Minobe et al. (2008), the filter was applied 100 times and the resultant SST condition is shown in Fig. 4.3. The first coupled simulation is demonstrated in the *2-Way* experiment, featuring coupling between the WRF and ROMS model (as in previous case studies). Finally, the fully coupled WRF-ROMS-SWAN configuration is demonstrated in the *3-Way* case. The *2-Way* case was also run with 2 more experiments utilizing different treatment of the surface salt flux. In *ANA\_SSFLUX*, the model is run with no freshwater input into the surface ocean. In *EMINUSP*, the 2-Way experiment is run with freshwater input determined by the net difference between evaporation and precipitation. These results are only used in examining the salinity impacts on the ocean and the impact was demonstrated to be minimal. As a result, the *2-Way* case used everywhere else utilizes *EMINUSP*.

### *4.3 Results and Discussion*

#### *4.3.1 Atmosphere*

All experiments performed well in simulating Irene's track, but there was some delay in forecasted landfall. Fig. 4.1 demonstrates that all experiments performed inside of the swath of the forecast track ensemble with initialization at 12 UTC 25 August. Fig. 4.4 demonstrates the experiment tracks alone. As in the two previous case studies, the impact of coupling on the track forecast was limited as forecast track is largely dependent on large-scale forcing mechanisms (Marks and Shay 1998).

Both the location of the two landfalls were accurately represented. The forecasted timing of the first landfall occurring about 5 hr after of the actual landfall (17 UTC 27 August). A 4-panel plot depicting the atmosphere, ocean and wave environments in the 3-Way case at the time of the NC landfall are demonstrated in Fig. 4.5. The location of the second landfall was harder to resolve due to the weakening storm and ill-defined center of circulation. The best estimate of the simulated second landfall is 12 UTC on 28 August, about 3 hr after the actual second landfall. After the second landfall, the simulated storm rapidly weakens and the center of circulation becomes even harder to define. In all of the forecast simulations, the storm center does not proceed as far to the north as demonstrated by the NHC Best Track position. However, the massive breadth of the storm circulation certainly had some impact on northern NY and NE as had actually occurred.

All forecast simulations performed well in simulating the storm strength (maximum wind in  $\text{ms}^{-1}$ ), especially compared to the 73-member forecast ensemble (Fig. 4.2). Fig. 4.6 shows that both uncoupled and coupled simulations demonstrated agreement in simulating the Irene's maximum wind. Table 4.2 demonstrates the Root-Mean-Square Error (RMSE) of strength were between 4.35 and 4.70  $\text{ms}^{-1}$ . While this seems like a large bias, its important to remember that this is a forecast and that the forecasted strength is superior to other forecasts available from the NHC during the storm. Also shown in Table 4.2, the strength correlation coefficients ( $r$ ) for the wave-uncoupled models were excellent, between 0.96 and 0.90. The wave-coupled (3-Way) case featured the worst correlation coefficient of 0.86. The strength plot in Fig. 4.6 shows the variability that occurs with introducing wave coupling and the sea

surface roughness parameterization was investigated. The sea surface roughness was parameterized using Taylor and Yelland (2001)

$$\frac{z_0}{H_s} = A_1 \left( \frac{H_s}{L_p} \right)^{B_1} .$$

The decision to use this parameterization was based on several offline simulations of the 3-*Way* coupled configuration and comparisons to NHC Best Track data. This sea surface roughness parameterization performed best, compared to parameterizations from Oost et al. (2002) and Drennan et al. (2005). As in previous case studies, no parameterization should be considered “best”, and sensitivity runs should be completed to determine the most accurate simulation.

The forecasted intensity of Irene demonstrated less accuracy when compared to NHC Best Track, across all experiments. The RMSE values demonstrated a range of 11.39 and 14.65 hPa. High frequency oscillations resulted in mediocre correlation coefficients ( $r$ ) as well, between 0.57 and 0.66. The best RMSE (11.39 hPa) was the case with the least ocean feedback, *WRF-Static*, which also had the worst correlation coefficient ( $r=0.57$ ). Interestingly, the next-best RMSE (12.42 hPa) was the case with the most coupling, *3-Way*. This case featured the next-worst correlation coefficient ( $r=0.58$ ). Forecasted ensemble intensity is not a product available from NHC, so comparisons of these forecasts to operational models are not possible.

Fig. 4.8 demonstrates comparisons of the 5 experiments to *in situ* data collected from 6 buoys of 10 m wind speed. Moving south to north (locations denoted in Fig. 4.7), along with the storm, the timing of the ramp-up and ramp-down storm impact on the 10 m is

apparent. Overprediction of the 10 m wind at the southern buoy (41010) is due to the slight westward jog the simulated storm made in all of the simulations. At 41036, south of the NC Outer Banks, the simulations had the storm impact the location directly and the eyewall-crossing signature (gradual increase, rapid decrease, rapid increase, gradual decline) is demonstrated. Verification showed that the storm moved to the east of this location and the increasing, decreasing, and increasing trend of storm passage is not demonstrated. Towards the end of the simulation, the simulated storm is over-strengthened in the *WRF-Static* case, this signal is repeated with the *in situ* data.

SLP comparisons to the buoy data long the U.S. east coast is conducted in Fig. 4.9. These figures show agreement between the simulations and buoy data. Similar discrepancies in the simulation occur at 41010 and 41036 as in the 10 m wind comparison above. At 41010, the overly strong SLP reduction is due to the simulated TC moving directly over the location, rather than translating to the east. At 41036, the impact of the storm is apparent in the wind time series, however the storm does not deepen sufficiently to match the SLP reported by the buoy. This signal is apparent in the remaining buoys to the north (44014, 44009, 44065), and is shown in Fig. 4.6 as the storm did not deepen to the intensity demonstrated by the NHC best track data. Despite this, the timing and magnitude of the SLP depression is well-forecast for this storm. As in the intensity comparisons of Fig. 4.6, the *WRF-Static* case demonstrated the lowest SLP (most intense) for the simulations.

As Hurricane Irene was an event characterized by severe flooding throughout the east coast of the U.S. (Avila and Cangialosi 2011), an analysis of forecast precipitation was conducted in comparison to the Global Satellite Mapping of Precipitation (GSMaP) satellite-

derived precipitation product (Okamoto et al. 2005; Kubota et al. 2007; Aonashi et al. 2009; Ushio et al. 2009). The GSMaP product is produced on a  $0.1^\circ$  spatial grid, with data available hourly from  $60^\circ\text{S}$  to  $60^\circ\text{N}$ . Fig. 4.10 shows the spatial extent of the storm precipitation as it makes landfall in NC. All of the simulations performed similarly and demonstrate the breadth shown in the GSMaP verification. As discussed with storm track, the forecast simulations are about 5 hr behind verification at landfall. As a result, the GSMaP storm is shifted slightly north of the simulated storms. Significantly greater precipitation is found to the north of the eye as the storm impacts NC, also demonstrated in the GSMaP verification.

In order to gauge the accuracy of the forecast simulations in predicting Hurricane Irene's heavy precipitation, we compare our forecast experiments to the GSMaP product in Fig. 4.11. Hourly precipitation flux ( $\text{mm hr}^{-1}$ ) is integrated over grid points in the parent domain utilizing the bounds established within the vortex-following moving nest. As a result, precipitation outside of the vicinity of the TC is ignored. In order to make a direct comparison between the 15 km outer grid and the  $0.1^\circ$  GSMaP grid, we interpolate the former to the latter. Integration of the grid points across the entire domain is then completed. There was significant noise in the GSMaP data, so a 36 hr low pass filter is applied.

The final comparison demonstrates that the forecast predicts the intensity of precipitation over the parent domain bounded by the vortex-following grid. Also, clear differences in precipitation exist between the different experiments. The *WRF-Filter* case demonstrates the least amount of precipitation among all of the experiments, in agreement with Minobe et al. (2008, 2010). The *WRF-Static* experiment featured the greatest amount of

precipitation, much larger than any of the other experiments. As discussed in previous cases, the unchanging SST, warmer in most of the spatial domain throughout the simulation, results in increased latent and sensible heat fluxes. As a result of these increased fluxes, storm intensity is increased along with enhanced precipitation. Minimal differences exist between the remaining experiments, including the 2- and 3-Way coupled cases. It is apparent that enhanced surface fluxes owing different parameterizations of surface roughness have minimal impact on storm-generated precipitation fluxes.

#### 4.3.2 Ocean

The ocean condition is analyzed in a manner similar to the previous case studies. In order to examine the differences in simulated strength and intensity, the SST condition is analyzed as a time series. For the majority of *in situ* analysis over the forecast period, the modeled SST was within 2° C of the observed value. The impact of the 1-2-1 running filter in the *WRF-Filter* case is apparent when compared to the *WRF-Dynamic* data over the same time period, in one case differing by more than 2° C (00 UTC 27 August at buoy 44065). The more significant differences between the *WRF-Filter* and *WRF-Dynamic* cases are plotted spatially in Fig. 4.3 with large differences found in the Mid-Atlantic Bight (MAB), demonstrated accordingly at buoys 44014, 44009, and 44065. Resolving the SST in the coupled forecast configurations proved a challenge in the area of the Gulf Stream. Large surface winds forced meanders in the Gulf Stream. These had distinctive impacts on the simulated and *in situ* SST, as apparent at buoys 41036 and 44014. At the location immediately south of New York City, NY (44065), a short-lived increase in SST is observed

shortly before 20 UTC 26 August. The coupled model simulations demonstrate this rapid increase and decrease in SST, however to a much greater degree than observed. This short-duration signal was reproduced by the uncoupled WRF experiments.

The ocean salinity budget is examined in a method similar to how the heat budget was examined with Hurricane Ivan in Chapter 2. As in the Hurricane Ivan case, the *2-Way* experiment is used in order to remove any effects that wave coupling might have on the ocean dynamics. Three point locations were chosen for a time series analysis (Fig. 4.13). The first location, S1, to the southern part of the storm track is in the interior of the Sargasso Sea and is off the continental shelf. The second location, S2 is also in in interior of the Sargasso Sea but is on the continental shelf. The third location, S3 is located off of Cape Hatteras, NC in a region where the Gulf Stream frequently meanders.

At point S1 (Fig. 4.14), the contribution of horizontal and vertical advection begin to increase as surface winds increase before the arrival of the hurricane. During and after Irene's arrival (around 12 UTC 26 August), the horizontal and vertical terms of the salinity budget are large but out of phase with each other. The net result is a slight salinity increase followed by a decrease at the surface. However, a larger impact is found deeper. As the storm passes, the water between 60 m and 100 m depth undergoes alternating freshening and salinification due to advective processes. The vertical diffusion term is largely positive at the surface and negative beneath during the TC's passage. The local rate of change is largely positive at the surface as the storm translates through. Below roughly 50 m depth, the local rate of change oscillates positive and negative after the storm passes. The result is the water at the surface increases in salinity at this location about 0.3 PSU due to advection and

diffusion. The saltier water below remains largely unchanged with some slight ( $\sim 0.1$  PSU) freshening.

At the on-shore point within the Sargasso Sea, S2 (Fig. 4.15), some notable differences occur. The most apparent difference is the increase in contribution to the local rate of change that occurs as a result of the influence of advective terms. At the surface, freshening due to vertical diffusion combines with strong surface advection of fresh water to generate a surface pool of fresh water as the hurricane passes on 00 UTC 27 August. This is evidence of the precipitation impact that the TC had on the upper-ocean salinity gradient, a much stronger signal than that found at point S1. After the TC passes, strong advective and diffusive processes rapidly remove the fresh water, increasing the salinity from 36.0 to 36.2 PSU over the course of a few hours. Below the surface, the brackish water increases in salinity but maintains a similar depth after the fresh water pool disappears.

The final point, S3 (Fig. 4.16), off of Cape Hatteras, NC is in a region where Gulf Stream meanders are frequent and have drastic impacts on the SST and surface salinity of this region. Similar oscillations in horizontal and vertical advection are found in this region, but as it was to the east of the storm track, the magnitude is much smaller than at points S1 and S2. As the storm passes to the west on 12 UTC 27 August, a drastic change in the upper ocean salinity occurs as the Gulf Stream was forced further offshore. As demonstrated by the horizontal advection term, the later half of 27 August demonstrates intense increasing salinity. The vertical diffusion term shows significant freshening of the deeper (approximately 50 m to 90 m) water, but an increase in salinity in the upper (from the surface to approximately 40 m). The net change in this is a strong salinification of the entire water

column after approximately 12 UTC August 27, concurrent with Irene's passage to the west. The resultant change in salinity is drastic, increasing the upper 50 m from less than 35.4 PSU to over 36.5 PSU over the course of 2 days.

In order to demonstrate the impact of precipitation on the ocean salinity, we completed another *2-Way* experiment where we utilized an analytical surface salinity flux (*ANA\_SSFLUX*) instead of computing it based on the difference between the evaporation and precipitation (*EMINUSP*) fields from WRF. The differences between the budgeted fields at all 3 locations were extremely minimal and therefore not shown. As a result, the precipitation flux into the ocean had a minimal impact on the upper-ocean (upper 100 m) salinity budget.

The minimal impact of the upper-ocean surface salinity is examined further by completing cross-sections at the 3 point locations, extended outward east and west as denoted by Fig. 4.17. As Irene made landfall close to point S3, we extended this transect further east instead of over land to the west. The large variance of upper-ocean salinity required usage of different colorbars in order to discern the most detail possible.

The cross-section furthest to the south (S1; Fig. 4.18) demonstrates the earliest arrival of Hurricane Irene. At initialization, there is an apparent gradient of salinity increasing from west to east. This gradient is maintained through the model experiment. At 10 UTC 26 August, asymmetric surface freshening is a result of the northern rain bands of the storm making an impact. A few hours later, on 00 UTC 27 August the freshwater is mixed throughout and the precipitation signal is immediately, in agreement with Asher et al. (2014). At model termination, the cross-section of salinity at through S1 is decidedly more saline

through the entire plot, with a strong west-east gradient of salinity present. At this location the peak of precipitation flux was approximately 30% greater than the 2 remaining locations.

Moving up the coast with the storm, the next cross-section at S2 (Fig. 4.19) initializes with a weak column of saline water approximately 70 km to the east of the storm center. The tongue of surface salinity is also present in Fig. 4.17. As Irene arrives around 21 UTC 26 August, there is a strong signature of asymmetric precipitation. The strongest rainfall to the east of the storm center completely erodes the column of salinity found at initialization. This response is found 2 hr after the peak of precipitation flux into the ocean. This freshwater is rapidly mixed and 17 hr later, the surface freshwater signature is absent from the analysis. For the rest of the simulation, the cross-section maintains roughly the same signature with minimal change. At this location, Irene's impact eliminated the column of saline water to the east and reduced the overall west-east stratification.

The cross-section furthest to the north, with the latest storm impact, is demonstrated in Fig. 4.20. This location features the greatest stratification ( $>3$  PSU) of upper-ocean salinity, due to the presence of the saline Gulf Stream to the south and east as well as the fresher waters of the MAB to the north. As Irene made landfall on the Outer Banks of NC at 12 UTC 27 August, the coastal wind changed from downwelling-favorable to upwelling-favorable. The former helped to advect fresher MAB shelf water into the SAB coast. The latter helped to push this fresher water and the Gulf Stream further offshore. The freshwater along the coast is not due to river input as that was not considered in our experiments. The west-east stratification is reduced after the storm subsides but at the conclusion of the model run maintains a large magnitude ( $\sim 2$  PSU).

In addition to the examination of the storm salinity impact with vertical time series and X-Z cross-sections, a spatial analysis of the surface salinity budget is completed at 12 UTC 27 August (Fig. 4.21), as Irene is making its first landfall on the NC Outer Banks. Concurrent with the movement of the Gulf Stream offshore demonstrated by the salinity budget time series at point S3 (Fig. 4.16), the advection terms show movement of the Gulf Stream offshore south of Cape Hatteras, NC. To the north of Cape Hatteras, NC, increasing salinity is found with the advection terms but decreasing salinity due to the vertical diffusion. The decreasing salinity in the vertical diffusion term is likely due to the precipitation input and is confirmed through examination of the same fields in the *ANA\_SSFLUX* case (Fig. 4.22). In the *ANA\_SSFLUX* experiment, the negative vertical diffusion of salt at the surface reverses sign. Also interestingly, the advection of freshwater south of Cape Hatteras, NC is non-existent in the *ANA\_SSFLUX* experiment.

To further investigate the impact of precipitation on surface salinity, we analyzed a time series of lagged along-track precipitation flux and surface salinity. In order to negate the impact of other ocean processes, the surface salinity difference between the *EMINUSP* and *ANA\_SSFLUX* experiments are computed. The addition of a “lag” term was necessary as the precipitation directly under the eye of the hurricane would not be a good representation of the precipitation during the storm event. The lag interval represents the location of the storm center several hours in the future to determine the location of heavy precipitation in at that particular point in the forecast. To determine the best “lag” interval, we ran analysis from 0 to 18 hr into the future to find the highest anti-correlation. This interval was determined to be 10 hr (i.e. the location of the heaviest rain at forecast initialization is the location of the

storm center 10 hr later.) The anti-correlation coefficient (i.e. increasing precipitation should lead to decreasing surface salinity) with this lag interval was determined to be  $r=-0.57$ . This weak anti-correlation between the passage of heavy precipitation within the TC and the ocean salinity response further strengthens the assertion that the total ocean advection of salt had a much greater impact to surface salinity than the precipitation along the TC's track.

#### 4.3.3 Wave

Time series analysis of the wave forecast at the six buoy locations from Fig. 4.7 are shown in Fig. 4.24. With the atmospheric model in “forecast mode” and the aforementioned deficiencies in the atmospheric forcing, the wave model performed well. Correlation coefficients ( $r$ ) ranged from 0.76 (41004; located offshore of SC) to 0.96 (41014; east of the NC/Virginia border). It should be noted that three of the buoys had large data gaps ( $> 12$  hr) during the storm period. These periods of missing data could have contributed to lower correlation coefficients at 41010 and 41004.

Low RMSE values also indicate a good forecast of the wave condition throughout the US east coast. The station with the largest RMSE, 41010 (furthest to the south) indicate over-prediction of significant wave heights by the model. As the storm strength ( $\text{ms}^{-1}$ ) was largely underestimated throughout the early part of the *3-Way* model iteration, the likely cause of this overprediction was due to the westward shift in track (towards the buoy) between 00 UTC and 12 UTC 26 August. The smallest RMSE value was found at the northernmost station, 44065. At this buoy just south of New York City, NY, the RMSE was 0.84 but the wave model underpredicted the peak wave condition by over 2 m. This is likely

a consequence of the close proximity to the shoreline (24 m depth) and 7-10 km grid spacing utilized by the ocean and wave models.

#### *4.4 Summary and Conclusions*

We utilize the Coupled Ocean-Atmosphere-Wave Sediment Transport (COAWST) model in order to examine the dynamics of a Hurricane Irene, a significant TC which made 2 landfalls on the U.S. east coast in late August 2011. The damage from this storm was significant. The initial landfall occurred near Cape Lookout, NC on 12 UTC 27 August. The first landfall resulted in widespread damage from wind, surge, and flooding to the Outer Banks of NC. The second landfall occurred 21 hr later on Brigantine Island, NJ at 0935 UTC 28 August. The second landfall was significantly weaker but characterized by intense flooding and storm surge across several states of the Mid-Atlantic and Northeast U.S.

The TC was significantly weaker during its two landfalls than while translating northward through the South Atlantic Bight. At its peak, Irene had winds in excess of  $55 \text{ ms}^{-1}$ . This weakened to slightly over  $35 \text{ ms}^{-1}$  during landfall in NC and further weakened to  $30 \text{ ms}^{-1}$  during the second landfall in NJ (becoming a Tropical Storm at this point). Despite this, the damage from Irene was intense due, in part, to heavy precipitation and flooding. While weakening, the storm expanded extensively. The massive breadth of this storm was maintained well after landfall and the resultant flooding in New York and New England was unlike anything seen in this region since the November 1927 flood. Irene's two landfalls resulted in 41 direct fatalities in the Mid-Atlantic and Northeast U.S. In addition, the

combined landfalls resulted in approximately \$8.6 billion in damage, making this the 7<sup>th</sup> costliest TC to impact the U.S.

The forecast track was well-forecasted, however persistence and climatological models also scored well, indicating that this was an “easy” storm to forecast. During this same time period, Irene’s strength forecast was worse than the average error from forecasts issued during the previous five years. As with the track forecast, persistence and climatological models also performed better than the previous five years. The strength forecast error indicated consistent over-strengthening bias throughout Irene’s path along the U.S. east coast. During landfall, Irene was forecast to maintain Saffir-Simpson Category-3 intensity but impacted as a Category-1 hurricane. Based on this over-prediction of strength and earlier success in reducing this overprediction with the Hurricane Ivan experiments, we applied the COAWST model to this TC and analyzed its impacts on the atmosphere, ocean, and wave environments.

Our model was configured in a similar manner to our nowcast/forecast that was running during the event. As a result, we were able to use forecast fields for the atmosphere rather than hindcast. This gave us a unique ability to compare our forecast as if it were made that day. Unfortunately, ocean and wave forecast fields were not captured due to logistical issues, so those models were run in hindcast mode. We initialized our model run approximately 48 (68) hr before landfall in NC (NJ) and ran our model for 84 hr. An experimental design was established in order to examine the effects of SST representation in an uncoupled configuration (*WRF-Static*, *WRF-Filter*, and *WRF-Dynamic*), a coupled atmosphere-ocean configuration (*2-Way*), as well as a coupled atmosphere-ocean-wave

configuration. In addition, the treatment of the surface salinity flux in the *2-Way* case is examined through 2 additional experiments. The first experiment utilized no freshwater input to the ocean model (*ANA\_SSFLUX*). The second experiment featured freshwater input as the net difference between evaporation and precipitation at ocean grid points (*EMINUSP*). The difference outside of the salinity was minimal, so for examination of other fields, we simply utilize results from the *2-Way* configuration with *EMINUSP* activated.

All forecasts, uncoupled and coupled performed well in simulating Irene's track with some delay in predicting landfall. The location of both landfalls were accurately predicted. In addition, prediction of TC strength was better than forecast ensembles utilized by NHC with some noticeable impacts between the uncoupled and coupled model configurations. Comparing our results to the ensemble track and strength forecasts, our forecast performed better than both global and regional scale ensemble members utilized by NHC.

Forecast intensity was mediocre, and comparison to operational models is not possible as the data is not available. Comparing the different experiments yielded large differences in simulated intensity. None of the forecasts were able to intensify the storm to the degree represented by NHC best track data. The unchanging, WRF-Static yielded the most intense storm, followed by the 3-Way coupled configuration. These cases demonstrated the lowest RMSE, but worst correlation coefficient ( $r$ ).

*In situ* buoy comparisons demonstrate that a slight westward shift in track had a noticeable impact on time series comparisons in the South Atlantic Bight region (41010 and 41004). This impact was observed in 10m wind (high-bias), SLP (low-bias), SST (low-bias), and significant wave height (high-bias). Differences between the modeled and *in situ* fields

demonstrated impacts from coupling. The most intense storms resulted in the strongest wind, lowest SLP, and greatest change in SST (where available). Meanders in the Gulf Stream caused drastic differences between modeled and *in situ* observations at buoys near the western boundary current.

As Hurricane Irene was a hurricane largely characterized by its severe precipitation and large breadth, we compared our simulations to GSMaP satellite-derived surface precipitation. Our results demonstrated agreement in simulating storm size. In addition, the spatial orientation of rainfall (mostly to the north of Irene's eye) was also forecast. We analyze the precipitation flux produced inside of a vortex-following nested grid with GSMaP. The difference between coupled and uncoupled configurations was apparent, with *WRF-Static* producing much more precipitation within the storm than the remaining experiments. The difference between 2- and 3-*Way* configurations was minimal however, indicating that enhanced surface fluxes may have had a minimal impact on storm precipitation flux.

As a result of the intense precipitation, we analyzed its impacts on the ocean salinity. One proposed impact is that the freshening of the upper-ocean column would result in increased salinity stratification, reducing mixing and the impact upper-ocean cooling would have on the TC. The ocean salinity budget was investigated in a detailed manner similar to the heat budget investigation with Hurricane Ivan. Three points were analyzed and at all three points, the impacts of surface salinity via vertical diffusion were weak compared to horizontal advection. The *ANA\_SSFLUX* experiment was applied as well, to examine precipitation impacts on vertical diffusion. Despite the removal of freshwater input into the ocean model, there was minimal impact on the vertical diffusion term of the salinity budget.

In addition, 3 cross-sections of ocean salinity were analyzed at these 3 points along the Irene's track through the SAB. While freshwater input is apparent at all 3 locations, intense mixing quickly erases this signature. The freshwater impact (through advection and diffusion) to the east of the storm center had an impact at one location, completely removing a column of saline water resulting in less horizontal stratification. At the location furthest to the north, there was intense salinity stratification ( $>3$  PSU) through the cross-section. Irene's impact here was to push fresh water from the MAB south, along the shoreline. This was a consequence of the shift from downwelling-favorable to upwelling-favorable winds and had the effect of briefly increasing the horizontal stratification.

A spatial analysis of the surface salinity budget was calculated as Irene was making its first landfall on the North Carolina Outer Banks (12 UTC 27 August). The impact on the surface salinity is apparent as the experiments *ANA\_SSFLUX* and *EMINUSP* had drastically different terms (opposite signs) to the vertical diffusion budget at the surface. This is in contrast to the minimal effect precipitation had through mixing the upper 100m of the water column. However, even at the surface layer, horizontal advection of salinity dominates the salinity budget.

A time series of lagged along-track precipitation flux and surface salinity is analyzed. We utilize a difference between the surface salinity results in the *ANA\_SSFLUX* experiment and the *EMINUSP* experiment in order to discern any input from precipitation while eliminating other dynamic sources of surface salinity adjustment. While tracking the location of the storm, a lag was employed as the greatest impact to surface salinity would occur when the heavy rainbands and eyewall were passing over the location and not the eye.

A strong negative correlation was sought (heavy precipitation decreases surface salinity) over several lag intervals. The greatest anticorrelation ( $r=-0.57$ ) was found at 10 hr. This relatively weak anti-correlation suggests that the passage of heavy precipitation is not a large contributor to changes in surface salinity, but rather salinity advection along the TC's track.

Time series wave comparisons demonstrated skill of the *3-Way* coupled model to predict significant wave heights as Irene impacted the U.S. east coast. Correlation coefficients (ranging from 0.76 to 0.96) and RMSE values (ranging from 2.13 to 0.84) indicated good performance, however several data points were missing in the analysis of three buoys. Overprediction of wave heights was consistent with the westward jog of TC track in the southern portion of the domain, increasing surface forcing and significant wave heights.

## 5 Conclusions and Future Work

TC's are large events that can create an immense amount of damage and devastation, typically focused on the coastal region. The ability to more accurately predict these events can help save lives and reduce their impact. To accomplish this, the research community has identified several areas that can increase our predictive capability. This dissertation provides a broad perspective and discrete examples of one of those actively growing area of research, air-sea coupling to dynamical models. While the track forecasting of TCs has continually improved, intensity forecasting has been much slower to improve. One of the contributing factors to errors in TC intensity prediction is due to lack of coupling to dynamic ocean and wave models. Several approaches have been attempted to reduce this error (through use of parameterizations, 1-D ocean mixed layer models, etc.), but many are not sufficient. Several of these approaches were demonstrate in the literature review section of this thesis. Additional case studies were presented in the following chapters to show the improvement in TC prediction through use of a coupled numerical model. The experimental design in each chapter was created in order to increase the complexity of coupling, to demonstrate the areas where ocean coupling could improve a hindcast/forecast, or where there was minimal impact. In addition to the improvement from forecasting/hindcasting TCs and ETCs that is apparent, the inclusion of ocean and wave coupled models allows analysis into those fields. It is hypothesized that coupled modeling systems will provide improvement to the prediction of hurricane intensity, environmental states of surface waves and sea surface temperature, and atmospheric impact from precipitation distribution. This is demonstrated with 3 different tests of Hurricanes Ivan (2004), Sandy (2012), and Irene (2011).

In a hindcast simulation of Hurricane Ivan, improvement was demonstrated in simulating the intensity of the storm, compared to uncoupled models. Analysis into remotely sensed and *in situ* fields during this hurricane are shown in order to explain the intensity fluctuations during the storm. The impact of the TC on the ocean is then discussed, using prognostic variables to determine the impact Ivan's strong swirling winds had on the ocean. Using the three-dimensional currents available through coupling to a three-dimensional ocean model, a mixed layer heat budget analysis was conducted in order to determine the response of the ocean heat content to various dynamical processes. Through coupling to a wave model, agreement is demonstrated in simulating the wave fields forced by Hurricane Ivan, an extremely intense storm. Finally, an analysis of the entire ocean-atmosphere-wave coupled fields are given immediately prior to landfall.

Using Hurricane and Post-Tropical Storm Sandy (2012), a historic storm, an investigation of the impacts of ocean coupling on simulating extratropical conversion was conducted. Four experiments demonstrated that for this case, minimal change was observed in simulating this storm, in direct contrast to the aforementioned simulations of Hurricane Ivan. All simulations performed well in simulating Sandy's track, intensity and strength for the 36 hours leading up to landfall. Some significant differences in simulated track occur with the addition of simulated wave fields, and an analysis of the bottom roughness is used in order to explain those drastic differences. However, this is an area of ongoing study. Following along with Sandy's track, an examination into multiple environmental variables is conducted in order to explain the extratropical conversion through a coupled ocean-atmosphere approach. SST and significant wave height comparison to *in situ* data for this

storm demonstrated that the coupled hindcast performed well before, during, and after the storm. As in study of Ivan, an analysis of the entire ocean-atmosphere-wave coupled fields are given immediately prior to landfall.

The final case study uses Hurricane Irene's (2011) two impacts along the U.S. east coast for study into the impacts of coupled modeling using forecast fields rather than hindcast. Irene was characterized by its intense precipitation and large size, rather than its intensity. As in previous chapters, a number of experiments are displayed in order to discern the impact of ocean coupling on the TC track, intensity, and strength. As this was a forecast product, these experiments are compared to the large number of ensemble models used to forecast this storm as it was making its trek along the U.S. east coast. Limiting the amount of surface ocean features by filtering was attempted in order to see the importance of simulating the ocean condition in an uncoupled model with high resolution. Large differences were found in the forecast fields in precipitation fields intensity and strength. SST in the coupled configurations varied to a much greater degree than the representation of the sea surface in the uncoupled runs. As in the Ivan chapter, the ocean prognostic fields were used to discern differences in the salinity structure of the ocean as the heavy precipitation moved through. Minimal differences were found in most locations as the fresh water from the storm was rapidly mixed through the water column by heavy winds driving strong currents. The dominant feature in the salinity budget, regardless of location, was advection. This is in large part due to the shift of the Gulf Stream, forced by the intense winds of the TC impacting the nearshore environment. Minimal correlation between high precipitation and change in surface salinity was found. As in previous studies, the wave heights were well-reproduced in

the simulation and an analysis of the entire ocean-atmosphere-wave coupled fields are given immediately prior to Irene's first landfall in North Carolina.

While several things were learned using coupled modeling approaches, many deficiencies were also discovered. There are several areas upon which to continue research in this field. The first is the importance of coupling on the atmospheric boundary layer. As shown through coupling with the wave model, the storm's strength varies considerably. There is minimal data available upon which to draw parameterizations of wave coupling with sea surface roughness and drag coefficients. This is an area of ongoing research and the coupled modeling community would benefit greatly from improved knowledge in this area. Another area of improvement would be inclusion on an ecosystem model to the coupled ocean model. As demonstrated in the literature review, moving TCs have produced large chlorophyll-*a* blooms. Modeling these blooms would help to gain insight into the biological impacts that moving TCs have on the coastal environment, which would have large implications for coastal communities. Another area of research would be examining how a warm/cold core eddy, or sets of eddies effects a moving TC. Several studies already exist, but varying the number, strength, and thickness of these eddies would improve TC prediction. Continuing from this, not only surface observations (which have drastically introduction of remote-sensed platforms) of ocean state variables, but also at depth would greatly improve the ability to predict the ocean and atmosphere. Finally, the last area of ongoing research would be to validate and improve the coupled model in nowcasting/forecasting situations.

## TABLES

**Table 1.1.** Configuration of various coupled models for review and comparison

<b>ID</b>	<b>Reference</b>	<b>Coupled Model</b>	<b>Ocean</b>	<b>Atmosphere</b>	<b>Wave</b>
1	Khain et al. (2000)		7-layer prim.	8-layer prim.	
2	Bender and Ginis (2000)	GFDL	POM	GFDL	
3	Bender et al. (2007)	GFDL-2001	POM	GFDL	
4	Yablonsky and Ginis (2009)	GFDL-2001	POM	GFDL	
5	Lee and Chen (2014)	UMCM	3DPWP	WRF	
6	Chen et al. (2013)	UMCM	3DPWP	MM5	WW3
7	Lee and Chen (2012)	UMCM	3DPWP	MM5	WW3
8	Bao et al. (2000)		POM	MM5	Sfc. Gravity
9	Liu et al. (2008)			WRF	WW3
10	Xie et al. (2010)	CROWN	POM	WRF	WW3
11	Liu et al. (2012b)		POM	WRF	WW3
12	Liu et al. (2010)	CAWOMS	POM	WRF	SWAN
13	Liu et al. (2012a)	CAWOMS	POM	WRF	SWAN
14	Wada et al. (2013)		MRI-Bender	NHM	MRI-III

**Table 2.1.** Design of 5 experiments relating to the level of ocean and wave interaction

<b>Experiment</b>	<b>SST Condition</b>	<b>Ocean Coupling</b>	<b>Wave Coupling</b>
<i>Static SST</i>	RTG SST at initialization, unchanging	None	None
<i>Dynamic SST</i>	RTG SST, updated every 6 hours	None	None
<i>WRF OML</i>	Changing based on WRF OML Model	1-D Ocean	None
<i>2-Way</i>	Changing based on ROMS	Mixed Layer	None
<i>3-Way</i>	Changing based on ROMS	ROMS Model	None
		ROMS Model	SWAN Model

**Table 2.2.** Intensity comparisons against verification for 5 experiments over 108 h hindcast. Includes Root Mean Squared Error (RMSE), and correlation coefficient (r) for Intensity (in hPa)

	<b>Intensity</b>	
	<b>RMSE</b>	<b>r</b>
<i>Static SST</i>	20.82	0.85
<i>Dynamic SST</i>	19.16	0.86
<i>WRF OML</i>	15.20	0.88
<i>2-Way</i>	9.66	0.94
<i>3-Way</i>	10.95	0.92

**Table 3.1.** Design of 4 experiments relating to the level of ocean and wave interaction

<b>Experiment</b>	<b>SST Condition</b>	<b>Ocean Coupling</b>	<b>Wave Coupling</b>
<i>WRF-Static</i>	RTG SST at initialization, unchanging	None	None
<i>WRF OML</i>	Changing based on WRF OML Model	1-D Ocean Mixed Layer	None
<i>2-Way</i>	Changing based on ROMS	ROMS Model	None
<i>3-Way</i>	Changing based on ROMS	ROMS Model	SWAN Model

**Table 3.2.** Intensity (hPa) and Strength ( $\text{ms}^{-1}$ ) comparisons against verification for 4 experiments over first 60 hours of 132 hour hindcast as Sandy dissipated shortly after landfall. Includes Root Mean Squared Error (RMSE), and correlation coefficient (r).

	<b>Intensity</b>		<b>Strength</b>	
	<b>RMSE (hPa)</b>	<b>r</b>	<b>RMSE (<math>\text{ms}^{-1}</math>)</b>	<b>r</b>
<i>WRF-Static</i>	8.0	0.92	6.3	0.94
<i>WRF-OML</i>	9.0	0.91	7.2	0.90
<i>2-Way</i>	7.5	0.92	7.5	0.90
<i>3-Way</i>	6.9	0.94	9.6	0.80

**Table 3.3.** Significance testing (Student’s T-test) of experiments. P-value and Confidence Interval (CI) demonstrated for differences among the 4 model experiments.

<b>SLP (hPa)</b>	<b>Experiments</b>	<b>P-Value</b>	<b>CI</b>	
	Static-OML	<0.1%	0.9077	1.8451
	Static-2way	<0.1%	-0.6808	-0.4195
	Static-3way	<0.1%	-1.4502	-0.7564
	OML-2way	<0.1%	-2.3612	-1.4919
	OML-3way	<0.1%	-2.8926	-2.0667
	2way-3way	<0.1%	-2.8926	-2.0667
<b>Wind (ms-1)</b>	<b>Experiments</b>	<b>P-Value</b>	<b>CI</b>	
	Static-OML	1.08%	-0.8093	-0.11
	<b>Static-2way</b>	<b>10.58%</b>	<b>-0.476</b>	<b>0.0468</b>
	Static-3way	<0.1%	-3.1587	-1.9075
	<b>OML-2way</b>	<b>9.37%</b>	<b>-0.0427</b>	<b>0.5329</b>
	OML-3way	<0.1%	-2.7133	-1.4336
	2way-3way	<0.1%	-2.7133	-1.4336

**Table 4.1.** Design of 5 experiments relating to the level of ocean and wave interaction

<b>Experiment</b>	<b>SST Condition</b>	<b>Ocean Coupling</b>	<b>Wave Coupling</b>
<i>WRF-Static</i>	RTG SST at initialization, unchanging	None	None
<i>WRF-Dynamic</i>	RTG SST, updated every 6 hours	None	None
<i>WRF-Filter</i>	RTG SST, updated every 6 hours with a 1-2-1 filter applied 100 times	None	None
<i>2-Way</i>	Changing based on ROMS	ROMS Model	None
<i>3-Way</i>	Changing based on ROMS	ROMS Model	SWAN Model

**Table 4.2.** Intensity (hPa) and Strength ( $\text{ms}^{-1}$ ) comparisons against verification for 5 experiments over 84 h hindcast. Includes Root Mean Squared Error (RMSE), and correlation coefficient (r).

	<b>Intensity</b>		<b>Strength</b>	
	<b>RMSE (hPa)</b>	<b>r</b>	<b>RMSE (<math>\text{ms}^{-1}</math>)</b>	<b>r</b>
<i>WRF-Static</i>	11.39	0.57	4.36	0.90
<i>WRF-Filter</i>	14.52	0.66	4.37	0.96
<i>WRF-Dynamic</i>	14.65	0.58	4.70	0.95
<i>2-Way</i>	13.32	0.64	4.35	0.95
<i>3-Way</i>	12.42	0.58	4.60	0.86

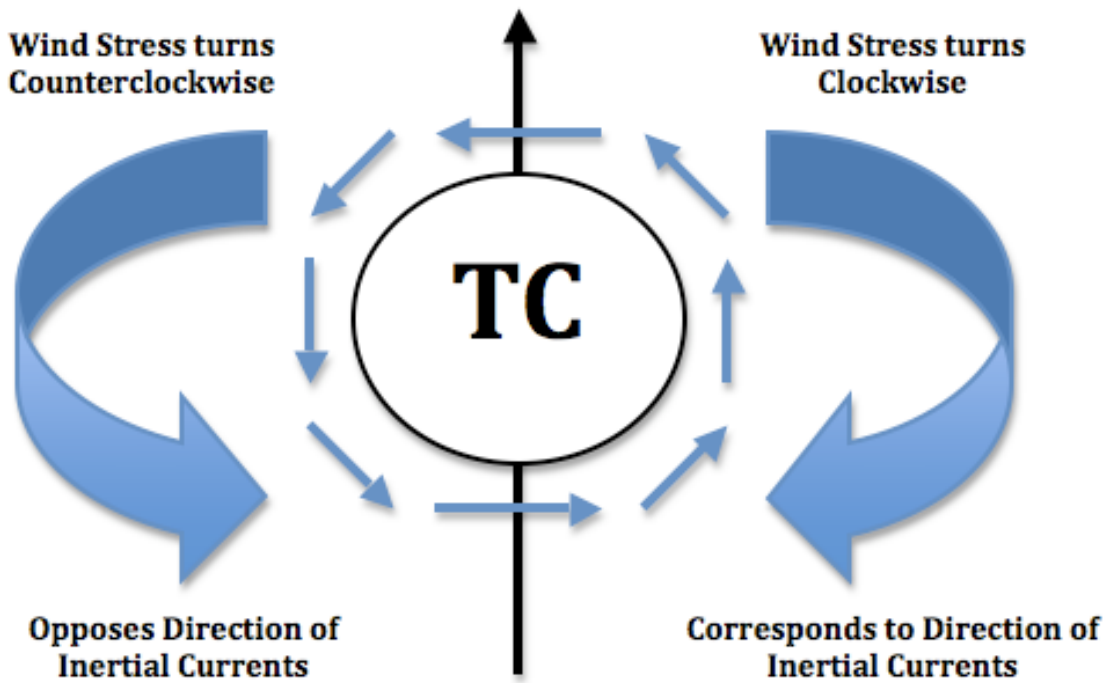
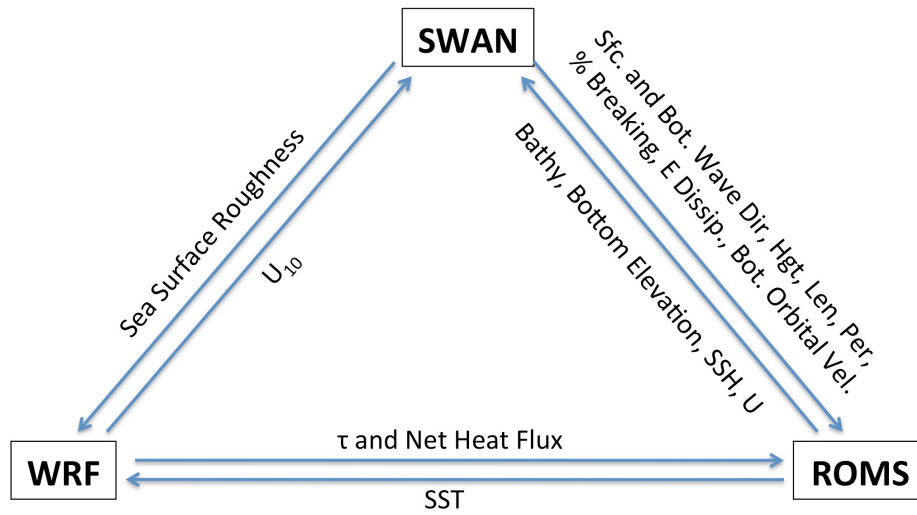


**Figure 1.1.** Schematic of wind stress vector rotation with TC translation (for northern hemisphere)



WRF->ROMS: Surface Stress and Net Heat Fluxes (computed in ROMS from flux components of Latent and Sensible Heat Fluxes, Shortwave and Longwave Radiation)  
 ROMS->WRF: Sea Surface Temperature  
 SWAN-> ROMS: Surface and Bottom Wave Direction, Height, Length, Period, Percent Breaking, Energy Dissipation, Bottom Orbital Velocity  
 ROMS->SWAN: Bathymetry, Bottom Elevation, Sea Surface Height, Depth Averaged Currents  
 SWAN->WRF: Sea Surface Roughness (computed in WRF from Significant Wave Height, Length, Period)  
 WRF->SWAN: 10m Winds

**Figure 2.1.** Diagram of 3-Way coupled model as implemented in the COAWST model for Hurricane Ivan experiments

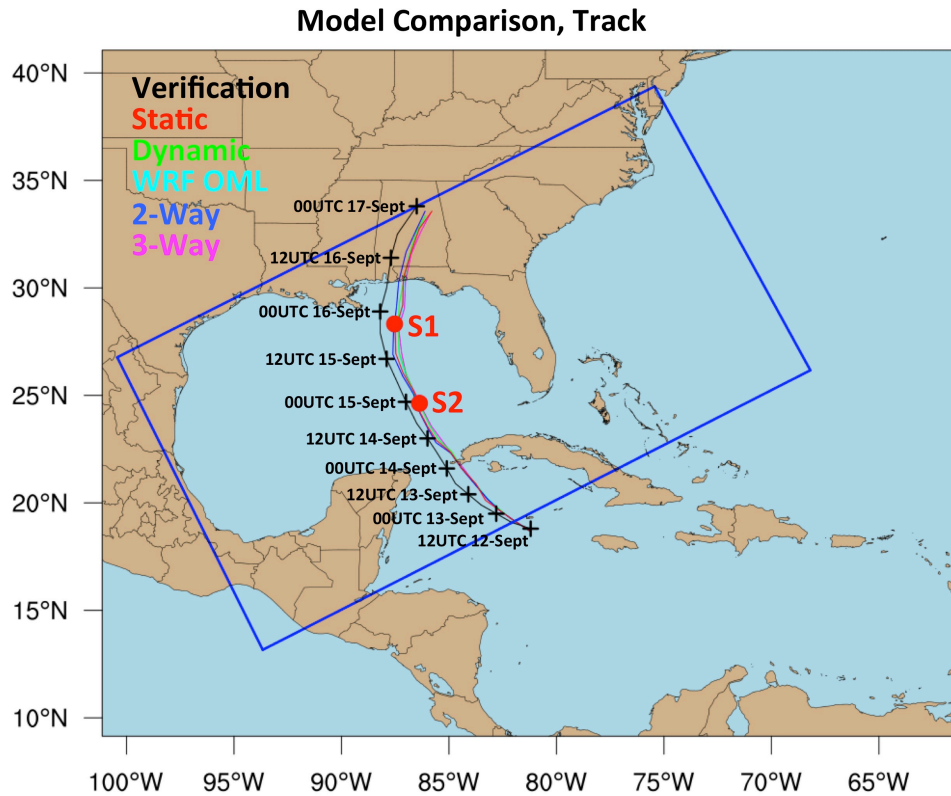


**Figure 2.2.** Comparison of forecast track, 5 experiments: *Static SST* (red), *Dynamic SST* (green), *WRF OML* (cyan), *2-Way* (blue), *3-Way* (magenta). NHC best track verification (black). Also shown are the location of onshore and offshore grid points (S1, S2) used for analysis in Figs. 2.7-2.10

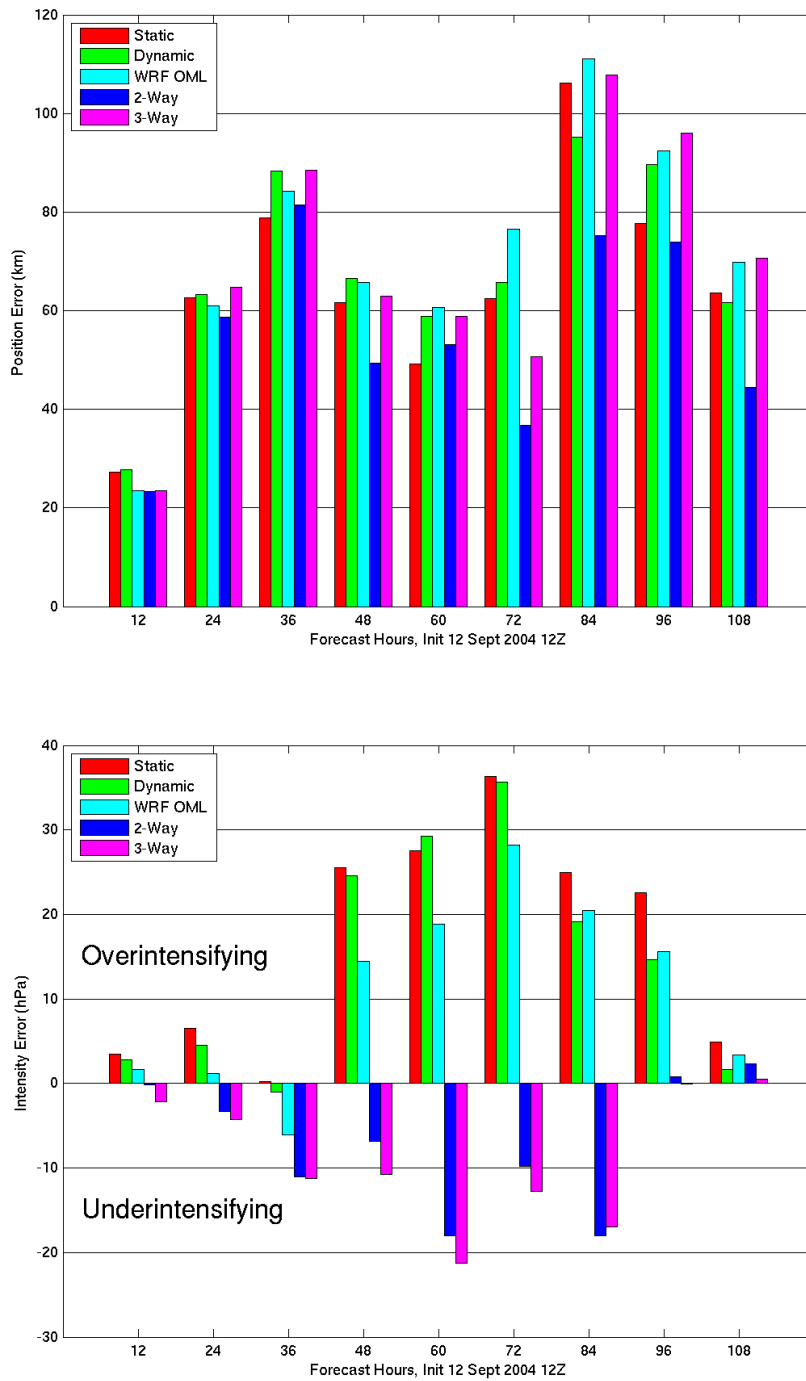


**Figure 2.3.** Simulated TC position (km) and intensity (hPa) errors from initialization (12 UTC 12 September 2004) through termination (00 UTC 17 September 2004), 5 experiments: *Static SST* (red), *Dynamic SST* (green), *WRF OML* (cyan), *2-Way* (blue), *3-Way* (magenta)

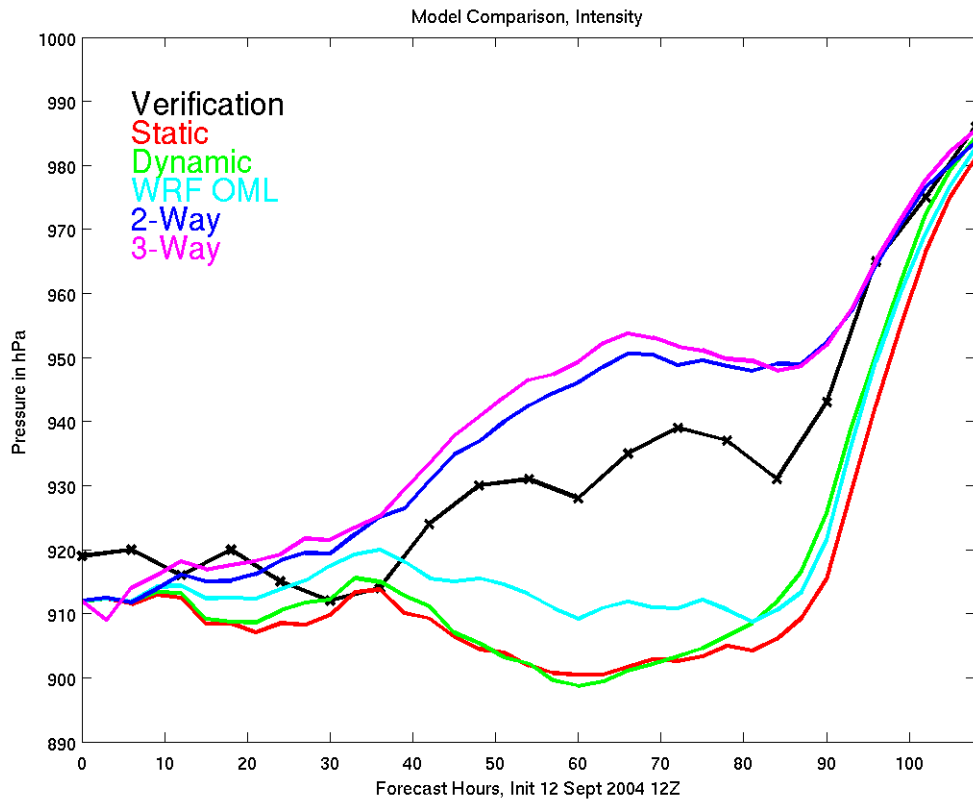


**Figure 2.4.** Simulated TC intensity from initialization (12 UTC 12 September 2004) through termination (00 UTC 17 September 2004), 5 experiments: *Static SST* (red), *Dynamic SST* (green), *WRF OML* (cyan), *2-Way* (blue), *3-Way* (magenta). NHC best track verification (black)

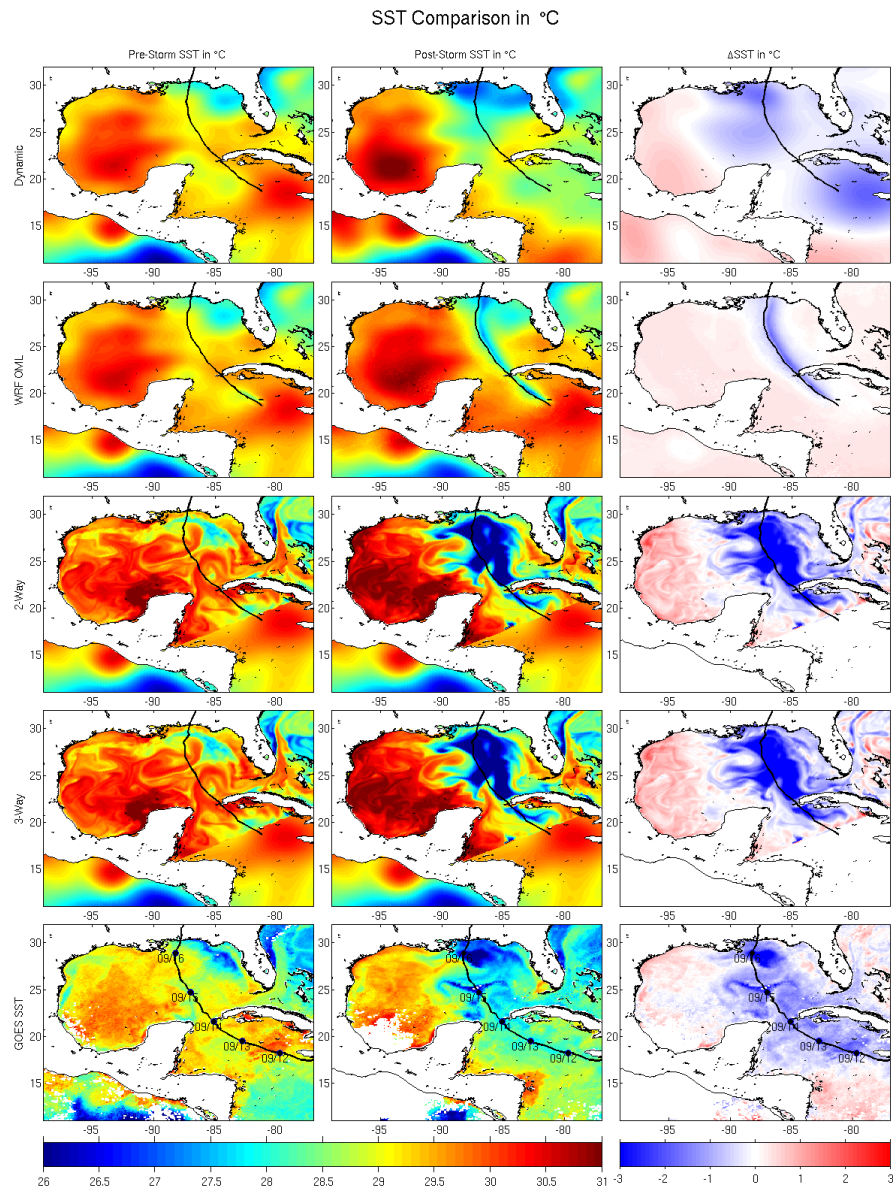


**Figure 2.5.** Coupled SST comparisons for various experimental cases: *Dynamic SST* based on the Gemmill et al. (2007) SST analysis (first row). *WRF OML* based on Pollard et al. (1973) and integrated into WRF by Davis et al. (2008; second row). *2-Way*, Atmosphere-Ocean model coupling (third row). *3-Way*, Atmosphere-Ocean-Wave model coupling (fourth row). GOES SST data obtained from the JPL Physical Oceanography Distributed Active Archive Center (PODAAC; fifth row). Pre-Storm Averaged model SST (top 4 rows, left column). Post-Storm Averaged model SST (top 4 rows, middle column). Pre-Storm averaged GOES SST (bottom row, left column). Post-Storm averaged GOES SST (*bottom row, middle column*). Change in SST (right column)

SST (in °C) Time Series (Valid 12-Sept-04 12Z through 17-Sept-04 00Z)

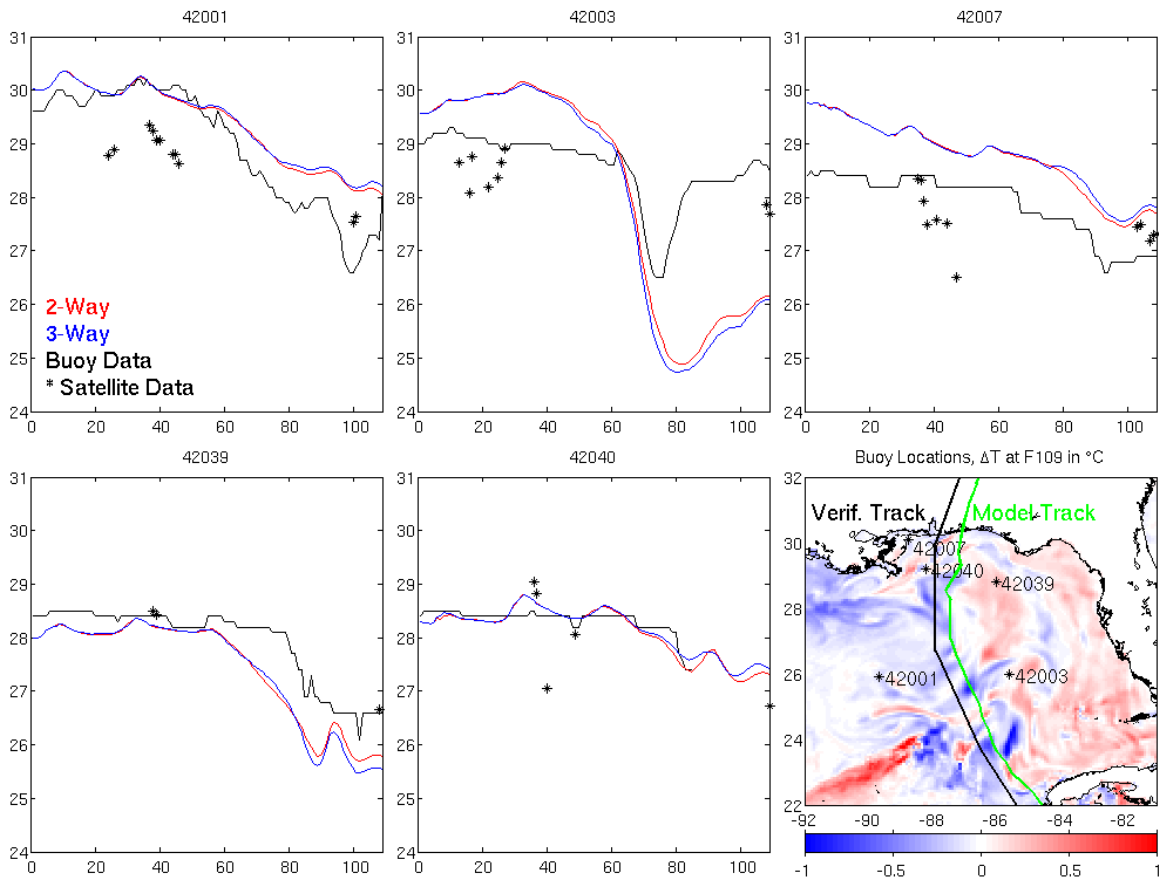


**Figure 2.6.** SST time series at 5 buoys situated inside of the Gulf of Mexico, showing *2-Way* (red line) and *3-Way* (blue line) SST, satellite derived SST (black asterisks) and in-situ SST (black line). Spatial difference in SST between *2-Way* and *3-Way* cases at conclusion of model run, along with location of buoys and *3-Way* simulated TC track (bottom right panel)

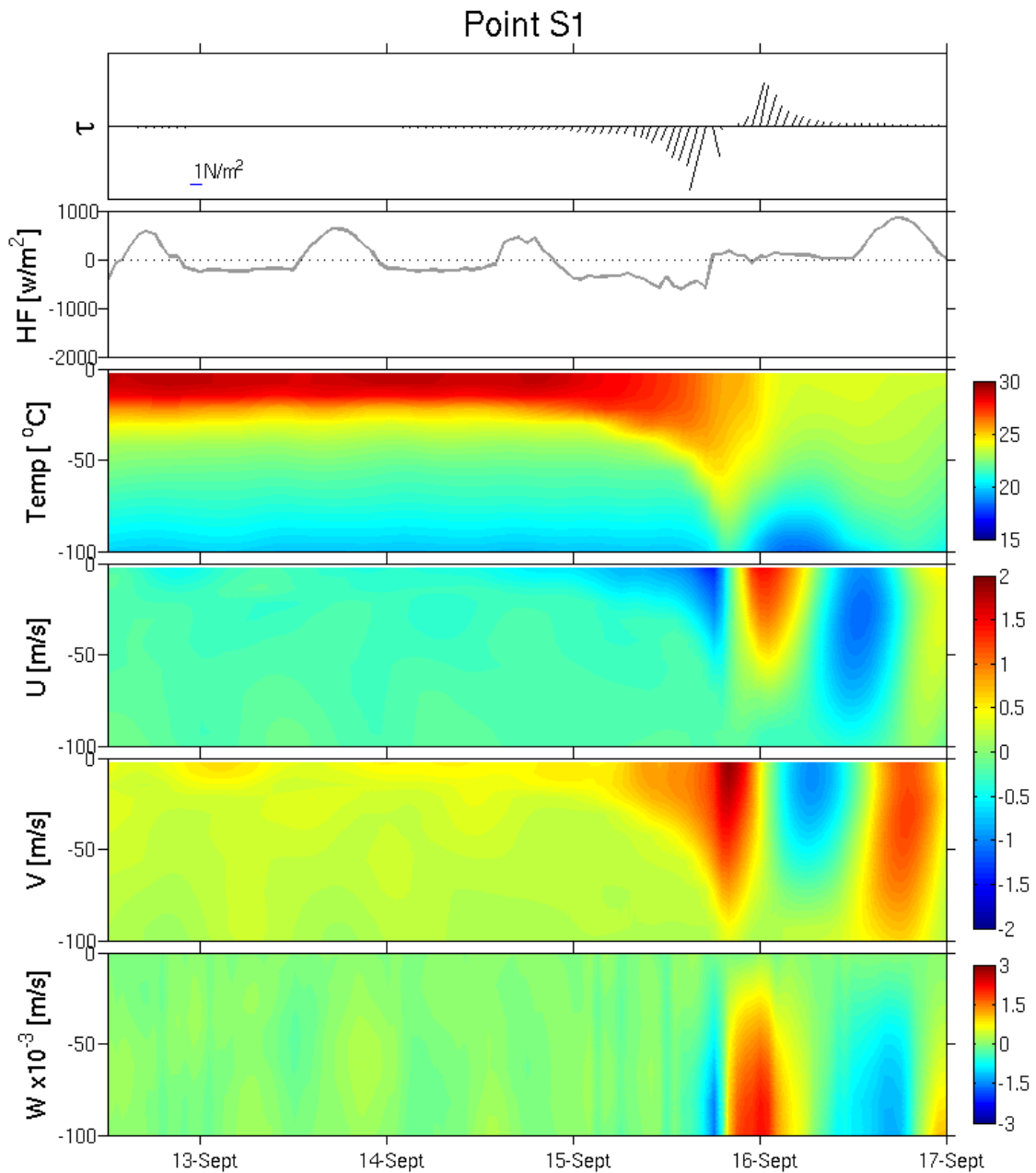


**Figure 2.7** Ocean model (*2-Way*) analysis at point S1 in Figure 2.2 from initialization (12 UTC 12 September 2004) through termination (00 UTC 17 September 2004). Wind stress ( $\tau$ ) in  $\text{Nm}^{-2}$  (first panel), heat flux (HF) in  $\text{Wm}^{-2}$  (second panel), temperature from surface through 100 m depth in  $^{\circ}\text{C}$  (third panel), U velocity from surface through 100 m depth in  $\text{ms}^{-1}$  (fourth panel), V velocity from surface through 100 m depth in  $\text{ms}^{-1}$  (fifth panel), W velocity from surface through 100 m depth in  $\text{ms}^{-1}$  (bottom panel)

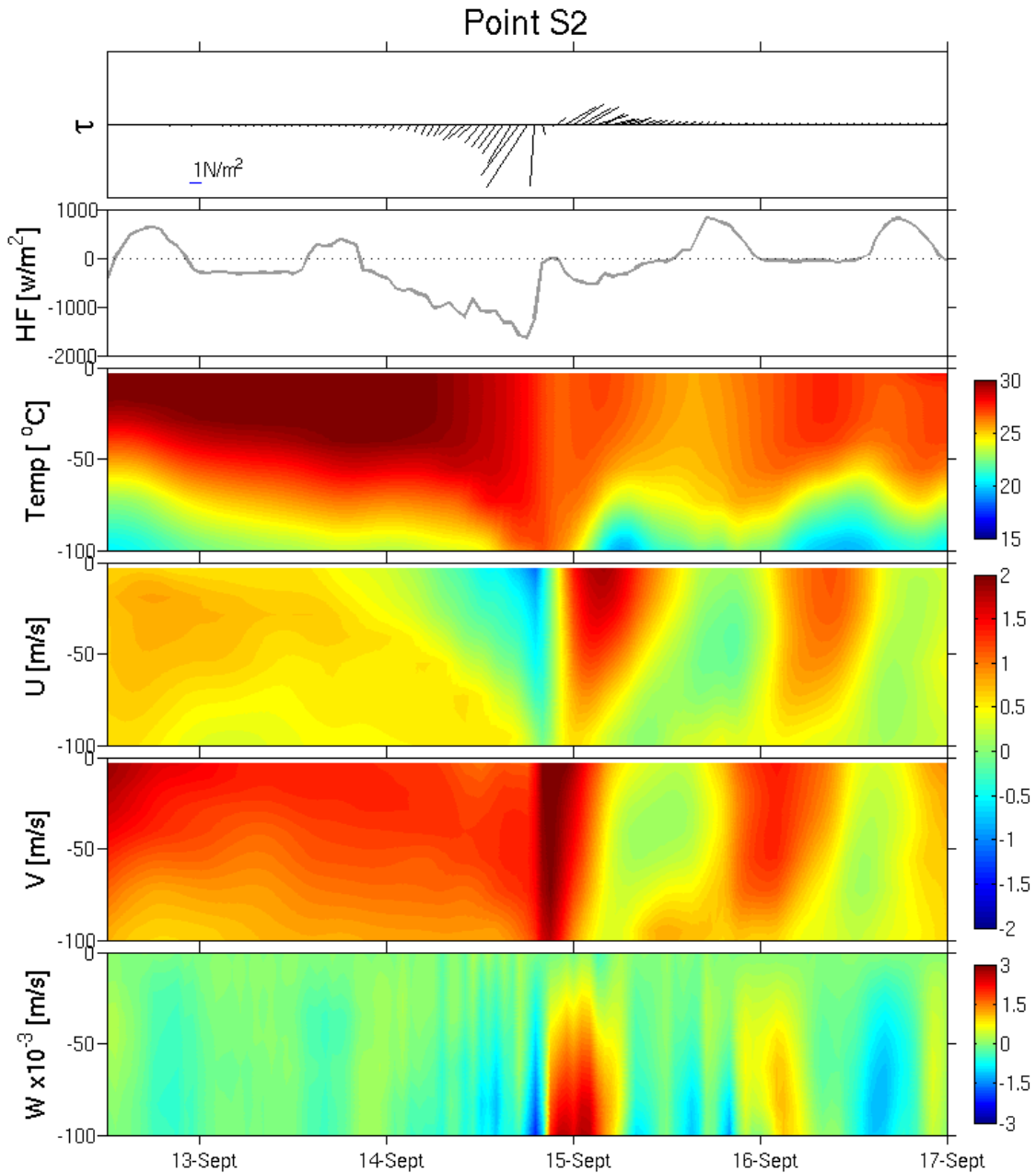


**Figure 2.8** Ocean model (*2-Way*) analysis at point S2 in Figure 2.2 from initialization (12 UTC 12 September 2004) through termination (00 UTC 17 September 2004). Wind stress ( $\tau$ ) in  $\text{Nm}^{-2}$  (first panel), heat flux (HF) in  $\text{Wm}^{-2}$  (second panel), temperature from surface through 100 m depth in  $^{\circ}\text{C}$  (third panel), U velocity from surface through 100 m depth in  $\text{ms}^{-1}$  (fourth panel), V velocity from surface through 100 m depth in  $\text{ms}^{-1}$  (fifth panel), W velocity from surface through 100 m depth in  $\text{ms}^{-1}$  (bottom panel)

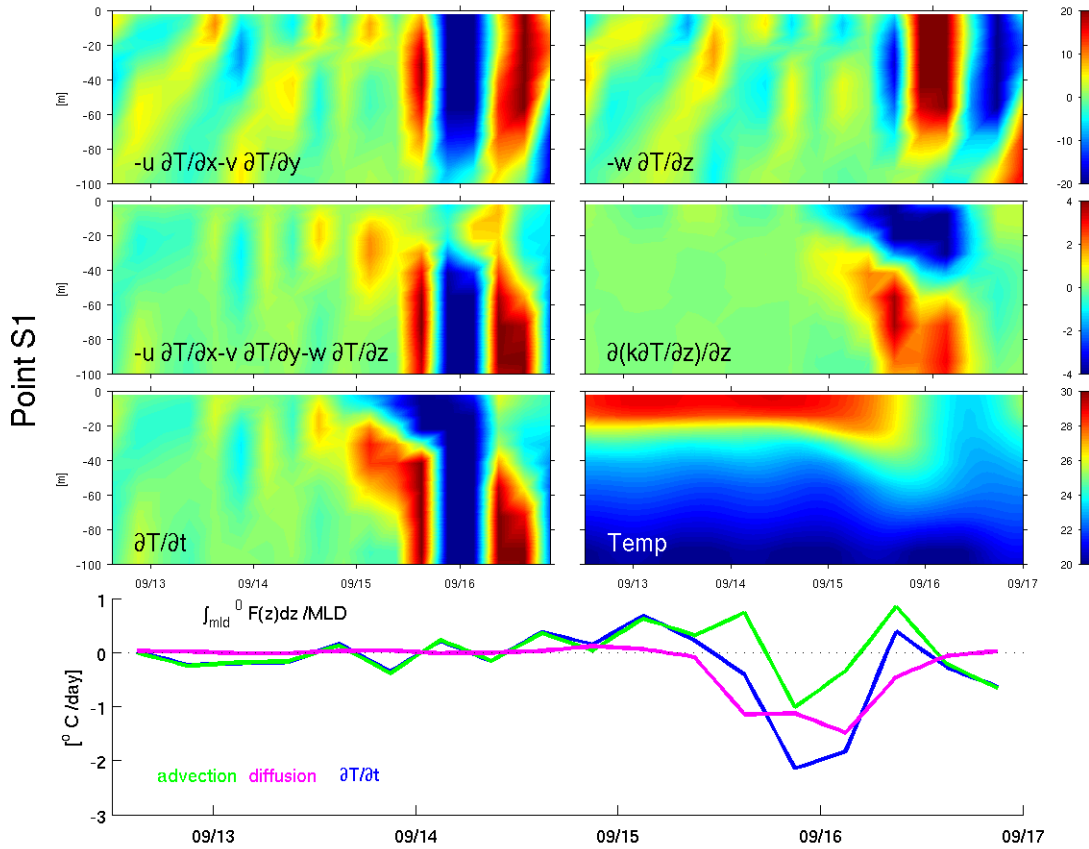


**Figure 2.9.** Ocean model (2-Way) analysis of heat budget at point S1 in Figure 2.2 from initialization (12 UTC 12 September 2004) through termination (00 UTC 17 September 2004). Horizontal advection term in °C/day (upper-left), vertical advection term in °C/day (upper-right), total advection term in °C/day (middle-left), vertical diffusion term in °C/day (middle-right), total local rate of change term in °C/day (lower-left), temperature in °C (lower-right), comparison of contributions of advection and diffusion to local change in temperature integrated through 100 m (bottom panel)

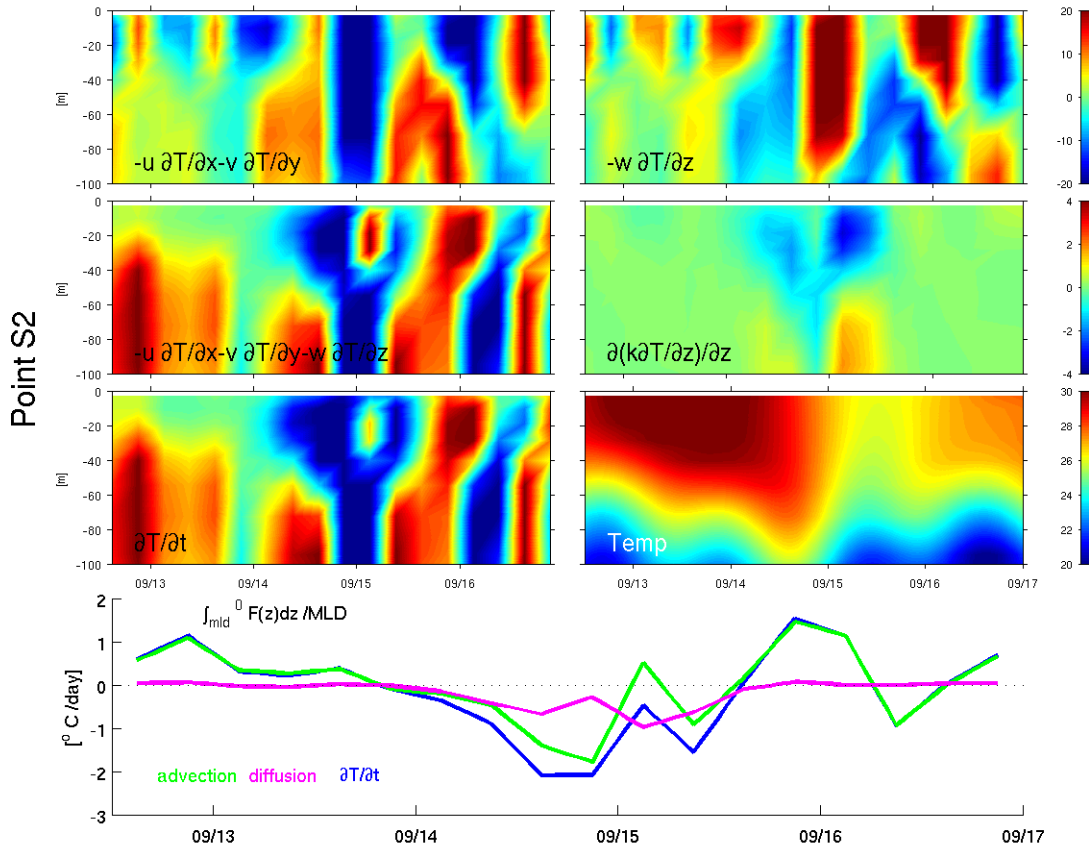


**Figure 2.10** Ocean model (2-Way) analysis of heat budget at point S2 in Figure 2.2 from initialization (12 UTC 12 September 2004) through termination (00 UTC 17 September 2004). Horizontal advection term in  $^{\circ}\text{C}/\text{day}$  (upper-left), vertical advection term in  $^{\circ}\text{C}/\text{day}$  (upper-right), total advection term in  $^{\circ}\text{C}/\text{day}$  (middle-left), vertical diffusion term in  $^{\circ}\text{C}/\text{day}$  (middle-right), total local rate of change term in  $^{\circ}\text{C}/\text{day}$  (lower-left), temperature in  $^{\circ}\text{C}$  (lower-right), comparison of contributions of advection and diffusion to local change in temperature integrated through 100 m (bottom panel)

Wave Height (in m) Time Series (Valid 12-Sept-04 12Z through 17-Sept-04 00Z)

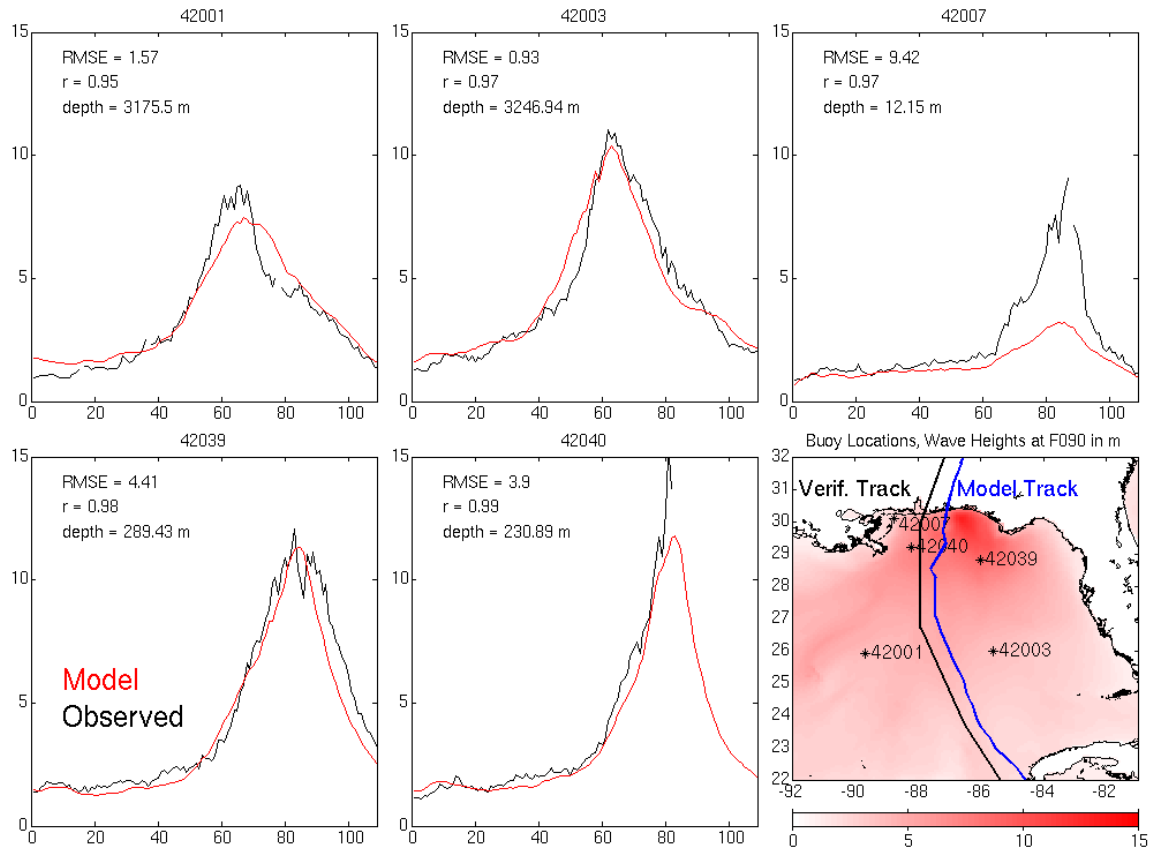


**Figure 2.11.** 3-Way model wave comparison from initialization (12 UTC 12 September 2004) through termination (00 UTC 17 September 2004). Observed (black) and modeled (red) significant wave heights at 5 buoy locations: 42001 (upper left), 42003 (upper middle), 42007 (upper right), 42039 (lower left), 42040 (lower middle). Inset (lower right) shows locations of buoys, simulated tracks, and wave heights at F090 (shaded). Some observations were not available due to extreme waves (e.g. buoy 42040 was torn from its mooring). For each comparison, the correlation coefficient and rms error between observed and simulated significant wave heights are given, along with the water depth information of each station

Forecast Valid: 16-Sep-2004 07:00:00

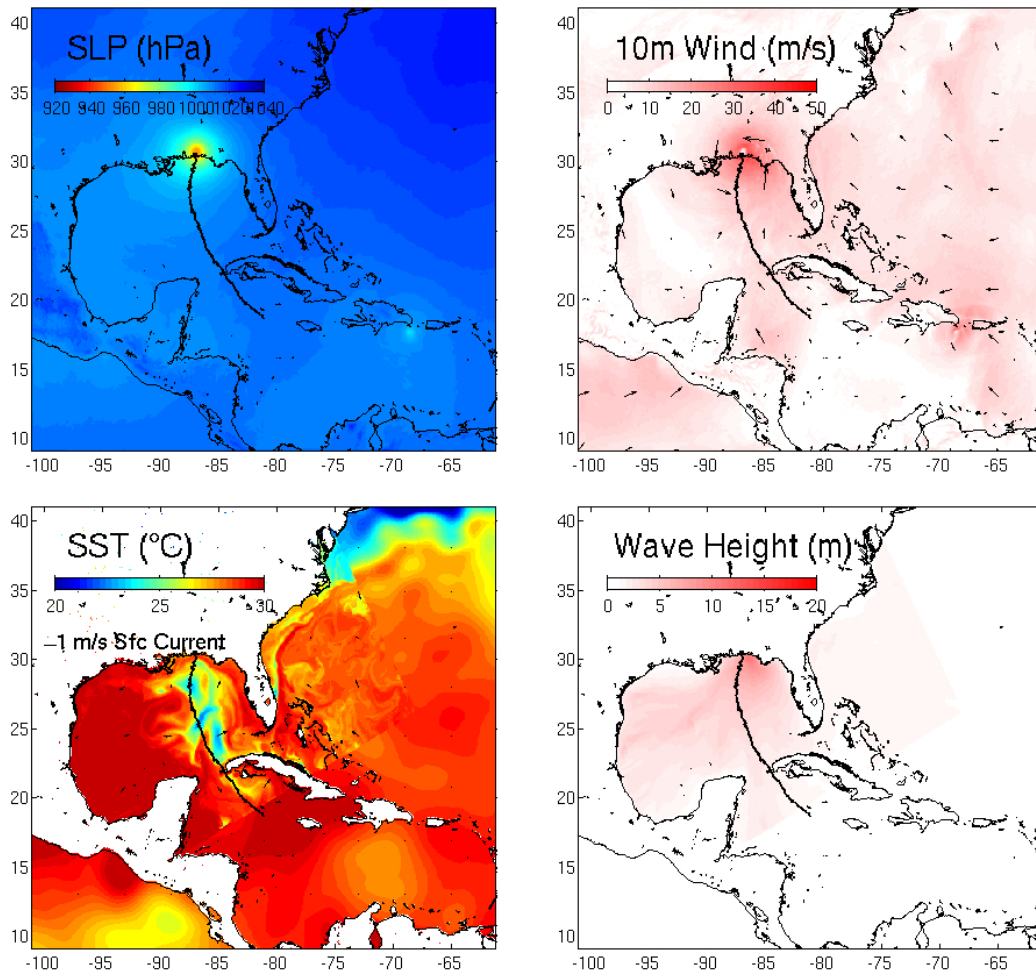
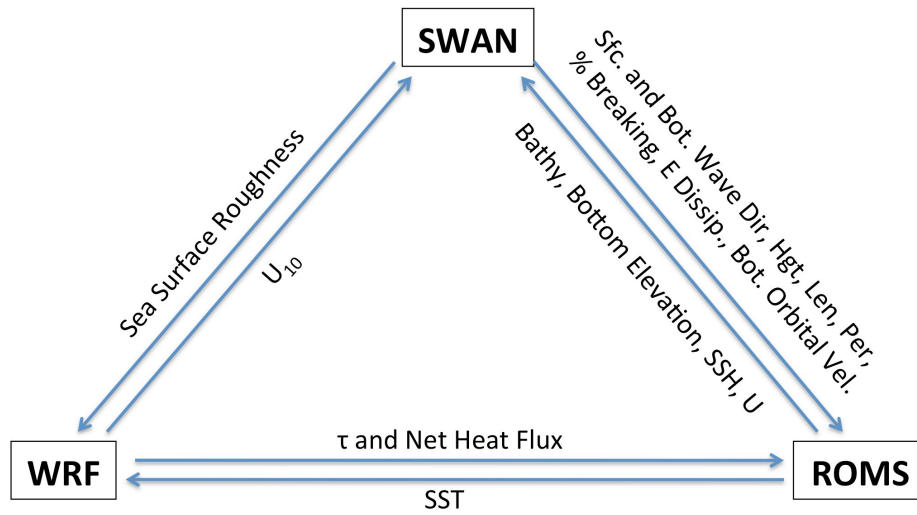


**Figure 2.12.** 4-panel plot of the 3-Way experiment demonstrating the atmosphere, ocean, and wave environments at the time of simulated landfall in Alabama (07 UTC 16 September 2004). The atmospheric environment is represented as quantities of SLP (upper left, shaded) and wind (upper right, shaded with vector arrows). The ocean environment is represented by SST (lower left, shaded) and surface current (lower left, vector arrows). The wave environment is represented by significant wave height (lower right, shaded)



WRF->ROMS: Surface Stress and Net Heat Fluxes (computed in ROMS from flux components of Latent and Sensible Heat Fluxes, Shortwave and Longwave Radiation)  
 ROMS->WRF: Sea Surface Temperature  
 SWAN-> ROMS: Surface and Bottom Wave Direction, Height, Length, Period, Percent Breaking, Energy Dissipation, Bottom Orbital Velocity  
 ROMS->SWAN: Bathymetry, Bottom Elevation, Sea Surface Height, Depth Averaged Currents  
 SWAN->WRF: Sea Surface Roughness (computed in WRF from Significant Wave Height, Length, Period)  
 WRF->SWAN: 10m Winds

**Figure 3.1.** Diagram of 3-Way coupled model as implemented in the COAWST model for Superstorm Sandy experiments

Forecast Valid: 29-Oct-2012 22Z

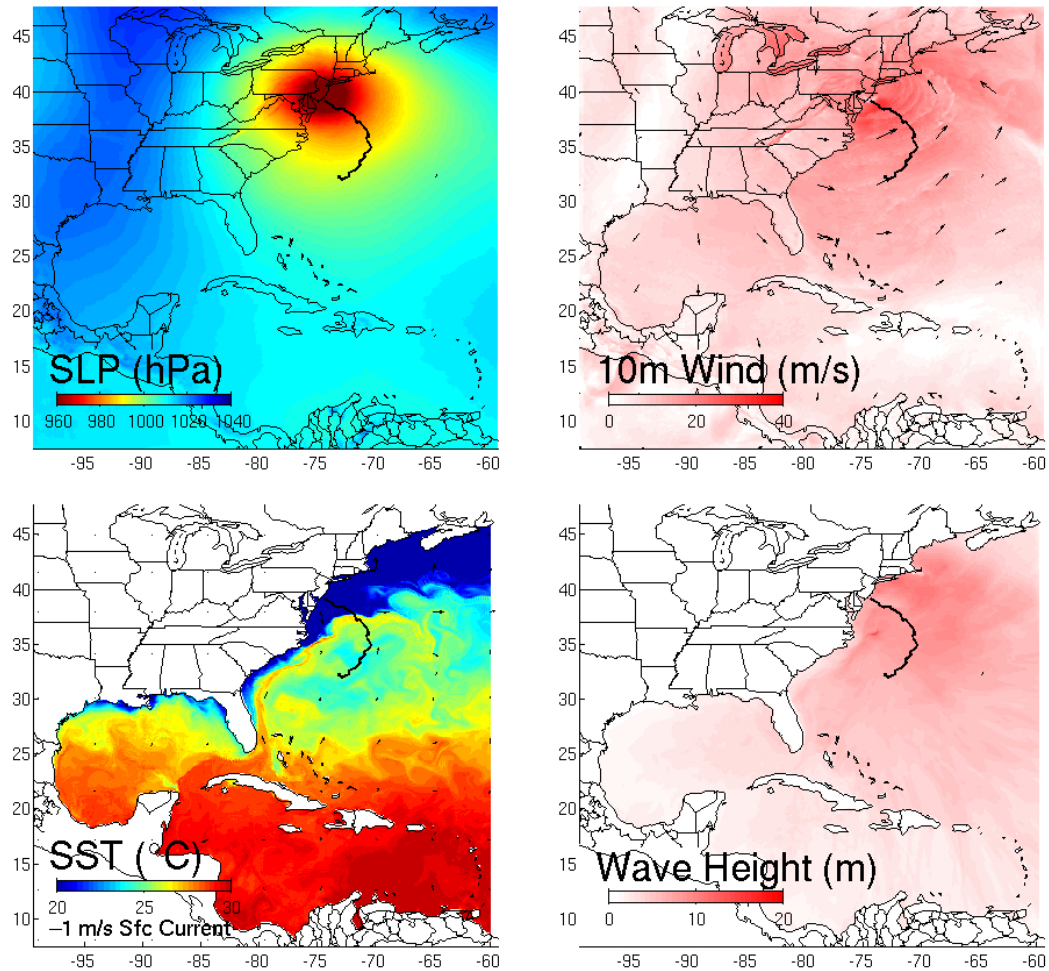


**Figure 3.2.** 4-panel plot of the *3-Way* experiment demonstrating the atmosphere, ocean, and wave environments at the time of simulated landfall in New Jersey (22 UTC 29 October 2012). The atmospheric environment is represented as quantities of SLP (upper left, shaded) and wind (upper right, shaded with vector arrows). The ocean environment is represented by SST (lower left, shaded) and surface current (lower left, vector arrows). The wave environment is represented by significant wave height (lower right, shaded)

# Hurricane Sandy Track

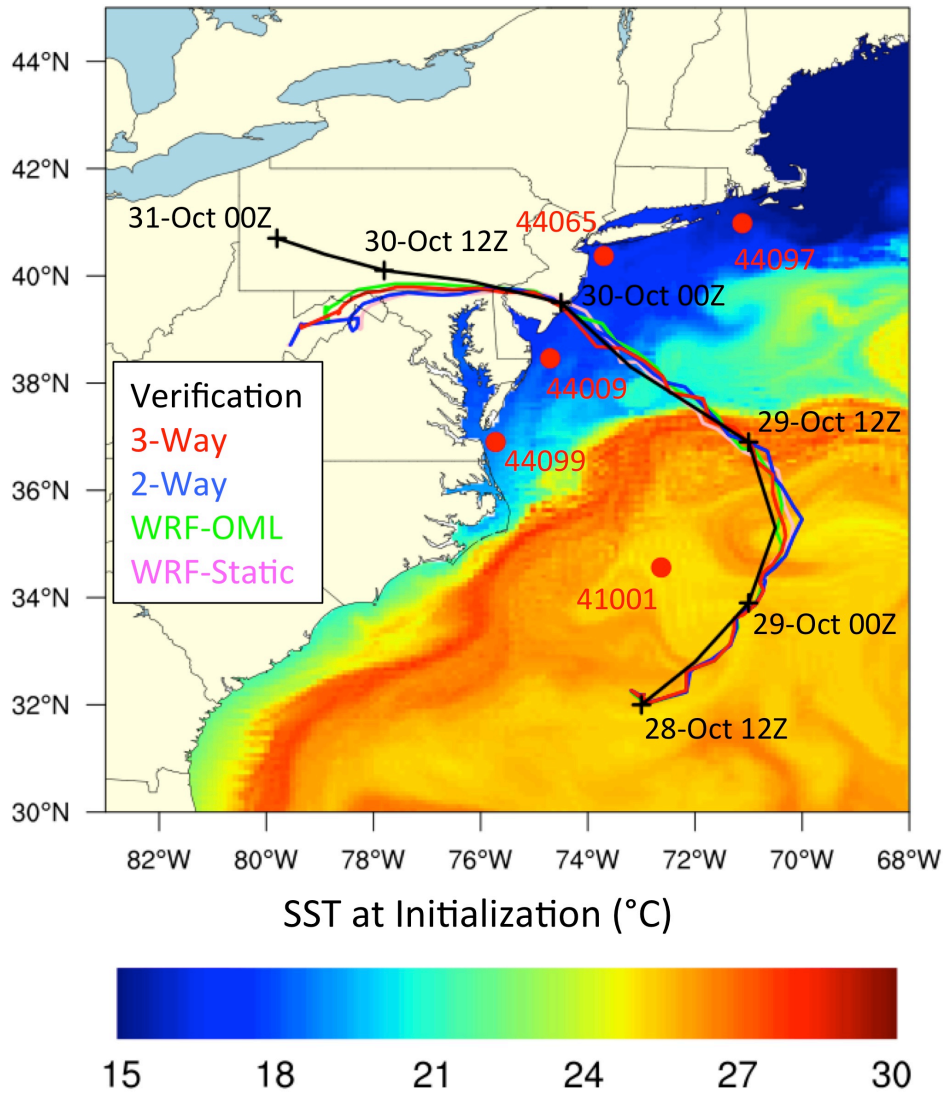


**Figure 3.3.** Simulated track comparison of 4 experiments: *WRF-Static* (magenta), *WRF-OML* (green), *2-Way* (blue), *3-Way* (red). The NHC Best Track product is used for verification (black). SST at initialization from the *3-Way* case is shaded. Buoys for *in situ* comparison in Figures 3.8 and 3.9 are included

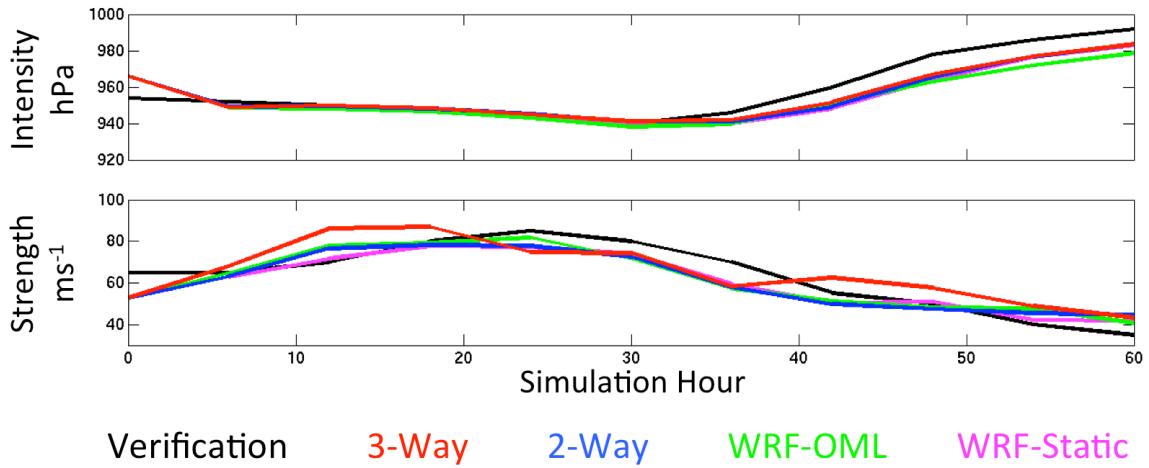


**Figure 3.4.** Simulated comparison of intensity (hPa) and strength ( $\text{ms}^{-1}$ ) of 4 experiments: *WRF-Static* (magenta), *WRF-OML* (green), *2-Way* (blue), *3-Way* (red). The NHC Best Track product is used for verification (black). First 60 hours of 132 hour hindcast are shown as Sandy dissipated shortly after landfall

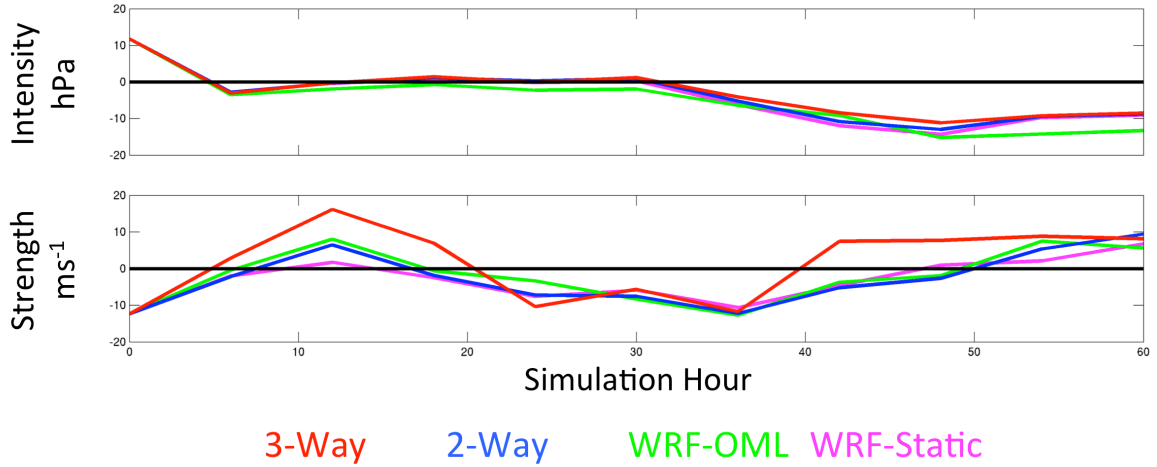


**Figure 3.5.** Simulated comparison of intensity (hPa) and strength ( $\text{ms}^{-1}$ ) residuals against verification of 4 experiments: *WRF-Static* (magenta), *WRF-OML* (green), *2-Way* (blue), *3-Way* (red). First 60 hours of 132 hour hindcast are shown as Sandy dissipated shortly after landfall. Positive (negative) indicates under- (over-) intensification/strengthening

Bottom Stress Comparison, Simulation Hour: 12

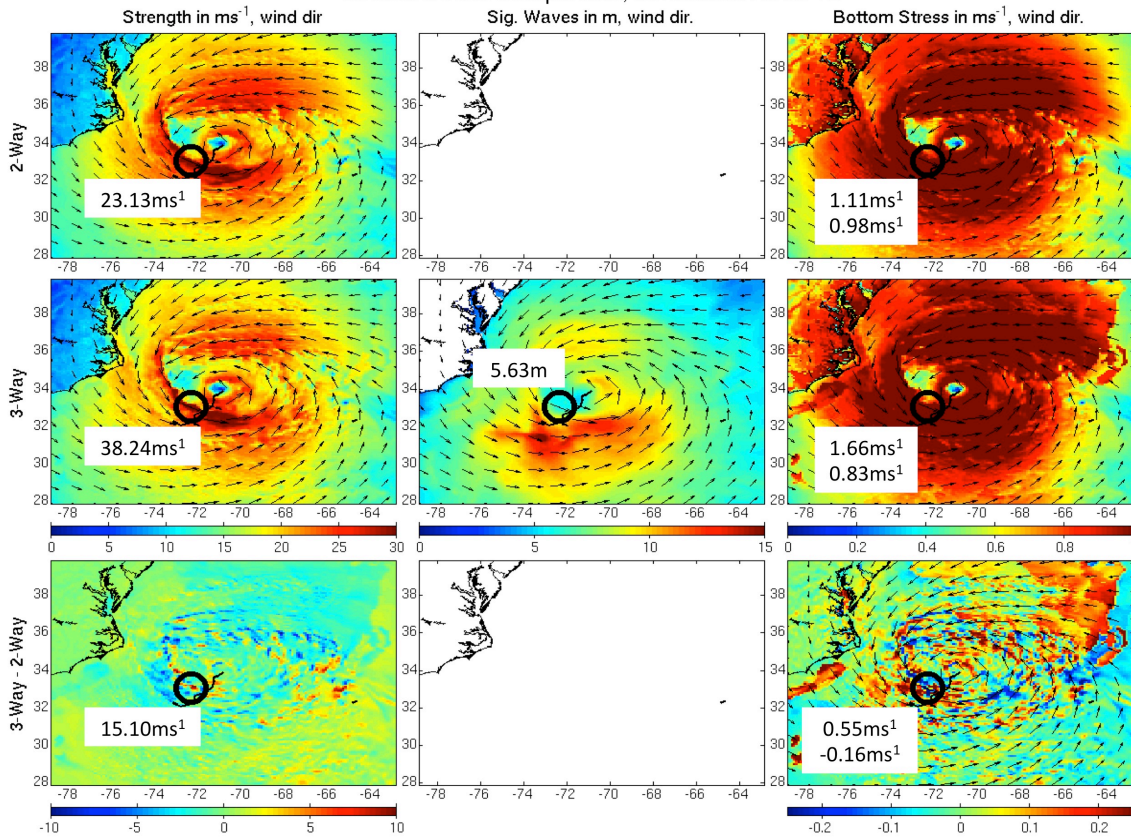


**Figure 3.6.** Analysis of bottom stress calculations (right column) based on wind speed ( $\text{ms}^{-1}$ , left column), wave height (m, middle column), and bottom stress ( $\text{ms}^{-1}$ , right column) at simulation hour 12 (00 UTC 29 October). 2-Way experiment (top row), 3-Way experiment (middle row), difference fields (bottom row)

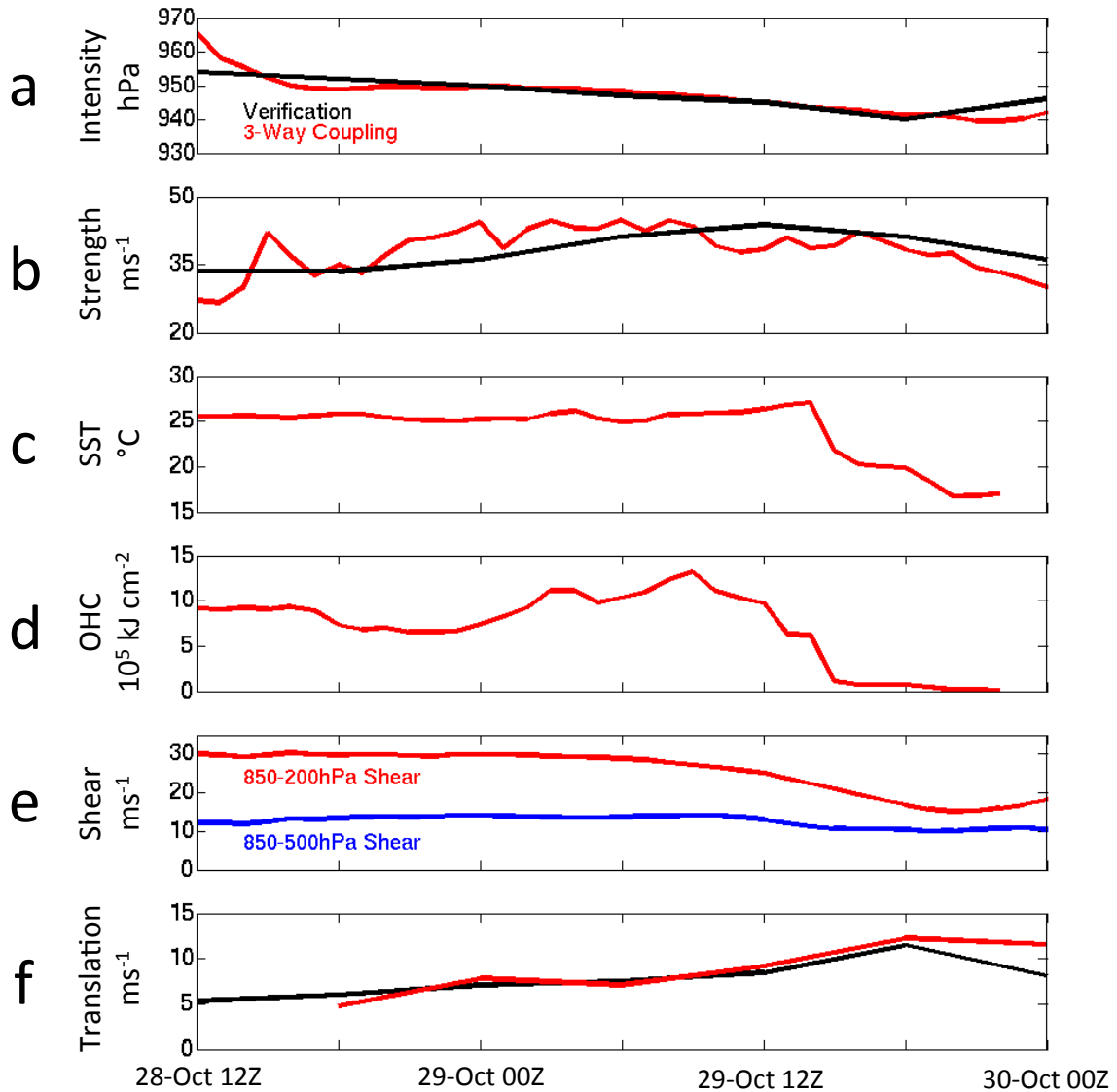


**Figure 3.7.** Environmental conditions prior to Sandy’s landfall (12 UTC 28 October through approximately 00 UTC 30 October). Figure includes: (a) simulated intensity (minimum SLP, hPa) every 3 h, (b) simulated strength (maximum 10 m wind,  $\text{ms}^{-1}$ ) every 3 h, (c) hourly SST ( $^{\circ}\text{C}$ ), (d) hourly ocean heat content (OHC,  $10^5 \text{ kJcm}^{-2}$ ), (e) hourly vertical shear ( $\text{ms}^{-1}$ ) calculated between 850/200 hPa (red) and 850/500 hPa (blue), and (f) translation speed ( $\text{ms}^{-1}$ ) evaluated every 6 h. The *3-Way* case was analyzed with NHC best track Verification (black) every 6 h where available (a, b, f)

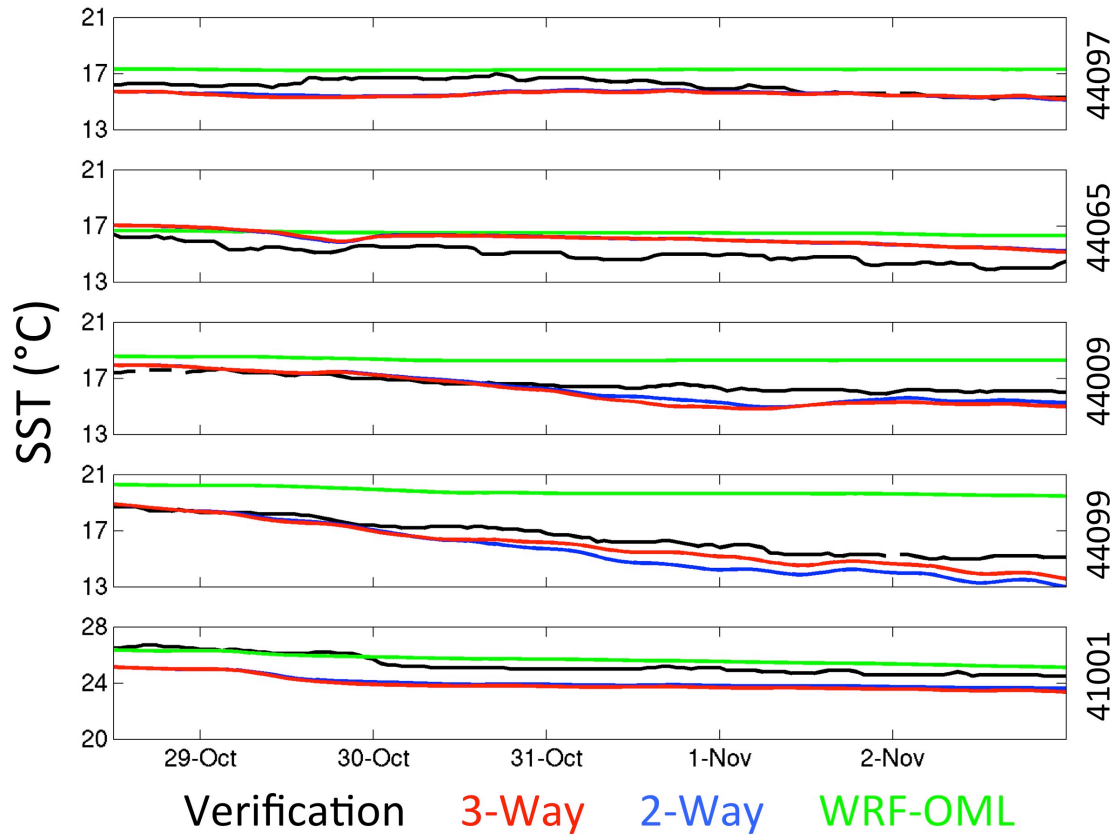


**Figure 3.8.** Simulated SST comparisons to *in situ* buoy data collected at 5 locations along the U.S. east coast demonstrated in Figure 3.3. Verification along with 3 experiments are shown throughout the entire model simulation (132 hr). SST in the *WRF-Static* case is not shown as it is demonstrated by the initial *WRF-OML* SST across the entire time series. Remaining experiments are shown, 4 experiments: *WRF-OML* (green), *2-Way* (blue), *3-Way* (red)

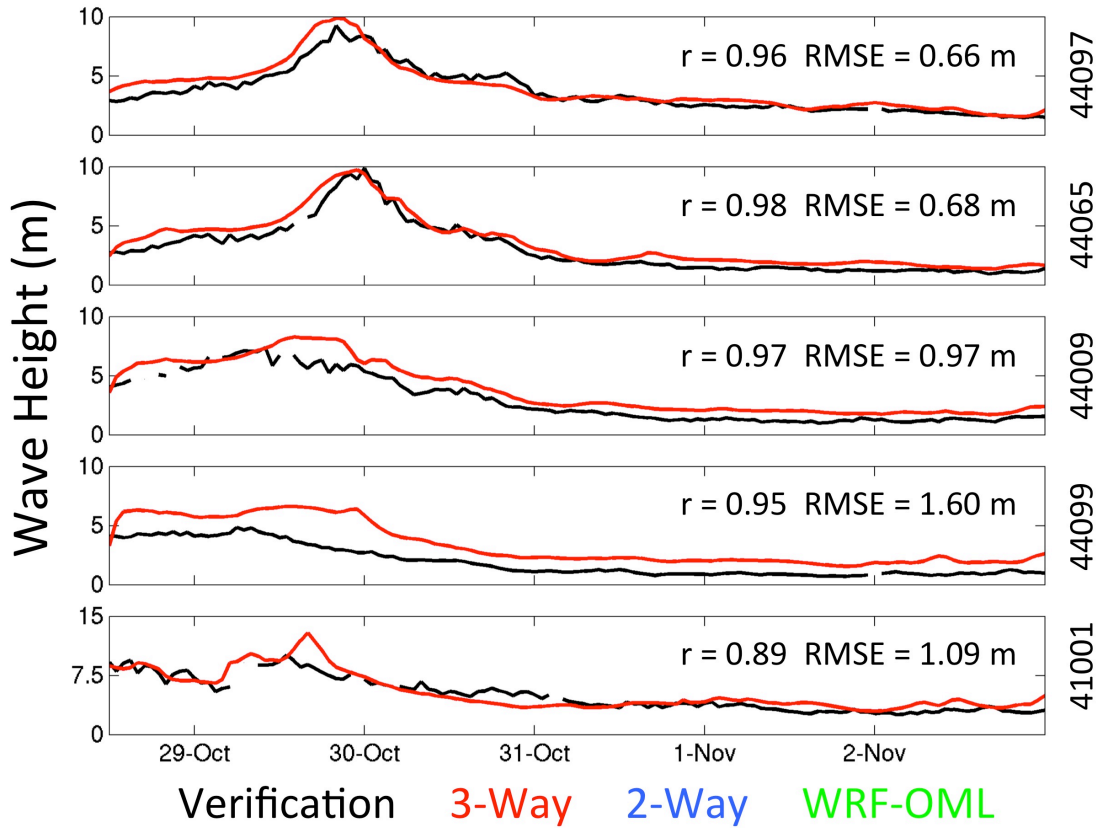


**Figure 3.9.** Simulated significant wave height comparisons to *in situ* buoy data collected at 5 locations along the U.S. east coast demonstrated in Figure 3.3. Verification along with the wave-coupled (*3-Way*) experiment is shown throughout the entire model simulation (132 hr). Also shown are correlation coefficients ( $r$ ) and root-mean-square error (RMSE)

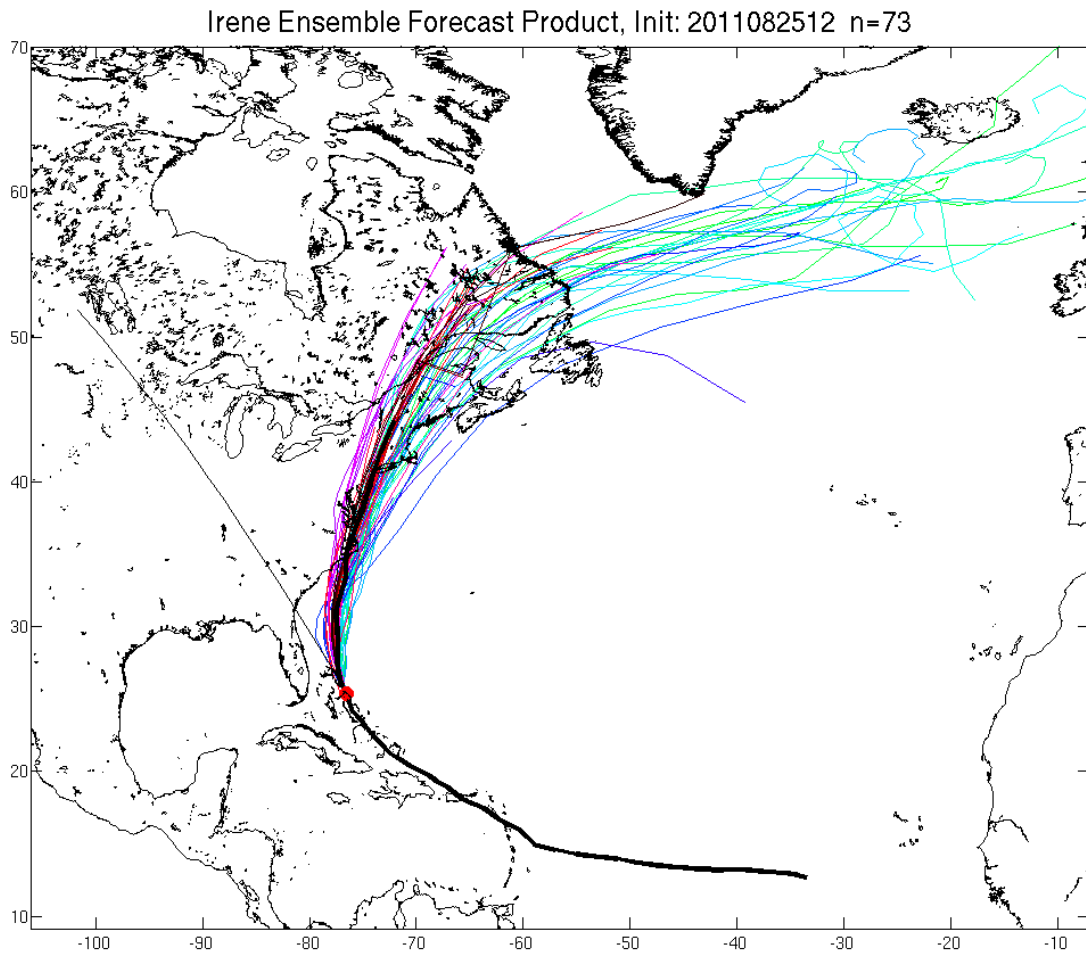


**Figure 4.1.** Hurricane Irene's track through the Atlantic Ocean (black). Thinner colored lines demonstrate the forecast tracks of ensemble members ( $n=73$ ) at the time of forecast initialization (12 UTC 25 August 2011). Thicker lines through the middle of the swath denote model experiment simulations. The red dot denotes the NHC Best Track location of Hurricane Irene at forecast simulation initialization

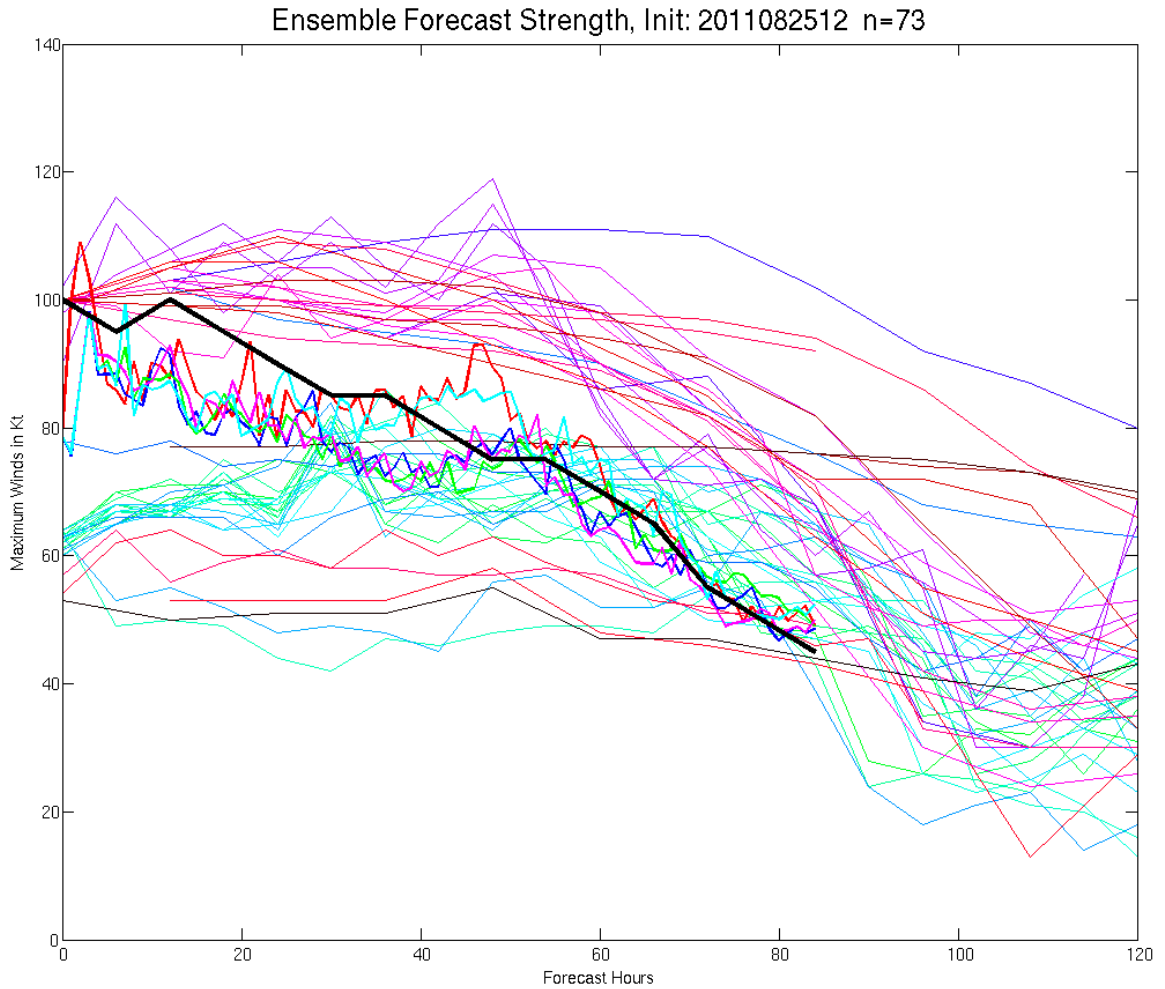


**Figure 4.2.** Hurricane Irene’s strength (black) from model initialization (12 UTC 25 August 2011) through model termination (00 UTC 29 August 2011). Thinner colored lines demonstrate the forecast tracks of ensemble members (n=73) at the time of forecast initialization (12 UTC 25 August 2011) through completion of a 120 hr forecast (12 UTC 30 August 2011). Thicker lines through the middle of the swath denote our forecast simulations and include 5 experiments: *WRF-Static* (cyan), *WRF-Filter* (pink), *WRF-Dynamic* (green), *2-Way* (blue), *3-Way* (red)

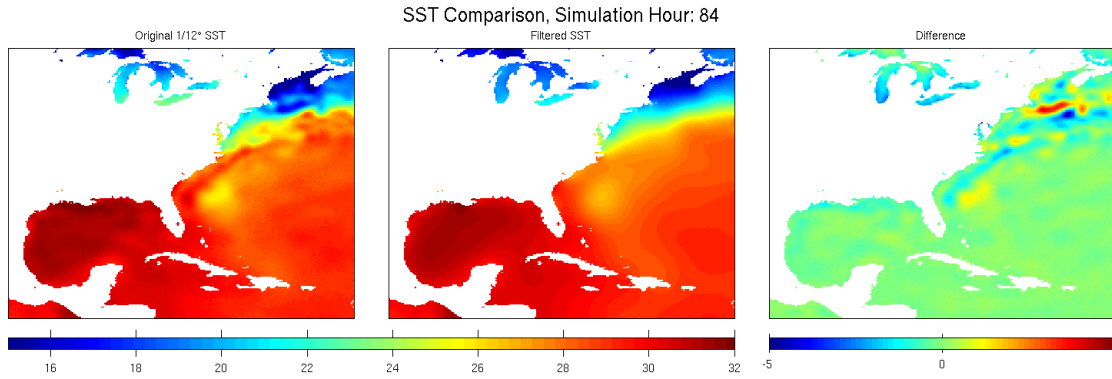


**Figure 4.3.** Spatial SST comparison between the original 1/12° RTG-SST (Gemmill et al. 2007; left column) product and the 1-2-1 filtered SST product (middle column). The difference (Original – Filtered) between the two fields is also shown (right column)

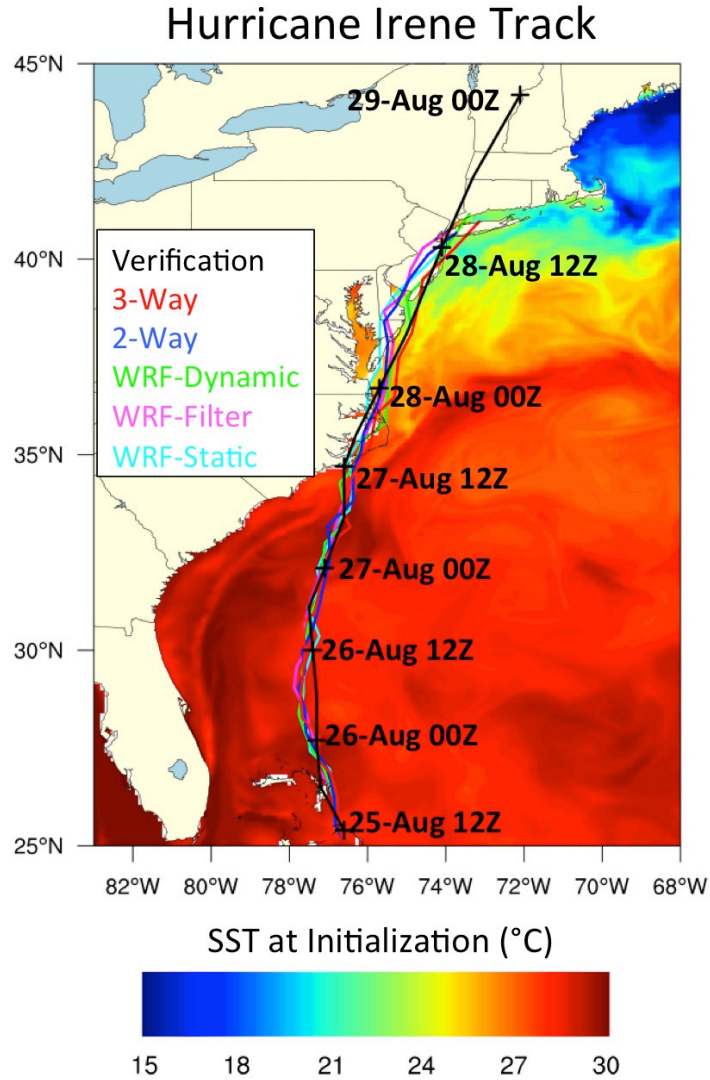


**Figure 4.4.** Simulated track comparison of 5 experiments: *WRF-Static* (cyan), *WRF-Filter* (pink), *WRF-Dynamic* (green), *2-Way* (blue), *3-Way* (red). The NHC Best Track product is used for verification (black). SST at initialization from the *3-Way* case is shaded

Forecast Valid: 27-Aug-2011 17Z

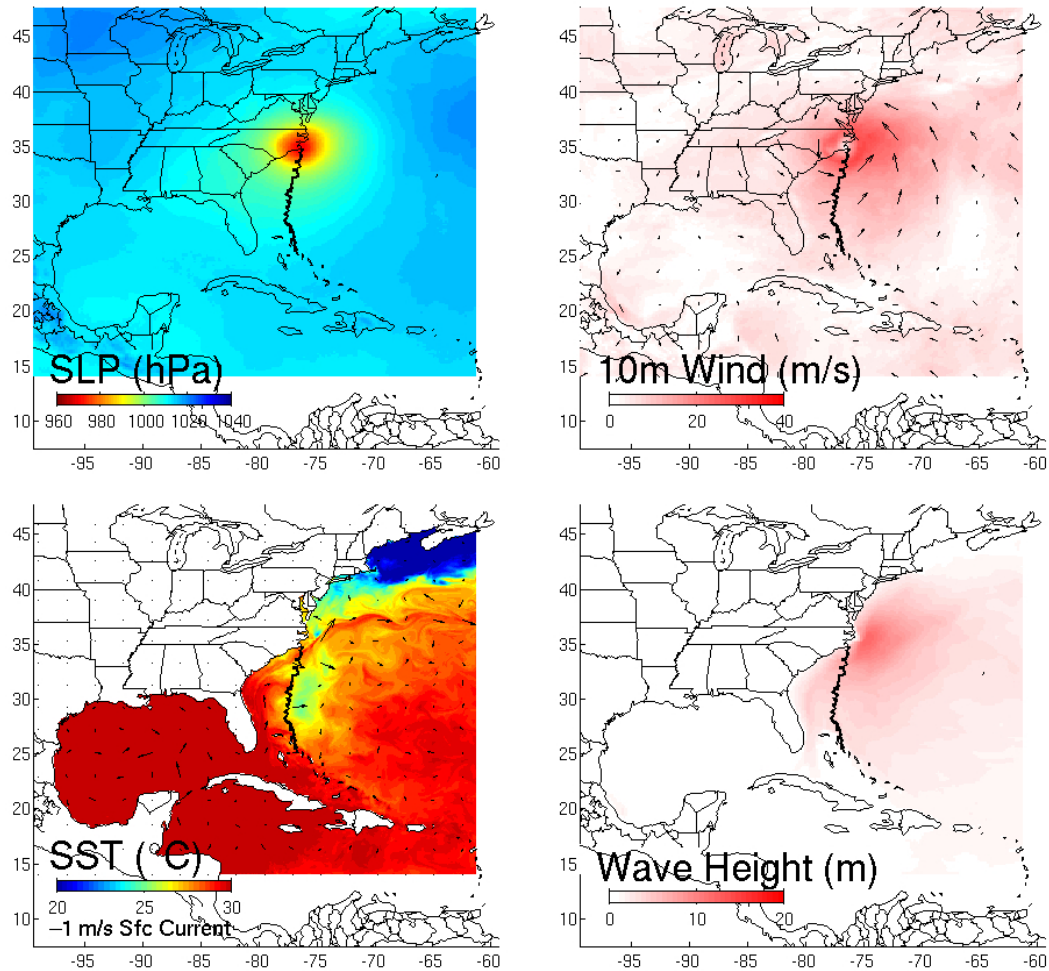


**Figure 4.5.** 4-panel plot of the *3-Way* experiment demonstrating the atmosphere, ocean, and wave environments at the time of simulated landfall in North Carolina (17 UTC 27 August 2011). The atmospheric environment is represented as quantities of SLP (upper left, shaded) and wind (upper right, shaded with vector arrows). The ocean environment is represented by SST (lower left, shaded) and surface current (lower left, vector arrows). The wave environment is represented by significant wave height (lower right, shaded)

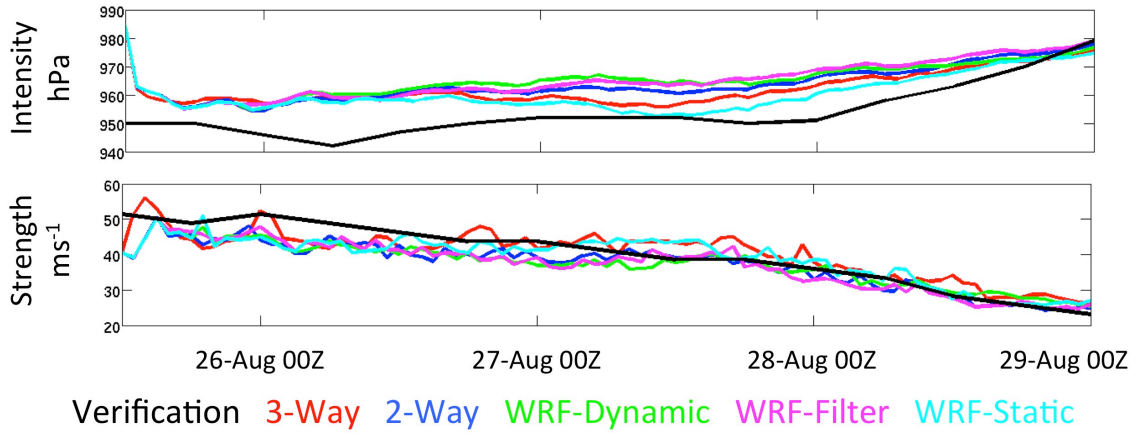


**Figure 4.6.** Simulated comparison of intensity (hPa) and strength ( $\text{ms}^{-1}$ ) of 5 experiments: *WRF-Static* (cyan), *WRF-Filter* (pink), *WRF-Dynamic* (green), *2-Way* (blue), *3-Way* (red). The NHC Best Track product is used for verification (black)

# Hurricane Irene Track

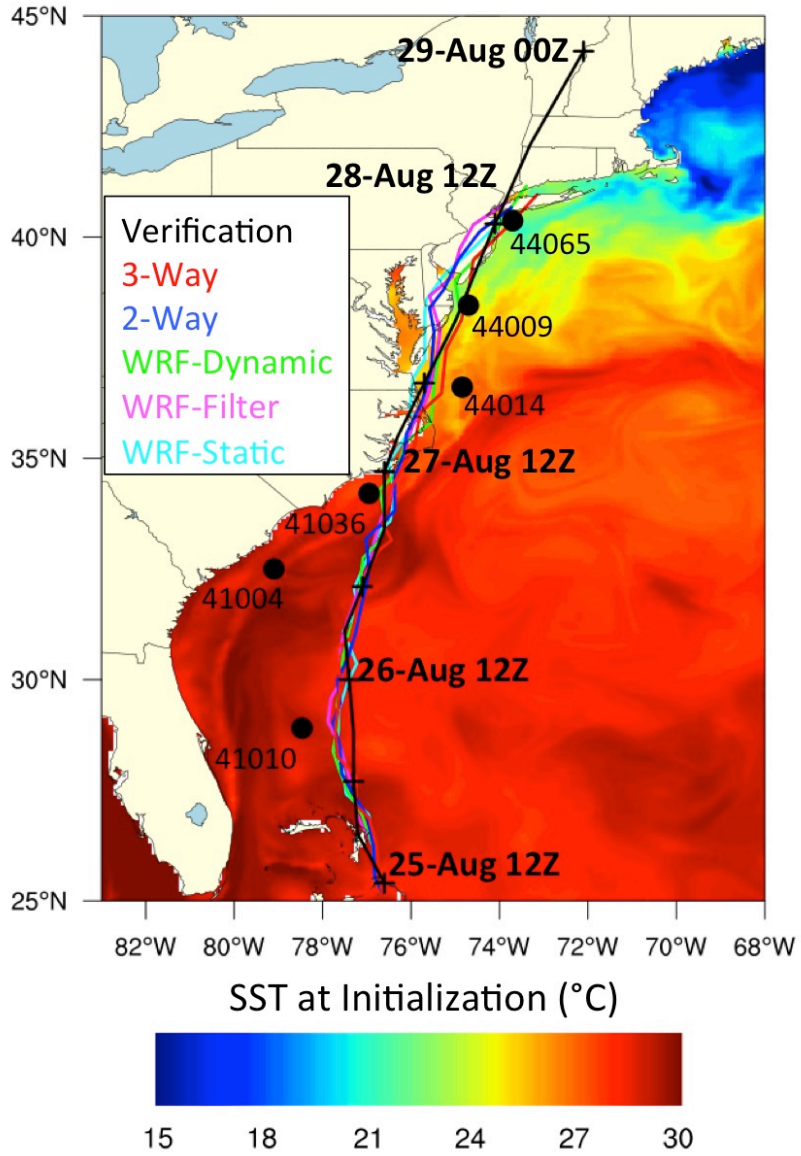


**Figure 4.7.** Track positions demonstrated as in Fig. 4.4 but with the addition of the 6 *in situ* buoys utilized for analysis in Figs. 4.8, 4.9, 4.12, and 4.24

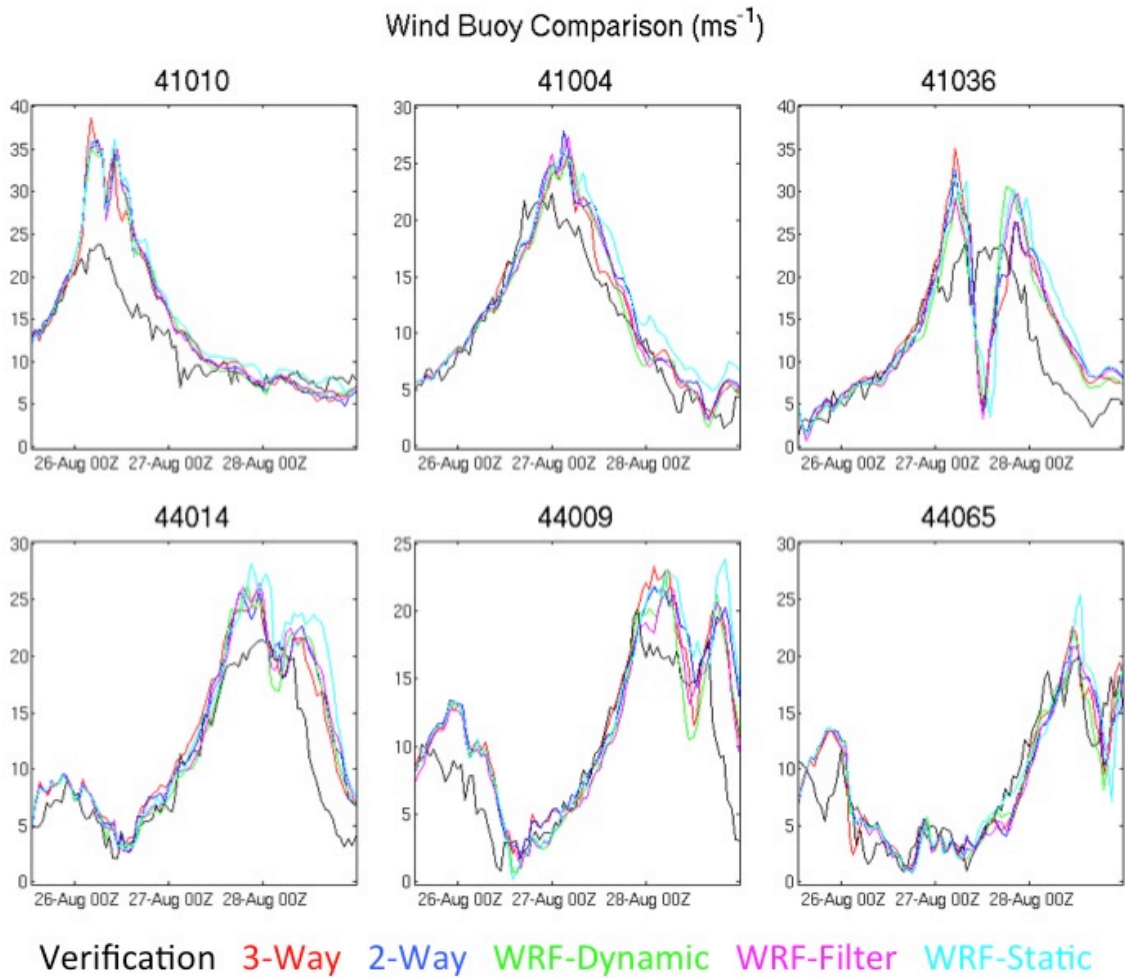


**Figure 4.8.** Simulated 10 m wind speed comparisons to *in situ* buoy data collected at 6 locations along the U.S. east coast demonstrated in Figure 4.7. Verification along with 5 experiments are shown throughout the entire model simulation (84 hr)

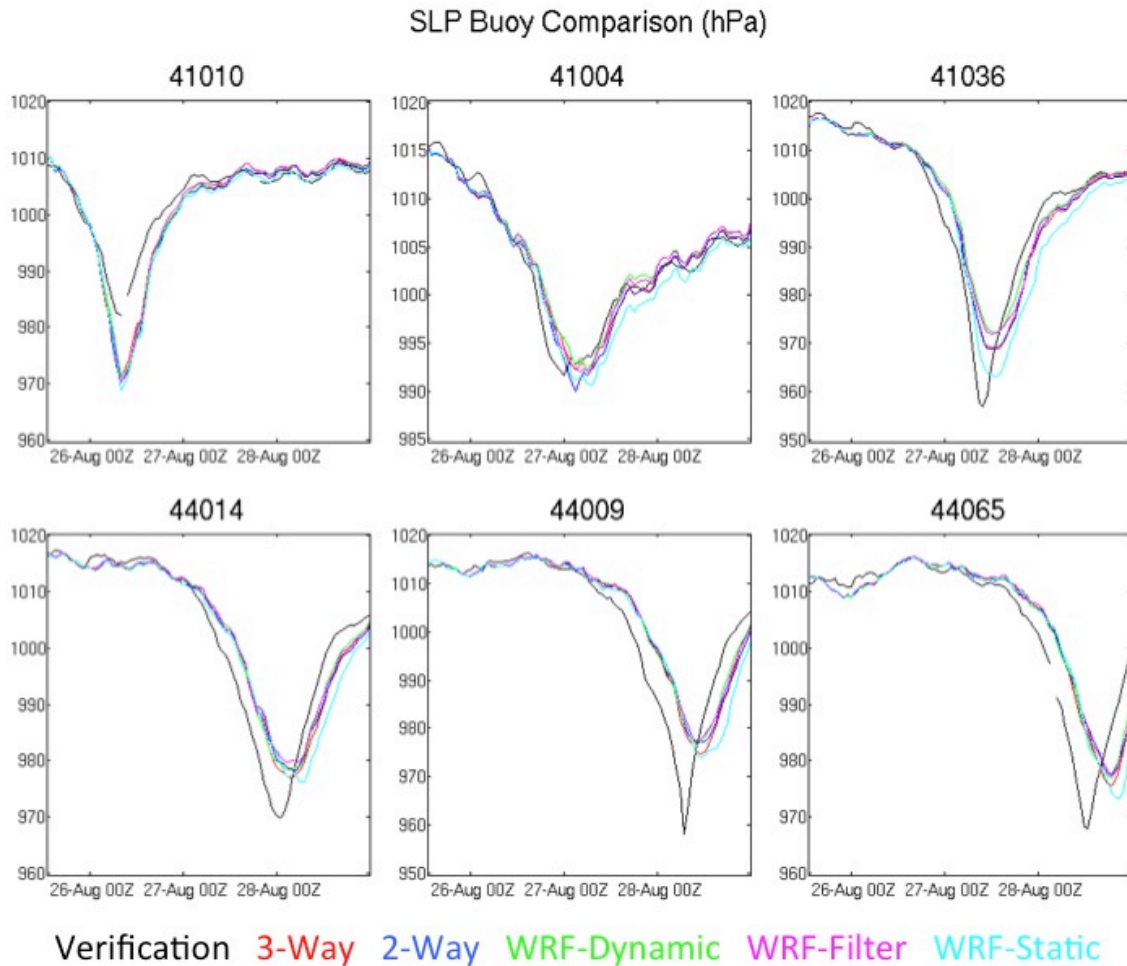


**Figure 4.9.** Simulated SLP comparisons to *in situ* buoy data collected at 6 locations along the U.S. east coast demonstrated in Figure 4.7. Verification along with 5 experiments are shown throughout the entire model simulation (84 hr)

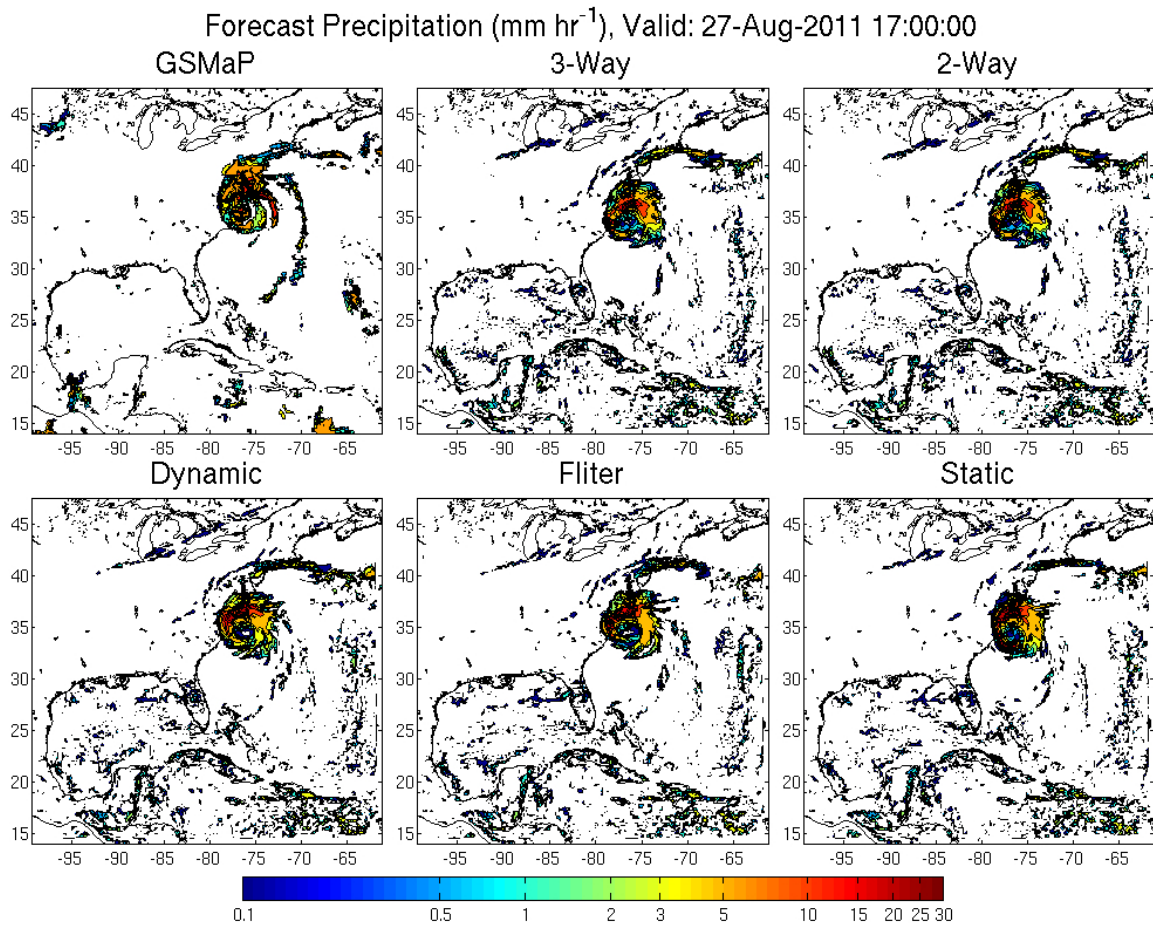


**Figure 4.10.** Forecast simulated precipitation rate ( $\text{mm hr}^{-1}$ ) of 5 experiments compared to satellite-derived Global Satellite Mapping of Precipitation (GSMaP) product (upper-left). Included are experiments *3-Way* (upper-middle), *2-Way* (upper-right), *WRF-Dynamic* (lower-left), *WRF-Filter* (lower-middle), and *WRF-Static* (lower-right)

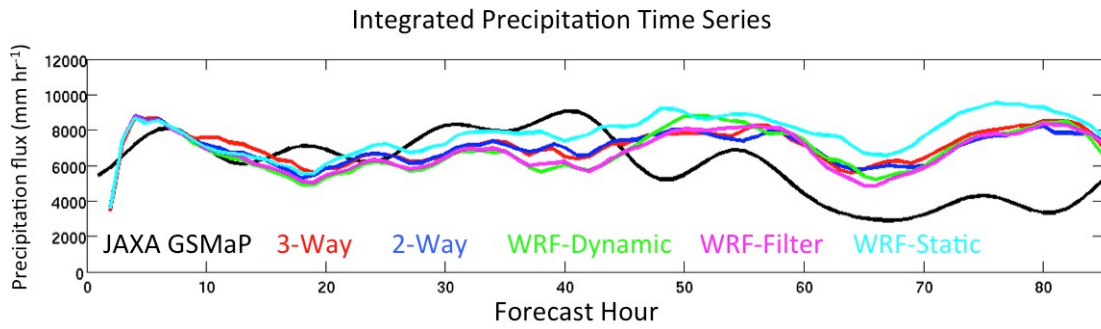


**Figure 4.11.** Forecast simulated precipitation flux (mm hr<sup>-1</sup>) integrated over all simulated grid points. Comparison of 5 experiments to satellite-derived Global Satellite Mapping of Precipitation (GSMaP) product (black). 5 experiments: *WRF-Static* (cyan), *WRF-Filter* (pink), *WRF-Dynamic* (green), *2-Way* (blue), *3-Way* (red)

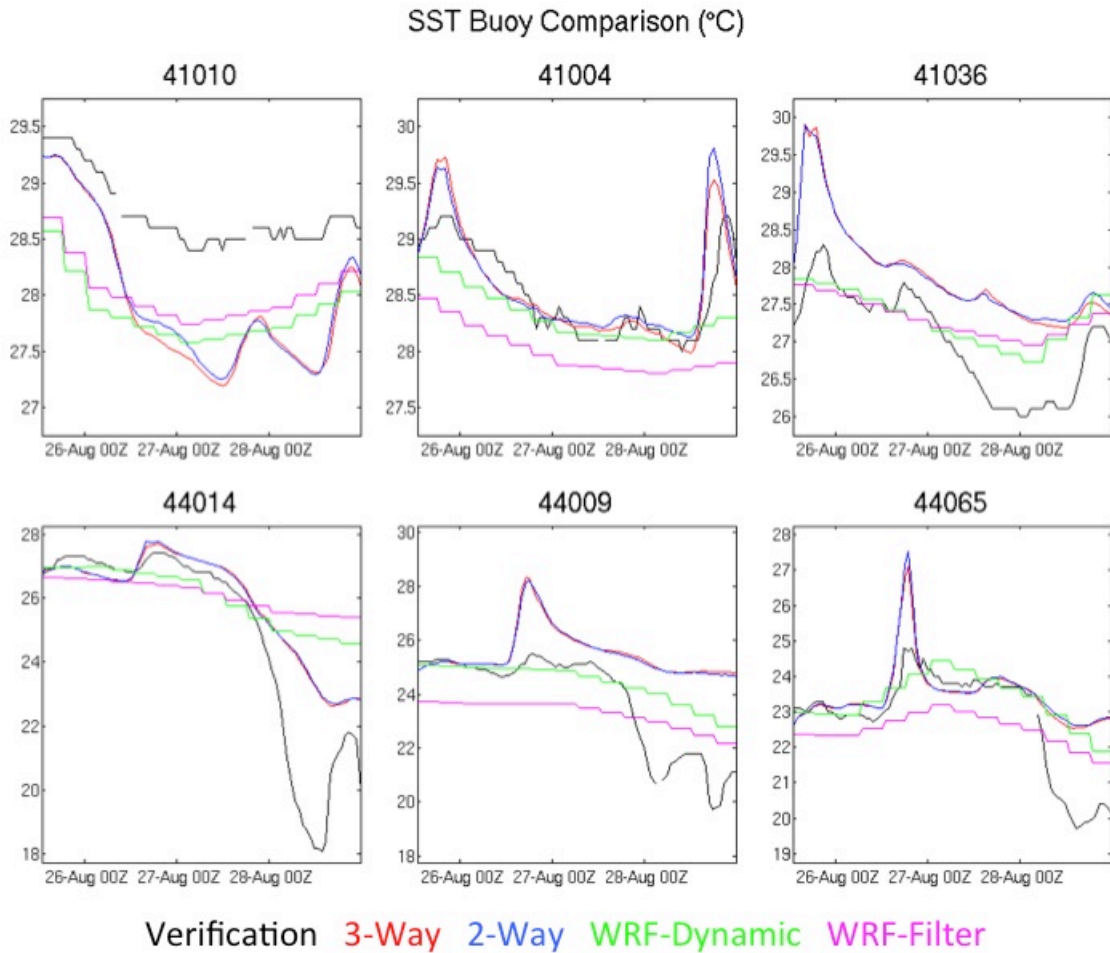


**Figure 4.12.** Simulated SST comparisons to *in situ* buoy data collected at 6 locations along the U.S. east coast demonstrated in Figure 4.7. Verification along with 4 experiments are shown throughout the entire model simulation (84 hr). SST in the *WRF-Static* case is not shown as it is demonstrated by the initial *WRF-Dynamic* SST across the entire time series. Remaining experiments are shown, 4 experiments: *WRF-Filter* (pink), *WRF-Dynamic* (green), *2-Way* (blue), *3-Way* (red)

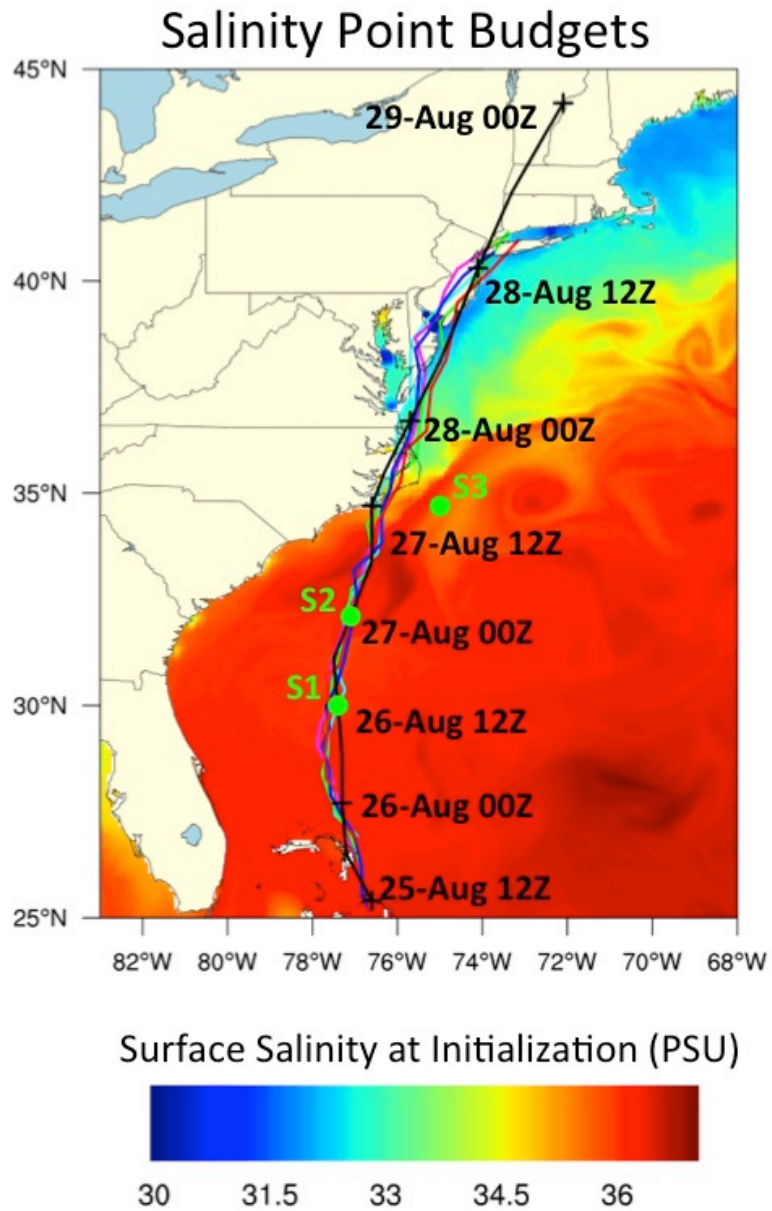


**Figure 4.13.** Track positions demonstrated as in Fig. 4.4 but with the addition of the 3 point locations utilized for time series analysis of the salinity budget in Figures 4.14, 4.15 and 4.16

### Salinity Budget, Point S1

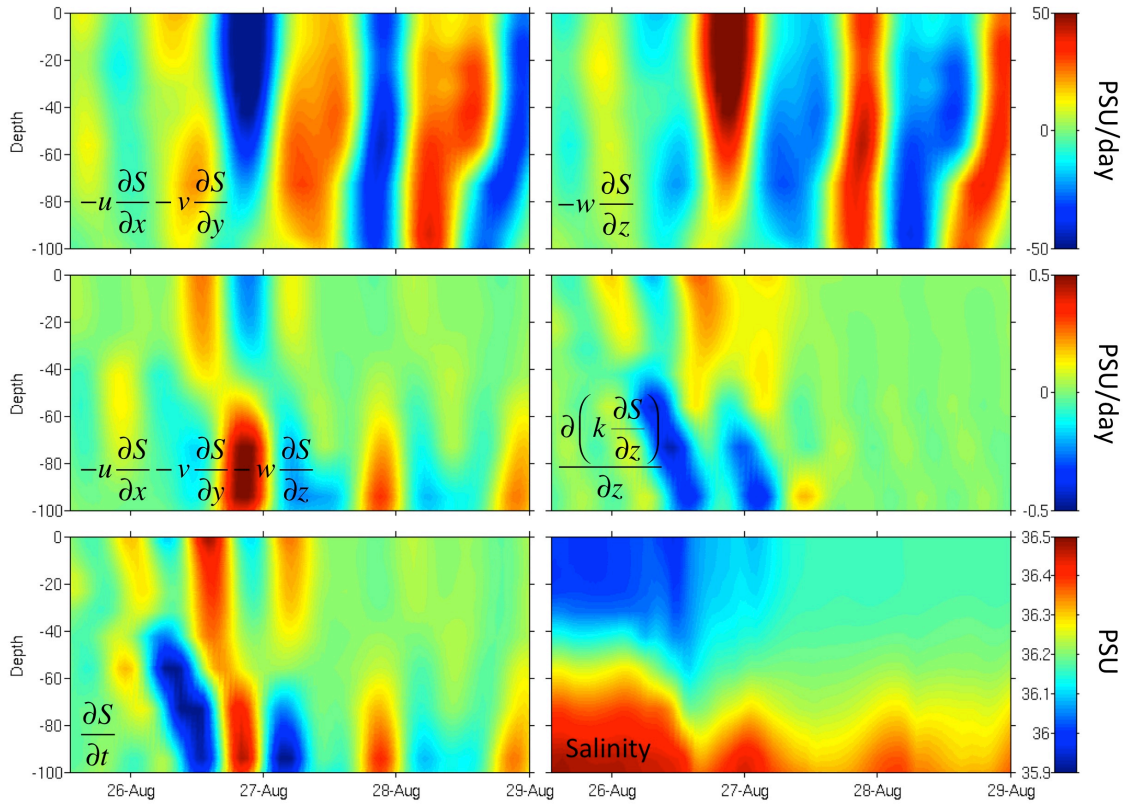


**Figure 4.14.** Ocean model (*2-Way*) analysis of salinity budget at point S1 in Fig. 4.13 from initialization (12 UTC 25 August 2011) through termination (00 UTC 29 August 2011). Horizontal advection term in PSU/day (upper-left), vertical advection term in PSU/day (upper-right), total advection term in PSU/day (middle-left), vertical diffusion term in PSU/day (middle-right), total local rate of change term in PSU/day (lower-left), salinity in PSU (lower-right)

### Salinity Budget, Point S2

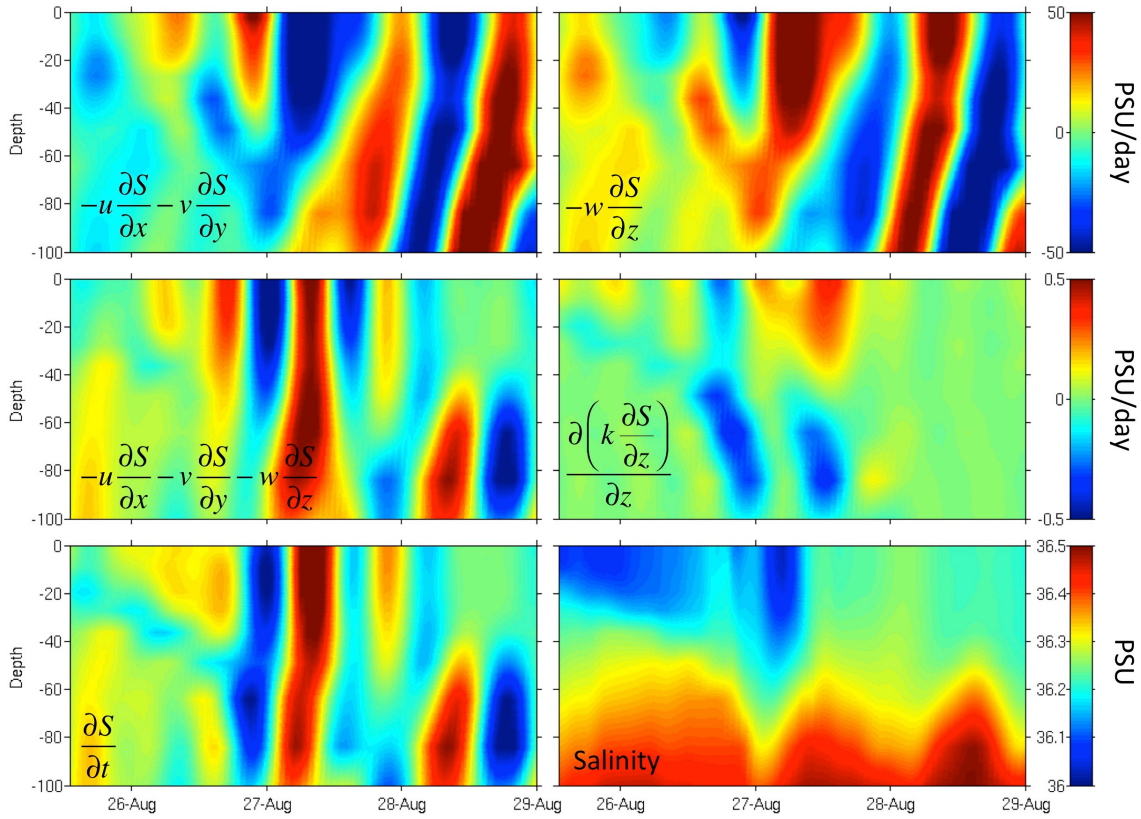


**Figure 4.15.** Ocean model (*2-Way*) analysis of salinity budget at point S2 in Fig. 4.13 from initialization (12 UTC 25 August 2011) through termination (00 UTC 29 August 2011). Horizontal advection term in PSU/day (upper-left), vertical advection term in PSU/day (upper-right), total advection term in PSU/day (middle-left), vertical diffusion term in PSU/day (middle-right), total local rate of change term in PSU/day (lower-left), salinity in PSU (lower-right)

### Salinity Budget, Point S3

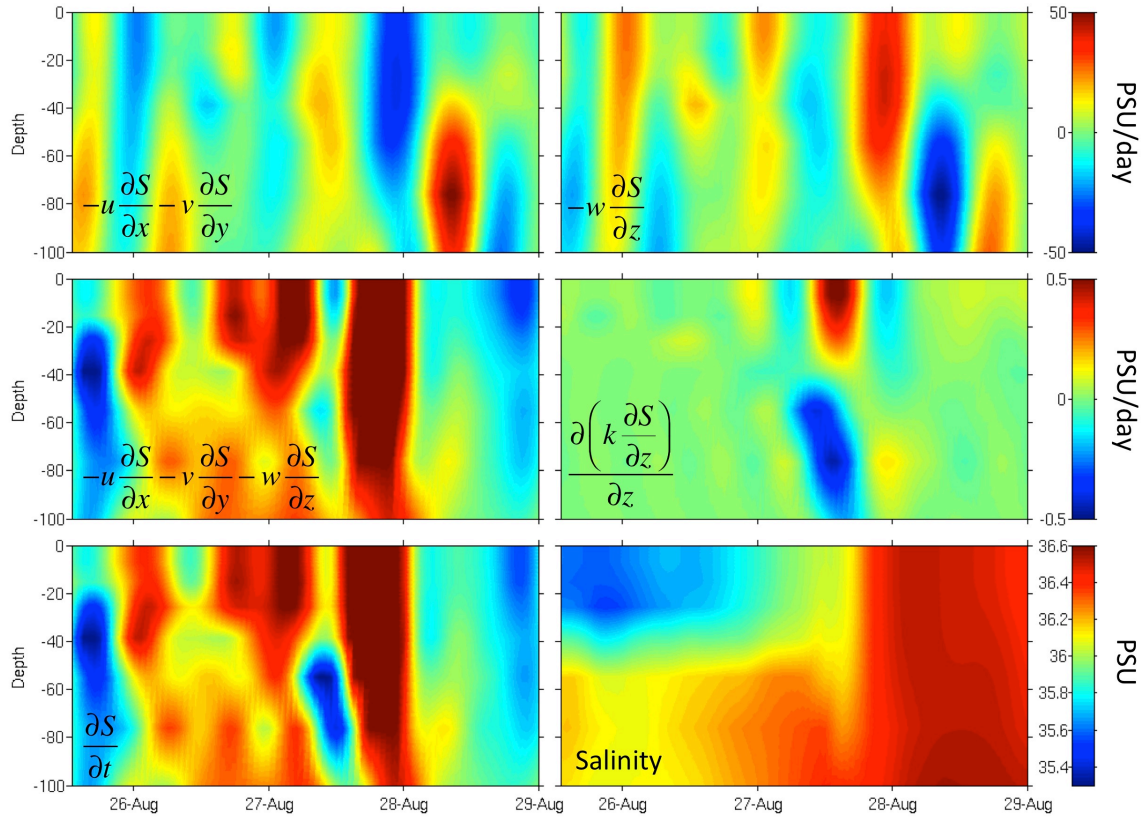


**Figure 4.16.** Ocean model (*2-Way*) analysis of salinity budget at point S3 in Fig. 4.13 from initialization (12 UTC 25 August 2011) through termination (00 UTC 29 August 2011). Horizontal advection term in PSU/day (upper-left), vertical advection term in PSU/day (upper-right), total advection term in PSU/day (middle-left), vertical diffusion term in PSU/day (middle-right), total local rate of change term in PSU/day (lower-left), salinity in PSU (lower-right)

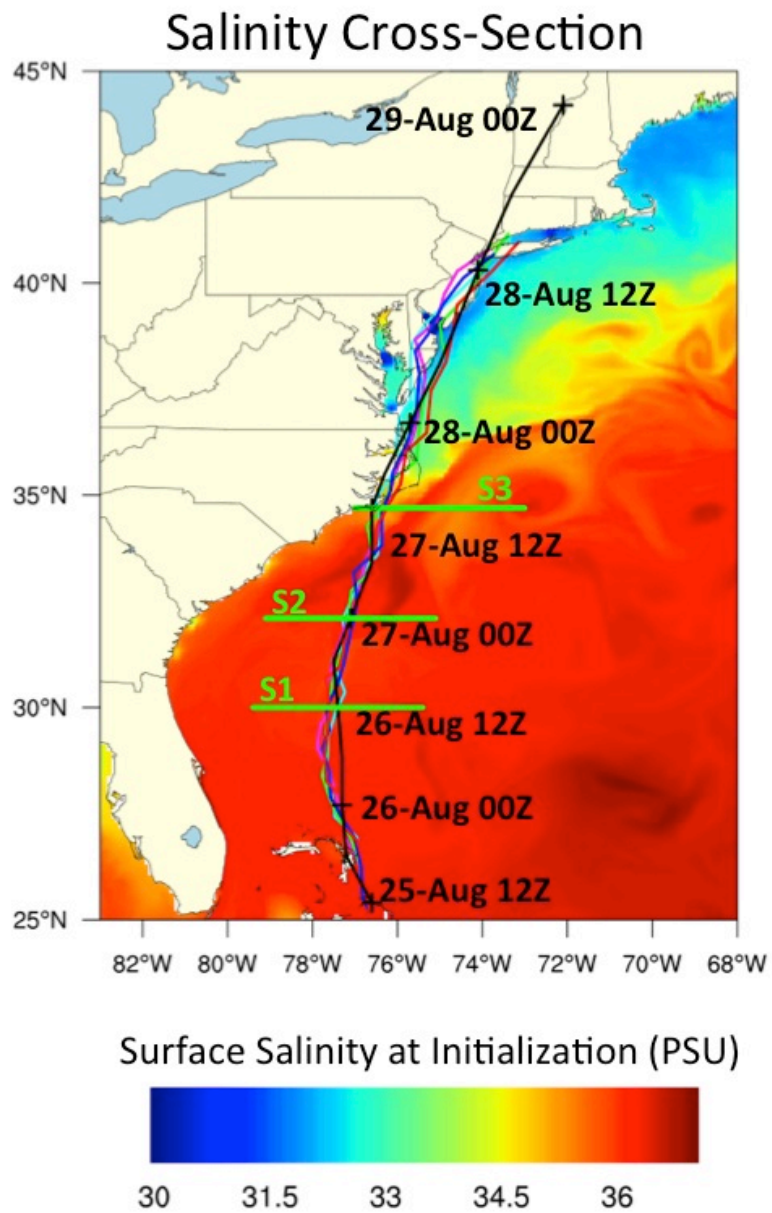


**Figure 4.17.** Track positions demonstrated as in Fig. 4.4 but with the addition of the 3 lines utilized for cross-section analysis of the upper-ocean salinity in Figs. 4.18, 4.19 and 4.20

## Salinity Cross-Section at Line S1

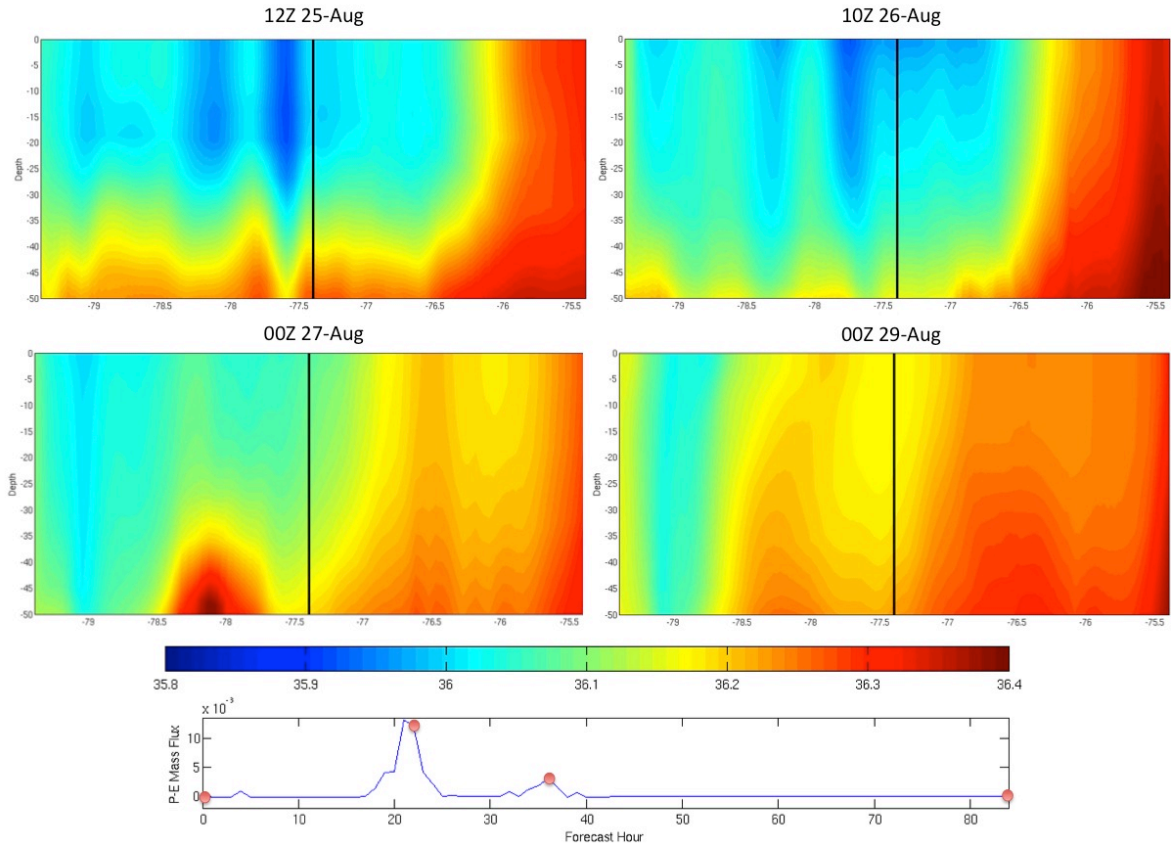


**Figure 4.18.** Cross-section of salinity at line S1 from Fig. 4.17 for the upper 50 m of ocean. Four times are chosen to represent the initial (12 UTC 25 August 2011; upper left), storm (10 UTC 26 August 2011; upper right), relaxation (00 UTC 27 August 2011; lower left), and termination (00 UTC 29 August 2011; lower right) periods. The black line denotes the approximate intersecting track of Hurricane Irene. Bottom line plot shows the Precipitation and Evaporation difference as a mass flux ( $\text{kg m}^2 \text{s}^{-1}$ ) with red circles to denote the instantaneous mass flux at the four chosen periods

## Salinity Cross-Section at Line S2

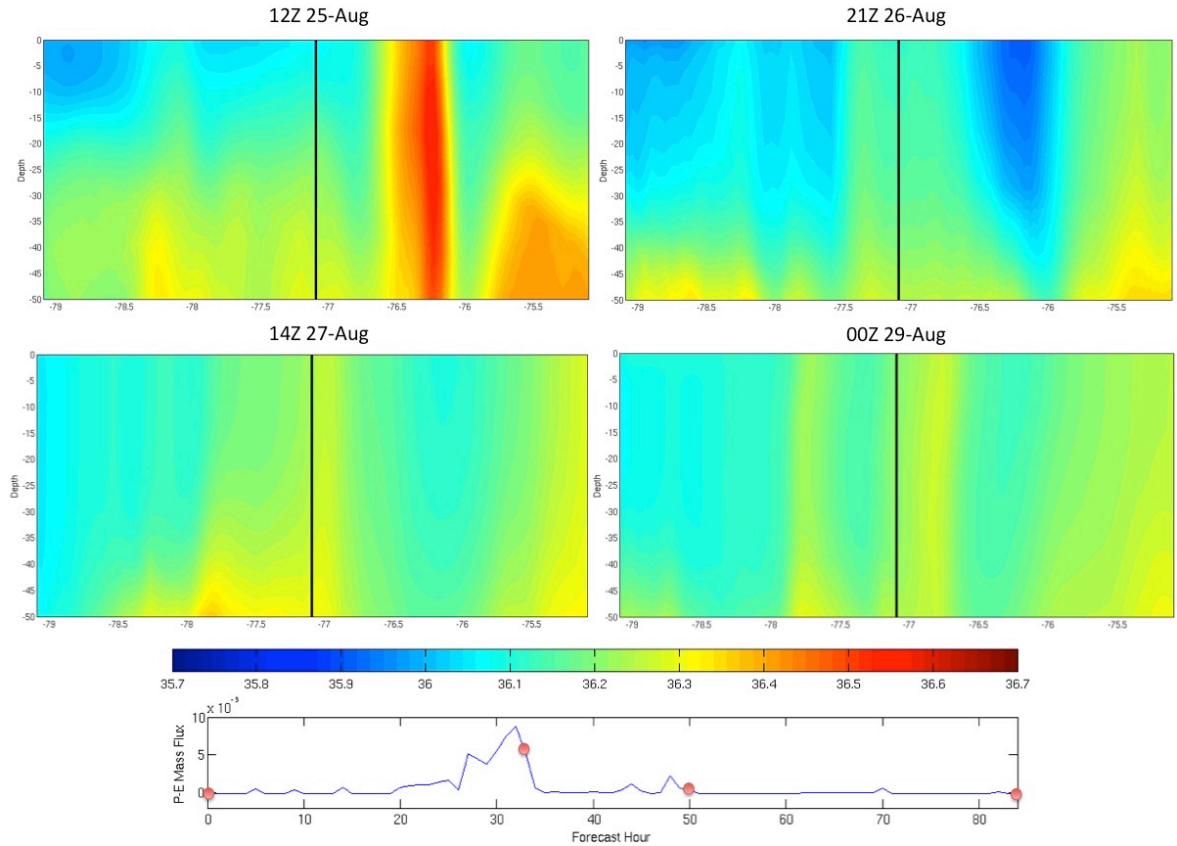


**Figure 4.19.** Cross-section of salinity at line S2 from Figure 4.17 for the upper 50 m of ocean. Four times are chosen to represent the initial (12 UTC 25 August 2011; upper left), storm (21 UTC 26 August 2011; upper right), relaxation (14 UTC 27 August 2011; lower left), and termination (00 UTC 29 August 2011; lower right) periods. The black line denotes the approximate intersecting track of Hurricane Irene. The black line denotes the approximate intersecting track of Hurricane Irene. Bottom line plot shows the Precipitation and Evaporation difference as a mass flux ( $\text{kg m}^2 \text{s}^{-1}$ ) with red circles to denote the instantaneous mass flux at the four chosen periods

## Salinity Cross-Section at Line S3

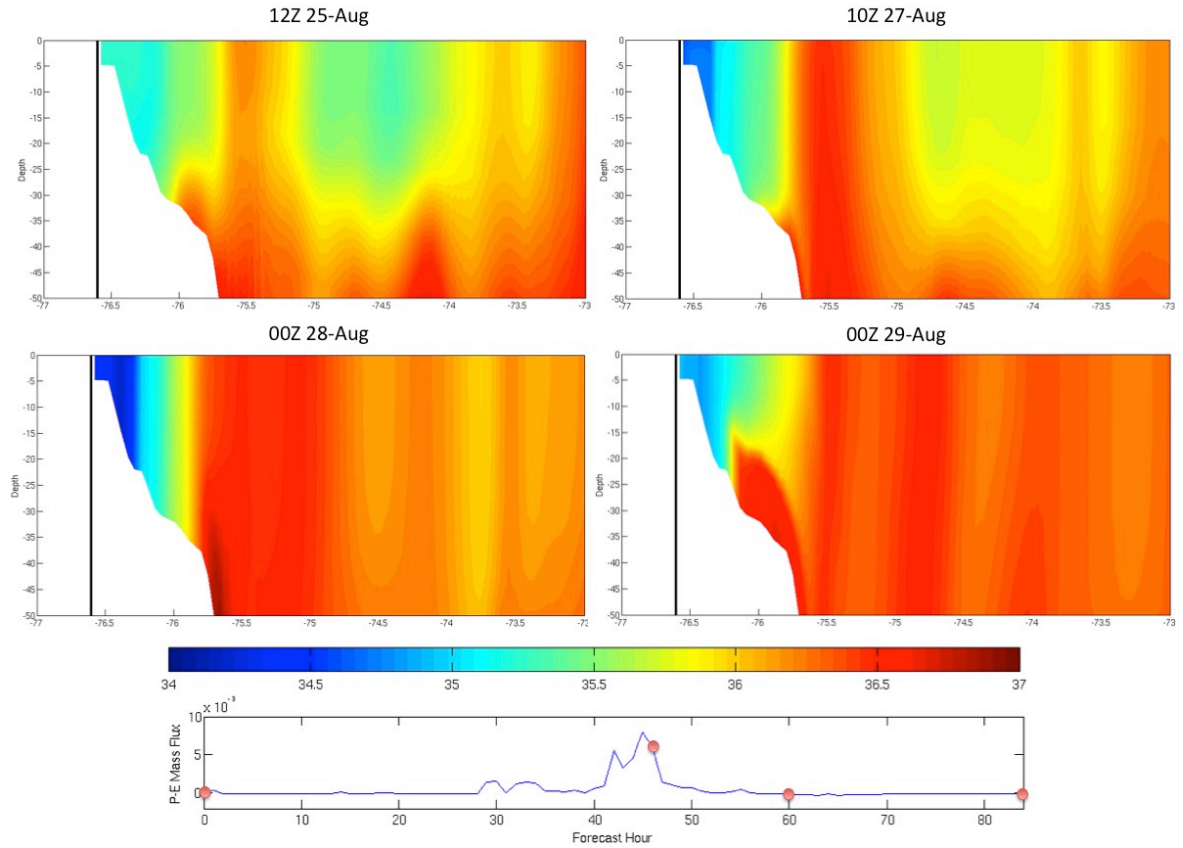


**Figure 4.20.** Cross-section of salinity at line S3 from Figure 4.17 for the upper 50 m of ocean. Four times are chosen to represent the initial (12 UTC 25 August 2011; upper left), storm (10 UTC 27 August 2011; upper right), relaxation (00 UTC 28 August 2011; lower left), and termination (00 UTC 29 August 2011; lower right) periods. Bottom line plot shows the Precipitation and Evaporation difference as a mass flux ( $\text{kg m}^2 \text{s}^{-1}$ ) with red circles to denote the instantaneous mass flux at the four chosen periods

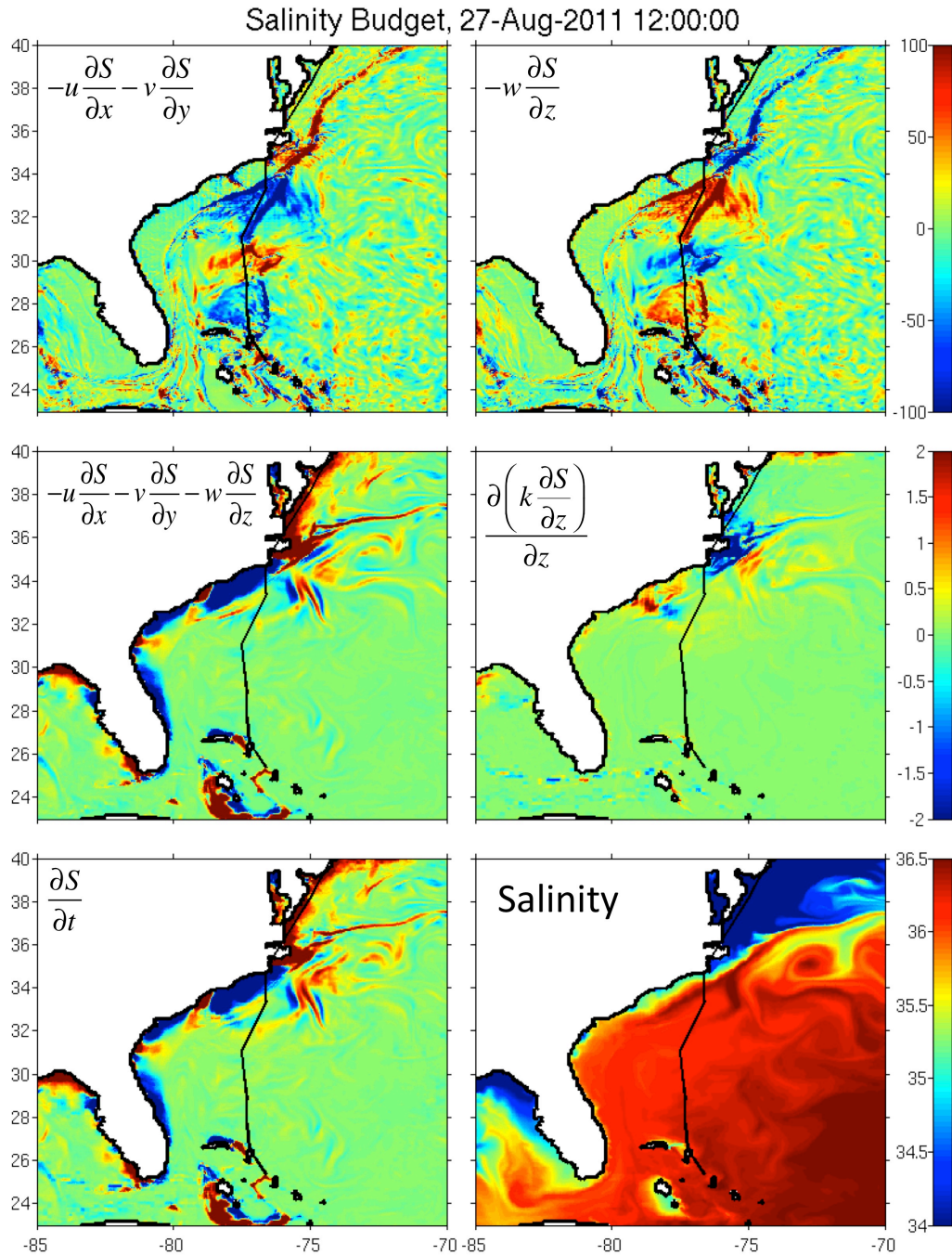


**Figure 4.21.** Spatial analysis of the surface salinity budget as Hurricane Irene makes landfall (12 UTC 27 August 2011) in North Carolina, *2-Way EMINUSP* (realistic precipitation flux) experiment.. Terms of the salinity budget are horizontal advection (upper-left), vertical advection (upper-right), total advection (middle-left), vertical diffusion (middle-right), total salinity rate of change (lower left), and a snapshot of the surface salinity

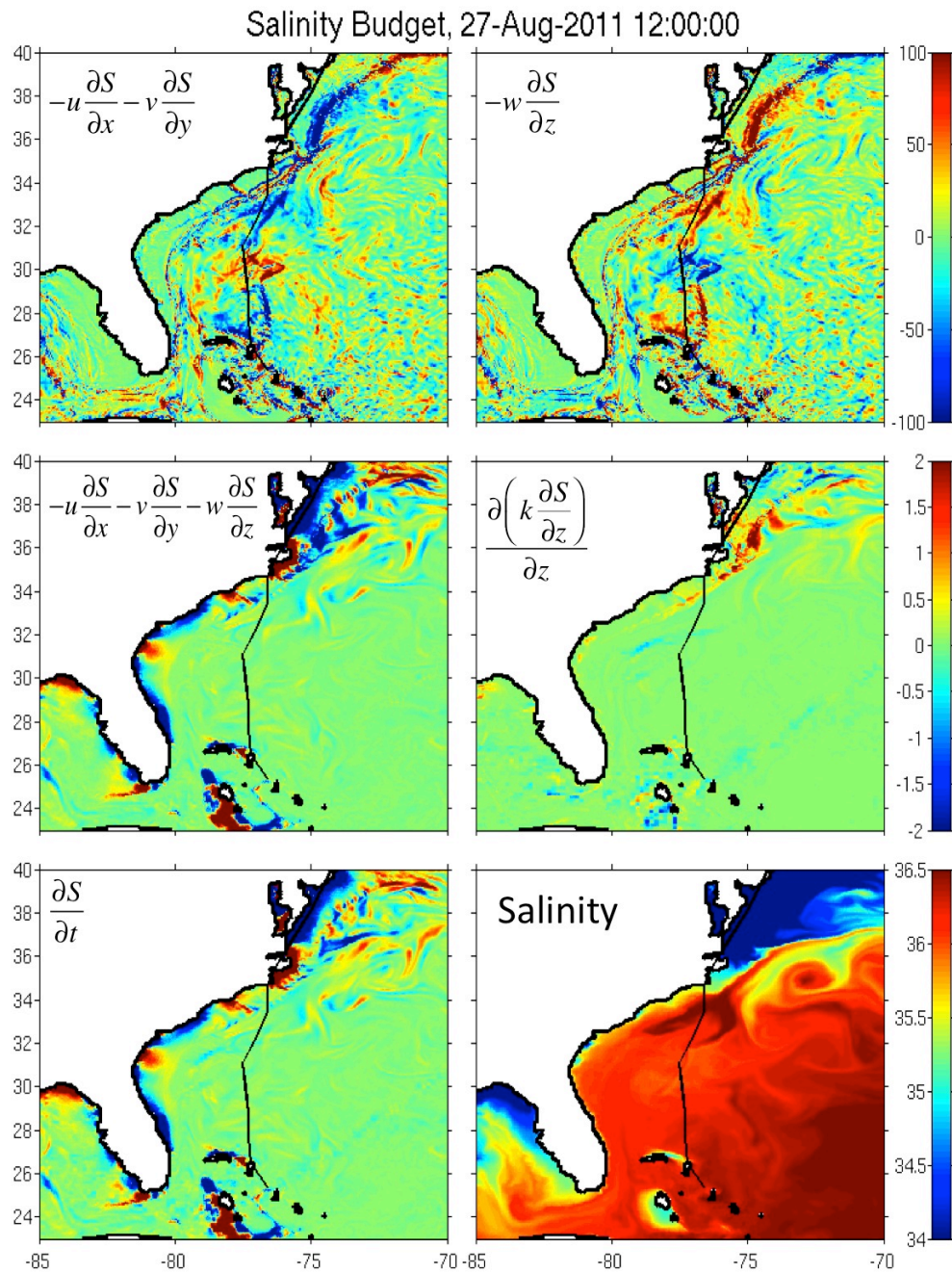


**Figure 4.22.** Spatial analysis of the surface salinity budget as Hurricane Irene makes landfall (12 UTC 27 August 2011) in North Carolina, *2-Way ANA\_SSFLUX* (analytical surface salt flux) experiment. Terms of the salinity budget are horizontal advection (upper-left), vertical advection (upper-right), total advection (middle-left), vertical diffusion (middle-right), total salinity rate of change (lower left), and a snapshot of the surface salinity

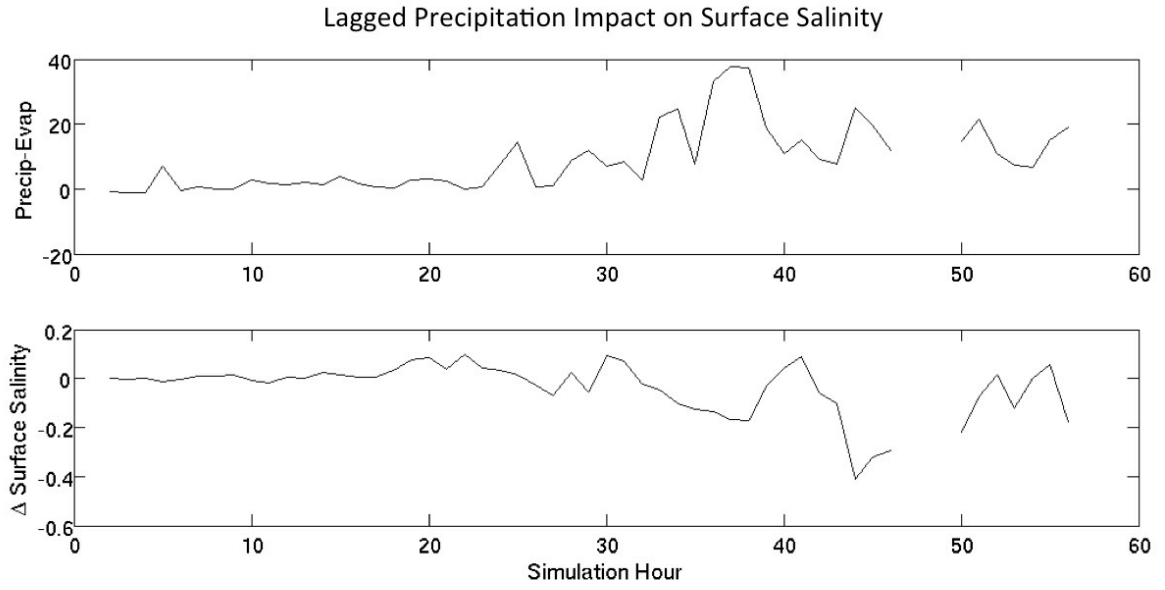
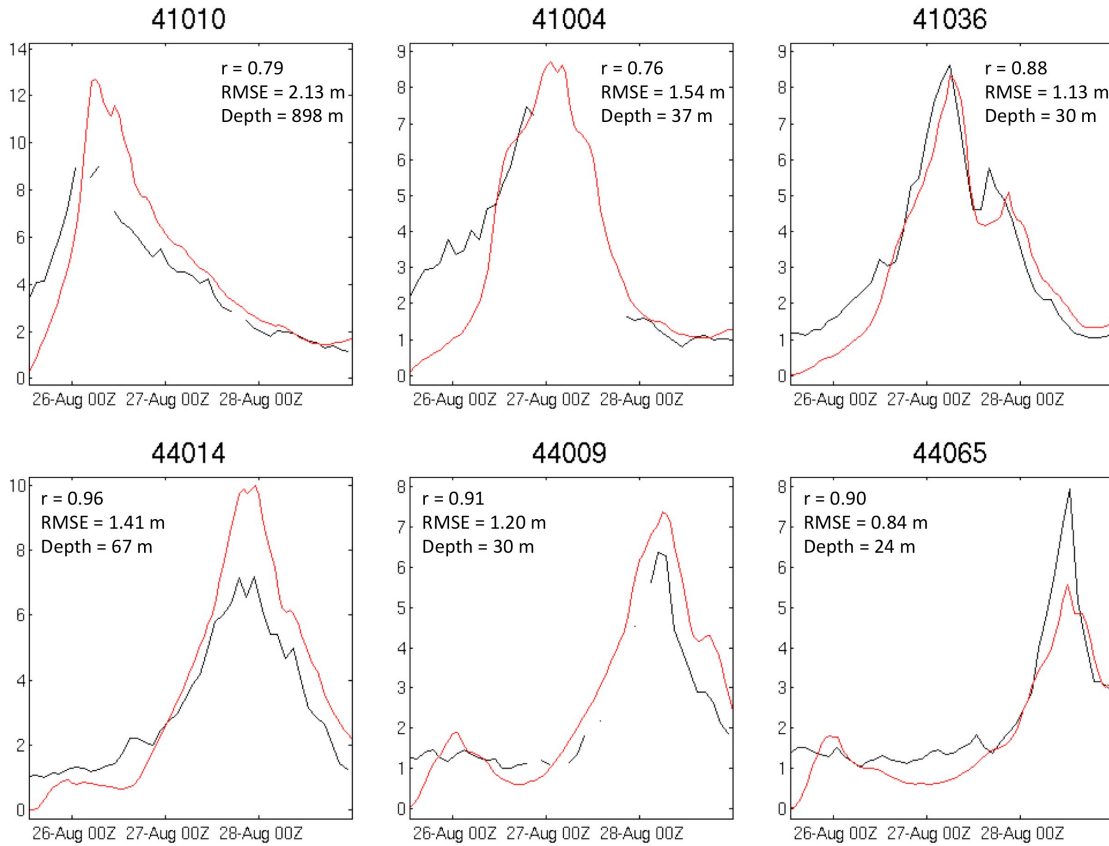


**Figure 4.23.** Precipitation at the location of the storm center 10 hours (lag) after the forecast time. Lagged storm location is necessary as the precipitation at the storm center would not be indicative of the strongest precipitation. The best time interval of lag was determined based on the anti-correlation of these two time series (e.g. high precipitation induces low surface salinity). The difference in surface salinity is from *EMINUSP* subtracted from *ANA\_SSFLUX* (negative values denote lower salinity in *EMINUSP*). Missing data points are when the lagged storm center is located over land

### Wave Height Buoy Comparison (m)



### Verification 3-Way

**Figure 4.24.** Simulated significant wave height comparisons to *in situ* buoy data collected at 6 locations along the U.S. east coast demonstrated in Figure 4.7. Verification along with the 3-Way experiments is shown throughout the entire model simulation (84 hr). Comparison also shows the correlation coefficient ( $r$ ), Root-Mean-Square Error (RMSE; in m) and modeled depth (m) at each location

## REFERENCES

- Andreas, E. L., and K. A. Emanuel, 2001: Effects of sea spray on tropical cyclone intensity. *J. Atmos. Sci.*, **58**, 3741–3751.
- Aonashi, K., and Coauthors, 2009: A Kalman Filter Approach to the Global Satellite Mapping of Precipitation (GSMaP) from Combined Passive Microwave and Infrared Radiometric Data. *JMSJ*, **87**, 137–151.
- Asher, W. E., A. T. Jessup, R. Branch, and D. Clark, 2014: Observations of rain-induced near-surface salinity anomalies. *J. Geophys. Res. Oceans*, **119**, 5483–5500, doi:10.1002/2014JC009954.
- Avila, L. A., and J. Cangialosi, 2011: Tropical Cyclone Report: Hurricane Irene (AL092011) 21–28 August 2011. *NOAA National Hurricane Center*. 45p.
- Bao, J. W., C. W. Fairall, S. A. Michelson, and L. Bianco, 2011: Parameterizations of Sea-Spray Impact on the Air–Sea Momentum and Heat Fluxes. *Monthly Weather Review*, **139**, 3781–3797, doi:10.1175/MWR-D-11-00007.1.
- Bao, J. W., J. M. Wilczak, J. K. Choi, and L. H. Kantha, 2000: Numerical Simulations of Air–Sea Interaction under High Wind Conditions Using a Coupled Model: A Study of Hurricane Development. *Monthly Weather Review*, **128**, 2190–2210, doi:10.1175/1520-0493(2000)128<2190:NSOASI>2.0.CO;2.
- Bao, S., S. Raman, and L. Xie, 2003: Numerical simulation of the response of the ocean surface layer to precipitation. *Pure Appl. Geophys.*, **160**, 2419–2446.
- Bassill, N. P., 2014: Accuracy of early GFS and ECMWF Sandy (2012) track forecasts: Evidence for a dependence on cumulus parameterization. *Geophys. Res. Lett.*, **41**, 2014GL059839, doi:10.1002/2014GL059839.
- Bender, M. A., I. Ginis, and Y. Kurihara, 1993: Numerical simulations of tropical cyclone–ocean interaction with a high-resolution coupled model. *J. Geophys. Res.*, **98**, 23245, doi:10.1029/93JD02370.
- Bender, M. A., I. Ginis, R. Tuleya, B. Thomas, and T. Marchok, 2007: The Operational GFDL Coupled Hurricane–Ocean Prediction System and a Summary of Its Performance. *Monthly Weather Review*, **135**, 3965–3989, doi:10.1175/2007MWR2032.1.
- Bender, M., and I. Ginis, 2000: Real-case simulations of hurricane–ocean interaction using a high-resolution coupled model: Effects on hurricane intensity. *Monthly Weather Review*, **128**, 917–946.

- Beven, J. L., II, and Coauthors, 2008: Atlantic Hurricane Season of 2005. *Tropical Prediction Center, NOAA/NWS/National Hurricane Center*.
- Blake, E. S., T. B. Kimberlain, R. J. Berg, J. P. Cangialosi, and J. L. Beven II, 2013: Tropical Cyclone Report: Hurricane Sandy Rep. AL182012. *National Hurricane Center*, 1–157.
- Blumberg, A. F., and G. L. Mellor, 1987: A description of a three-dimensional coastal ocean circulation model. *Three-dimensional coastal ocean models*, 1–16.
- Booij, N., R. C. Ris, and L. H. Holthuijsen, 1999: A third-generation wave model for coastal regions: 1. Model description and validation. *J. Geophys. Res.*, **104**, 7649, doi:10.1029/98JC02622.
- Brink, K. H., 1989: Observations of the Response of Thermocline Currents to a Hurricane. *J. Phys. Oceanogr.*, **19**, 1017–1022, doi:10.1175/1520-0485(1989)019<1017:OOTROT>2.0.CO;2.
- Charnock, H., 1955: Wind stress on a water surface. *Q. J. R. Meteorol. Soc.*, **81**, 639–640, doi:10.1002/qj.49708135027.
- Chassignet, E. P., H. E. Hurlburt, O. M. Smedstad, G. R. Halliwell, P. J. Hogan, A. J. Wallcraft, R. Baraille, and R. Bleck, 2007: The HYCOM (HYbrid Coordinate Ocean Model) data assimilative system. *Marine Environmental Monitoring and Prediction Selected papers from the 36th International Liège Colloquium on Ocean Dynamics 36th International Liège Colloquium on Ocean Dynamics*, **65**, 60–83, doi:10.1016/j.jmarsys.2005.09.016.
- Chen, F., and J. Dudhia, 2001: Coupling an Advanced Land Surface–Hydrology Model with the Penn State–NCAR MM5 Modeling System. Part I: Model Implementation and Sensitivity. *Monthly Weather Review*, **129**, 569–585, doi:10.1175/1520-0493(2001)129<0569:CAALSH>2.0.CO;2.
- Chen, S. S., W. Zhao, Dong, J. Price, E. Walsh, T. Sanford, and H. Tolman, 2007: The CBLAST-Hurricane Program and the Next-Generation Fully Coupled Atmosphere–Wave–Ocean Models for Hurricane Research and Prediction. *Bull. Amer. Meteor. Soc.*, **88**, 311–317, doi:doi: 10.1175/BAMS-88-3-311.
- Chen, S. S., W. Zhao, M. A. Donelan, and H. L. Tolman, 2013: Directional Wind–Wave Coupling in Fully Coupled Atmosphere–Wave–Ocean Models: Results from CBLAST-Hurricane. *J. Atmos. Sci.*, **70**, 3198–3215, doi:10.1175/JAS-D-12-0157.1.
- Church, J. A., T. M. Joyce, and J. F. Price, 1989: Current and Density Observations across the Wake of Hurricane Gay. *J. Phys. Oceanogr.*, **19**, 259–265, doi:doi: 10.1175/1520-0485(1989)019<0259:CADOAT>2.0.CO;2.

- Cornillon, P., L. Stramma, and J. Price, 1987: Satellite measurements of sea surface cooling during hurricane Gloria. *Nature*, **326**, 373–378.
- Csanady, G. T., 2001: *Air-sea interaction: laws and mechanisms*. Cambridge University Press, Cambridge, NY, 243 pp.
- Davis, C., and Coauthors, 2008: Prediction of Landfalling Hurricanes with the Advanced Hurricane WRF Model. *Monthly Weather Review*, **136**, 1990–2005, doi:10.1175/2007MWR2085.1.
- Done, J., C. A. Davis, and M. Weisman, 2004: The next generation of NWP: explicit forecasts of convection using the weather research and forecasting (WRF) model. *Atmosph. Sci. Lett*, **5**, 110–117, doi:10.1002/asl.72.
- Donelan, M. A., 2004: On the limiting aerodynamic roughness of the ocean in very strong winds. *Geophys. Res. Lett*, **31**, L18306, doi:10.1029/2004GL019460.
- Doyle, J. D., 2002: Coupled Atmosphere–Ocean Wave Simulations under High Wind Conditions. *Mon. Wea. Rev.*, **130**, 3087–3099, doi:doi: 10.1175/1520-0493(2002)130<3087:CAOWSU>2.0.CO;2.
- Drennan, W. M., P. K. Taylor, and M. J. Yelland, 2005: Parameterizing the Sea Surface Roughness. *J. Phys. Oceanogr.*, **35**, 835–848, doi:10.1175/JPO2704.1.
- Dudhia, J., 1989: Numerical Study of Convection Observed during the Winter Monsoon Experiment Using a Mesoscale Two-Dimensional Model. *J. Atmos. Sci.*, **46**, 3077–3107, doi:10.1175/1520-0469(1989)046<3077:NSOCOD>2.0.CO;2.
- Emanuel, K., 2005: Increasing destructiveness of tropical cyclones over the past 30 years. *Nature*, **436**, 686–688, doi:doi:10.1038/nature03906.
- Emanuel, K. A., 1986: An air-sea interaction theory for tropical cyclones. Part I: Steady-state maintenance. *J. Atmos. Sci.*, **43**, 585–605.
- Emanuel, K., C. DesAutels, C. Holloway, and R. Korty, 2004: Environmental Control of Tropical Cyclone Intensity. *J. Atmos. Sci.*, **61**, 843–858, doi:10.1175/1520-0469(2004)061<0843:ECOTCI>2.0.CO;2.
- Fairall, C. W., E. F. Bradley, D. P. Rogers, J. B. Edson, and G. S. Young, 1996: Bulk parameterization of air-sea fluxes for Tropical Ocean-Global Atmosphere Coupled-Ocean Atmosphere Response Experiment. *J. Geophys. Res.*, **101**, 3747, doi:10.1029/95JC03205.

- Fairall, C. W., E. F. Bradley, J. E. Hare, A. A. Grachev, and J. B. Edson, 2003: Bulk Parameterization of Air–Sea Fluxes: Updates and Verification for the COARE Algorithm. *J. Clim*, **16**, 571–591, doi:10.1175/1520-0442(2003)016<0571:BPOASF>2.0.CO;2.
- Fan, Y., I. Ginis, and T. Hara, 2009: The Effect of Wind–Wave–Current Interaction on Air–Sea Momentum Fluxes and Ocean Response in Tropical Cyclones. *J. Phys. Oceanogr*, **39**, 1019–1034, doi:10.1175/2008JPO4066.1.
- Flather, R. A., 1976: A tidal model of the northwest European continental shelf. *Mem. Soc. R. Sci. Liege, Vol. 10, No. 6. (1976)*, pp. 141–164, **10**, 141–164.
- Fowle, M. A., and P. J. Roebber, 2003: Short-Range (0–48 h) Numerical Prediction of Convective Occurrence, Mode, and Location. *Wea. Forecasting*, **18**, 782–794, doi:10.1175/1520-0434(2003)018<0782:SHNPOC>2.0.CO;2.
- Galarneau, T. J., Jr., C. A. Davis, and M. A. Shapiro, 2013: Intensification of Hurricane Sandy (2012) through Extratropical Warm Core Seclusion. *Monthly Weather Review*, **141**, 4296–4321, doi:10.1175/MWR-D-13-00181.1.
- Garratt, J. R., 1992: *The Atmospheric Boundary Layer*. Cambridge University Press.
- Gemmill, W., B. Katz, and X. Li, 2007: *Daily Real Time Global SST*. NOAA / NWS / NCEP / MMAB Office Note.
- Gentry, M. S., and G. M. Lackmann, 2009: Sensitivity of Simulated Tropical Cyclone Structure and Intensity to Horizontal Resolution. *Mon. Wea. Rev*, **138**, 688–704, doi:10.1175/2009MWR2976.1.
- Ginis, I., 2002: Tropical cyclone-ocean interactions. *Atmosphere-Ocean Interactions, Advances in Fluid Mechanics Series*, 83–114.
- Ginis, I., 1995: *Interaction of tropical cyclones with the ocean*. R.L. Elsberry, Ed. World Meteorological Organization, Geneva, Switzerland, 63 pp.
- Goerss, J. S., 2006: Prediction of tropical cyclone track forecast error for Hurricanes Katrina, Rita, and Wilma. *Amet. Meteor. Soc. Preprints, 27th Conf. on Hurricanes and Tropical Meteorology*.
- Gopalakrishnan, S. G., S. Goldenberg, T. Quirino, X. Zhang, F. Marks Jr., K.-S. Yeh, R. Atlas, and V. Tallapragada, 2012: Toward Improving High-Resolution Numerical Hurricane Forecasting: Influence of Model Horizontal Grid Resolution, Initialization, and Physics. *Wea. Forecasting*, **27**, 647–666, doi:10.1175/WAF-D-11-00055.1.

- Grell, G. A., J. Dudhia, and D. R. Stauffer, 1994: A description of the fifth-generation Penn State/NCAR mesoscale model (MM5). *NCAR Technical Note TN-398+STR*.
- Haidvogel, D. B., and Coauthors, 2008: Ocean forecasting in terrain-following coordinates: Formulation and skill assessment of the Regional Ocean Modeling System. *Journal of Computational Physics*, **227**, 3595–3624, doi:<http://dx.doi.org/10.1016/j.jcp.2007.06.016>.
- Hall, T. M., and A. H. Sobel, 2013: On the impact angle of Hurricane Sandy's New Jersey landfall. *Geophys. Res. Lett.*, **40**, 2312–2315, doi:10.1002/grl.50395.
- Halliwel, G. R., Jr., L. K. Shay, J. K. Brewster, and W. J. Teague, 2011: Evaluation and Sensitivity Analysis of an Ocean Model Response to Hurricane Ivan. *Monthly Weather Review*, **139**, 100802101247096, doi:10.1175/2010MWR3104.1.
- Hill, K. A., and G. M. Lackmann, 2009: Influence of Environmental Humidity on Tropical Cyclone Size. *Monthly Weather Review*, **137**, 3294–3315, doi:10.1175/2009MWR2679.1.
- Hodur, R. M., 1997: The Naval Research Laboratory's Coupled Ocean/Atmosphere Mesoscale Prediction System (COAMPS). *Monthly Weather Review*, **125**, 1414–1430, doi:10.1175/1520-0493(1997)125<1414:TNRLSC>2.0.CO;2.
- Hong, S.-Y., and J.-O. J. Lim, 2006: The WRF single-moment 6-class microphysics scheme (WSM6). *J. Korean Meteor. Soc.*, **42**, 129–151.
- Hyun, K. H., and R. He, 2010: Coastal upwelling in the South Atlantic Bight: A revisit of the 2003 cold event using long term observations and model hindcast solutions. *Journal of Marine Systems*, **83**, 1–13, doi:10.1016/j.jmarsys.2010.05.014.
- Jacob, R., J. Larson, and E. Ong, 2005: *M x N communication and parallel interpolation in CCSM using the Model Coupling Toolkit*. Argonne, IL.
- Jaimes, B., L. K. Shay, and G. R. Halliwel, 2011: The Response of Quasigeostrophic Oceanic Vortices to Tropical Cyclone Forcing. *J. Phys. Oceanogr.*, **41**, 1965–1985, doi:10.1175/JPO-D-11-06.1.
- Janjić, Z. I., 1990: The Step-Mountain Coordinate: Physical Package. *Monthly Weather Review*, **118**, 1429–1443, doi:10.1175/1520-0493(1990)118<1429:TSMCPP>2.0.CO;2.
- Janjić, Z. I., 1996: The surface layer in the NCEP Eta Model. *Eleventh Conference on Numerical Weather Prediction, American Meteorol Society*.
- Janjić, Z. I., 2002: Nonsingular implementation of the Mellor–Yamada level 2.5 scheme in the NCEP Meso model. *NCEP Office Note*, **437**, 61.

- Jones, P. W., 1999: First- and Second-Order Conservative Remapping Schemes for Grids in Spherical Coordinates. *Monthly Weather Review*, **127**, 2204–2210, doi:10.1175/1520-0493(1999)127<2204:FASOCR>2.0.CO;2.
- Kain, J. S., 2004: The Kain-Fritsch convective parameterization: an update. *Journal of Applied Meteorology*, **43**, 170–181.
- Khain, A., M. Frumin, I. Ginis, and A. Falkovich, 2000: Interaction of binary tropical cyclones in a coupled tropical cyclone-ocean model. *J. Geophys. Res.*, **105**, 22.
- Kirby, J. T., and T.-M. Chen, 1989: Surface waves on vertically sheared flows: Approximate dispersion relations. *J. Geophys. Res.*, **94**, 1013–1027, doi:10.1029/JC094iC01p01013.
- Komen, G. J., K. Hasselmann, and K. Hasselmann, 1984: On the Existence of a Fully Developed Wind-Sea Spectrum. *J. Phys. Oceanogr.*, **14**, 1271–1285, doi:10.1175/1520-0485(1984)014<1271:OTEAF>2.0.CO;2.
- Kumar, N., G. Voulgaris, J. C. Warner, and M. Olabarrieta, 2012: Implementation of the vortex force formalism in the coupled ocean-atmosphere-wave-sediment transport (COAWST) modeling system for inner shelf and surf zone applications. *Ocean Modelling*, **47**, 65–95, doi:10.1016/j.ocemod.2012.01.003.
- Kurihara, Y., 1973: A Scheme of Moist Convective Adjustment. *Monthly Weather Review*, **101**, 547–553, doi:10.1175/1520-0493(1973)101<0547:ASOMCA>2.3.CO;2.
- Kurihara, Y., and M. A. Bender, 1980: Use of a Movable Nested-Mesh Model for Tracking a Small Vortex. *Monthly Weather Review*, **108**, 1792–1809, doi:10.1175/1520-0493(1980)108<1792:UOAMNM>2.0.CO;2.
- Kurihara, Y., M. A. Bender, and R. J. Ross, 1993: An Initialization Scheme of Hurricane Models by Vortex Specification. *Monthly Weather Review*, **121**, 2030–2045, doi:10.1175/1520-0493(1993)121<2030:AISOHM>2.0.CO;2.
- Kurihara, Y., M. A. Bender, R. E. Tuleya, and R. J. Ross, 1995: Improvements in the GFDL Hurricane Prediction System. *Monthly Weather Review*, **123**, 2791–2801, doi:10.1175/1520-0493(1995)123<2791:IITGHP>2.0.CO;2.
- Kurihara, Y., R. E. Tuleya, and M. A. Bender, 1998: The GFDL Hurricane Prediction System and Its Performance in the 1995 Hurricane Season. *Monthly Weather Review*, **126**, 1306–1322, doi:10.1175/1520-0493(1998)126<1306:TGHPSA>2.0.CO;2.
- Lackmann, G. M., 2014: Hurricane Sandy before 1900, and after 2100. *Bull. Amer. Meteor. Soc.*, 140917143946002, doi:10.1175/BAMS-D-14-00123.1.

- Larson, J., R. Jacob, and E. Ong, 2004: *The Model Coupling Toolkit: A new Fortran90 toolkit for building multiphysics parallel coupled models*. Preprints, Mathematics and Computer Science Division, Argonne, IL.
- Lee, C.-Y., and S. S. Chen, 2012: Symmetric and Asymmetric Structures of Hurricane Boundary Layer in Coupled Atmosphere–Wave–Ocean Models and Observations. *J. Atmos. Sci.*, **69**, 3576–3594, doi:10.1175/JAS-D-12-046.1.
- Lee, C.-Y., and S. S. Chen, 2014: Stable Boundary Layer and Its Impact on Tropical Cyclone Structure in a Coupled Atmosphere–Ocean Model. *Monthly Weather Review*, **142**, 1927–1944, doi:10.1175/MWR-D-13-00122.1.
- Leipper, D., and D. Volgenau, 1972: Hurricane heat potential of the Gulf of Mexico. *J. Phys. Oceanogr.*, **2**, 218–224.
- Liu, B., C. GUAN, and L. Xie, 2008: Investigating the impacts of wave state and sea spray on typhoon via a coupled atmosphere-wave system: the idealized case. *28th Conference on Hurricanes and Tropical Meteorology*.
- Liu, B., C. Guan, L. Xie, and D. Zhao, 2012a: An investigation of the effects of wave state and sea spray on an idealized typhoon using an air-sea coupled modeling system. *Adv. Atmos. Sci.*, **29**, 391–406, doi:10.1007/s00376-011-1059-7.
- Liu, B., H. Liu, L. Xie, C. Guan, and D. Zhao, 2010: A Coupled Atmosphere–Wave–Ocean Modeling System: Simulation of the Intensity of an Idealized Tropical Cyclone. *Monthly Weather Review*, **139**, 100827132423068, doi:10.1175/2010MWR3396.1.
- Liu, L., J. Fei, X. Cheng, and X. Huang, 2012b: Effect of wind-current interaction on ocean response during Typhoon KAEMI (2006). *Sci. China Earth Sci.*, **56**, 418–433, doi:10.1007/s11430-012-4548-3.
- Ma, Z., J. Fei, L. Liu, X. Huang, and X. Cheng, 2013: Effects of the Cold Core Eddy on Tropical Cyclone Intensity and Structure under Idealized Air–Sea Interaction Conditions. *Monthly Weather Review*, **141**, 1285–1303, doi:10.1175/MWR-D-12-00123.1.
- Madsen, O. S., Y.-K. Poon, and H. C. Graber, 1988: Spectral wave attenuation by bottom friction: theory. *Coastal Engineering Proceedings*, **1**, doi:10.9753/icce.v21.
- Marchesiello, P., J. C. McWilliams, and A. Shchepetkin, 2001: Open boundary conditions for long-term integration of regional oceanic models. *Ocean Modelling*, **3**, 1–20, doi:10.1016/S1463-5003(00)00013-5.
- Marks, F. D., and L. K. Shay, 1998: Landfalling Tropical Cyclones: Forecast Problems and Associated Research Opportunities. *Bull. Am. Meteorol. Soc.*, **79**, 305–323, doi:10.1175/1520-0477(1998)079<0305:LTCFPA>2.0.CO;2.

- Mellor, G. L., and T. Yamada, 1974: A Hierarchy of Turbulence Closure Models for Planetary Boundary Layers. *J. Atmos. Sci*, **31**, 1791–1806, doi:10.1175/1520-0469(1974)031<1791:AHOTCM>2.0.CO;2.
- Mellor, G. L., and T. Yamada, 1982: Development of a turbulence closure model for geophysical fluid problems. *Rev. Geophys*, **20**, 851–875, doi:10.1029/RG020i004p00851.
- Merrill, R. T., 1984: A Comparison of Large and Small Tropical Cyclones. *Monthly Weather Review*, **112**, 1408–1418, doi:10.1175/1520-0493(1984)112<1408:ACOLAS>2.0.CO;2.
- Minobe, S., A. Kuwano-Yoshida, N. Komori, S.-P. Xie, and R. J. Small, 2008: Influence of the Gulf Stream on the troposphere. *Nature*, **452**, 206–209, doi:10.1038/nature06690.
- Minobe, S., M. Miyashita, A. Kuwano-Yoshida, H. Tokinaga, and S.-P. Xie, 2010: Atmospheric Response to the Gulf Stream: Seasonal Variations. *J. Clim*, **23**, 3699–3719, doi:10.1175/2010JCLI3359.1.
- Mitchell, D. A., W. J. Teague, E. Jarosz, and D. W. Wang, 2005: Observed currents over the outer continental shelf during Hurricane Ivan. *Geophys. Res. Lett*, **32**, L11610, doi:10.1029/2005GL023014.
- Mlawer, E. J., S. J. Taubman, P. D. Brown, M. J. Iacono, and S. A. Clough, 1997: Radiative transfer for inhomogeneous atmospheres: RRTM, a validated correlated-k model for the longwave. *J. Geophys. Res*, **102**, 16663, doi:10.1029/97JD00237.
- Molinari, J., and M. Dudek, 1992: Parameterization of Convective Precipitation in Mesoscale Numerical Models: A Critical Review. *Monthly Weather Review*, **120**, 326–344.
- Monin, A. S., and A. M. Obukhov, 1954: Basic laws of turbulent mixing in the surface layer of the atmosphere. *Contrib Geophys Inst Acad Sci USSR*.
- Moon, I., I. Ginis, and T. Hara, 2004a: Effect of surface waves on air–sea momentum exchange. Part II: Behavior of drag coefficient under tropical cyclones. *J. Atmos. Sci*, **61**, 2334–2348.
- Moon, I., I. Ginis, and T. Hara, 2004b: Effect of surface waves on Charnock coefficient under tropical cyclones. *J. Geophys. Res*, **31**, 20.
- Moon, I.-J., I. Ginis, T. Hara, and B. Thomas, 2007: A Physics-Based Parameterization of Air–Sea Momentum Flux at High Wind Speeds and Its Impact on Hurricane Intensity Predictions. *Monthly Weather Review*, **135**, 2869–2878, doi:10.1175/MWR3432.1.
- Morey, S., M. Bourassa, D. Dukhovskoy, and J. O'Brien, 2006: Modeling studies of the upper ocean response to a tropical cyclone. *Ocean Dynamics*, **56**, 594–606.

- Munsell, E. B., and F. Zhang, 2014: Prediction and uncertainty of Hurricane Sandy (2012) explored through a real-time cloud-permitting ensemble analysis and forecast system assimilating airborne Doppler radar observations. *J. Adv. Model. Earth Syst*, **6**, 38–58, doi:10.1002/2013MS000297.
- National Centers for Environmental Prediction, National Weather Service, NOAA, U.S. Department of Commerce, 2000: NCEP FNL Operational Model Global Tropospheric Analyses, continuing from July 1999. doi:10.5065/D6M043C6.
- Nelson, J., and R. He, 2012: Effect of the Gulf Stream on winter extratropical cyclone outbreaks. *Atmosph. Sci. Lett*, **13**, 311–316, doi:10.1002/asl.400.
- Oey, L. Y., T. Ezer, D. P. Wang, S. J. Fan, and X. Q. Yin, 2006: Loop Current warming by Hurricane Wilma. *Geophys. Res. Lett*, **33**, L08613, doi:10.1029/2006GL025873.
- Oey, L., T. Ezer, D. Wang, X. Yin, and S. Fan, 2007: Hurricane-induced motions and interaction with ocean currents. *Cont. Shelf Res*, **27**, 1249–1263.
- Okamoto, K., T. Iguchi, N. Takahashi, K. Iwanami, and T. Ushio, 2005: *The Global Satellite Mapping of Precipitation (GSMaP) Project*. 25th IGARSS Proceedings, 3 pp.
- Olabarrieta, M., J. C. Warner, and N. Kumar, 2011: Wave-current interaction in Willapa Bay. *J. Geophys. Res*, **116**, C12014, doi:10.1029/2011JC007387.
- Olabarrieta, M., J. C. Warner, B. Armstrong, J. B. Zambon, and R. He, 2012: Ocean–atmosphere dynamics during Hurricane Ida and Nor’Ida: An application of the coupled ocean–atmosphere–wave–sediment transport (COAWST) modeling system. *Ocean Modelling*, **43–44**, 112–137, doi:10.1016/j.ocemod.2011.12.008.
- Oost, W. A., G. J. Komen, C. M. J. Jacobs, and C. van Oort, 2002: New evidence for a relation between wind stress and wave age from measurements during ASGAMAGE. *Boundary-Layer Meteorology*, **103**, 409–438, doi:10.1023/A%3A1014913624535.
- Ooyama, K., 1969: Numerical Simulation of the Life Cycle of Tropical Cyclones. *J. Atmos. Sci*, **26**, 3–40, doi:10.1175/1520-0469(1969)026<0003:NSOTLC>2.0.CO;2.
- Pasch, R. J., E. S. Blake, H. D. Cobb III, and D. P. Roberts, 2006: *Tropical Cyclone Report Hurricane Wilma*. National Hurricane Center.
- Pollard, R. T., P. B. Rhines, and R. O. R. Y. Thompson, 1972: The deepening of the wind-Mixed layer. *Geophysical Fluid Dynamics*, **4**, 381–404, doi:10.1080/03091927208236105.
- Powell, M. D., P. J. Vickery, and T. A. Reinhold, 2003: Reduced drag coefficient for high wind speeds in tropical cyclones. *Nature*, **422**, 279–283.

- Powell, M. D., S. H. Houston, and T. A. Reinhold, 1996: Hurricane Andrew's Landfall in South Florida. Part I: Standardizing Measurements for Documentation of Surface Wind Fields. *Wea. Forecasting*, **11**, 304–328, doi:10.1175/1520-0434(1996)011<0304:HALISF>2.0.CO;2.
- Powell, M. D., S. H. Houston, L. R. Amat, and N. Morisseau-Leroy, 1998: The HRD real-time hurricane wind analysis system. *Journal of Wind Engineering and Industrial Aerodynamics*, **77-78**, 53–64, doi:10.1016/S0167-6105(98)00131-7.
- Prasad, T. G., and P. J. Hogan, 2007: Upper-ocean response to Hurricane Ivan in a 1/25° nested Gulf of Mexico HYCOM. *J. Geophys. Res.*, **112**, C04013, doi:10.1029/2006JC003695.
- Price, J., 1979: Observations of a rain-formed mixed layer. *J. Phys. Oceanogr.*, **9**, 643–649.
- Price, J., 1981: Upper ocean response to a hurricane. *J. Phys. Oceanogr.*, **11**, 153–175.
- Price, J., T. Sanford, and G. Forristall, 1994: Forced stage response to a moving hurricane. *J. Phys. Oceanogr.*, **24**, 233–260.
- Rheme, J. R., C. A. Sisko, and R. D. Knabb, 2006: On the calculation of vertical shear: An operational perspective. *Preprints: 27th Conference on Hurricanes and Tropical Meteorology*.
- Rogers, R., and Coauthors, 2006: The Intensity Forecasting Experiment: A NOAA Multiyear Field Program for Improving Tropical Cyclone Intensity Forecasts. *Bull. Am. Meteorol. Soc.*, **87**, 1523–1537, doi:10.1175/BAMS-87-11-1523.
- Shay, L. K., and Coauthors, 2008: *Air-Sea Interface and Oceanic Influences*. Seventh International Workshop on Tropical Cyclones, 48 pp.
- Shchepetkin, A. F., and J. C. McWilliams, 2005: The regional oceanic modeling system (ROMS): a split-explicit, free-surface, topography-following-coordinate oceanic model. *Ocean Modelling*, **9**, 347–404, doi:10.1016/j.ocemod.2004.08.002.
- Shen, B. W., M. DeMaria, J. L. F. Li, and S. Cheung, 2013: Genesis of Hurricane Sandy (2012) simulated with a global mesoscale model. *Geophys. Res. Lett.*, 4944–4950, doi:10.1002/grl.50934.
- Shen, W., and I. Ginis, 2003: Effects of surface heat flux-induced sea surface temperature changes on tropical cyclone intensity. *Geophys. Res. Lett.*, **30**, 1–4.
- Singh, R., P. Pal, C. Kishtawal, and P. Joshi, 2005: Impact of bogus vortex for track and intensity prediction of tropical cyclone. *J. Earth. Syst. Sci.*, **114**, 427–436.

- Skamarock, W. C., J. B. Klemp, J. Dudhia, D. O. Gill, X.-Y. Huang, and W. Wang, 2008: *A description of the Advanced Research WRF version 3*. 125 pp.
- Smith, G. B., 2012: Some insurance companies to Sandy victims: You are covered for hurricanes, not floods. *New York Daily News*, November 23, Local <http://www.nydailynews.com/new-york/insurers-sandy-victims-covered-hurricanes-floods-article-1.1206785>.
- Stewart, S. R., 2005: Tropical cyclone report—Hurricane Ivan 2-24 September 2004. *National Hurricane Center*.
- Taylor, P., and M. Yelland, 2001: The dependence of sea surface roughness on the height and steepness of the waves. *J. Phys. Oceanogr*, **31**, 572–590.
- Teague, W. J., E. Jarosz, D. Wang, and D. Mitchell, 2007: Observed Oceanic Response over the Upper Continental Slope and Outer Shelf during Hurricane Ivan. *J. Phys. Oceanogr*, **37**, 2181–2206.
- The Wamdi Group, 1988: The WAM Model—A Third Generation Ocean Wave Prediction Model. *J. Phys. Oceanogr*, **18**, 1775–1810, doi:10.1175/1520-0485(1988)018<1775:TWMTGO>2.0.CO;2.
- Tiedtke, M., 1989: A Comprehensive Mass Flux Scheme for Cumulus Parameterization in Large-Scale Models. *Monthly Weather Review*, **117**, 1779–1800, doi:10.1175/1520-0493(1989)117<1779:ACMFSF>2.0.CO;2.
- Tolman, H. L., 1991: A Third-Generation Model for Wind Waves on Slowly Varying, Unsteady, and Inhomogeneous Depths and Currents. *J. Phys. Oceanogr*, **21**, 782–797, doi:10.1175/1520-0485(1991)021<0782:ATGMFW>2.0.CO;2.
- Ushio, T., and Coauthors, 2009: GSMaP Passive Microwave Precipitation Retrieval Algorithm : Algorithm Description and Validation. *JMSJ*, **87A**, 119–136, doi:10.2151/jmsj.87A.119.
- Wada, A., M. F. Cronin, A. J. Sutton, Y. Kawai, and M. Ishii, 2013: Numerical simulations of oceanic pCO<sub>2</sub> variations and interactions between Typhoon Choi-wan (0914) and the ocean. *J. Geophys. Res. Oceans*, **118**, 2667–2684, doi:10.1002/jgrc.20203.
- Wada, A., N. Kohno, and Y. Kawai, 2010: Impact of Wave-Ocean Interaction on Typhoon Hai-Tang in 2005. *SOLA*, **6A**, 13–16, doi:10.2151/sola.6A-004.

- Wada, A., T. Uehara, and S. Ishizaki, 2014: Typhoon-induced sea surface cooling during the 2011 and 2012 typhoon seasons: observational evidence and numerical investigations of the sea surface cooling effect using typhoon simulations. *Prog Earth Planet Sci*, **64**, 3562–3578, doi:doi: 10.1175/JAS4051.1.
- Walker, N. D., R. R. Leben, and S. Balasubramanian, 2005: Hurricane-forced upwelling and chlorophyll a enhancement within cold-core cyclones in the Gulf of Mexico. *Geophys. Res. Lett*, **32**, L18610, doi:10.1029/2005GL023716.
- Wang, Y., and C. C. Wu, 2004: Current understanding of tropical cyclone structure and intensity changes - a review. *Meteorol Atmos Phys*, **87**, 257–278, doi:10.1007/s00703-003-0055-6.
- Warner, J. C., B. Armstrong, R. He, and J. B. Zambon, 2010: Development of a coupled ocean–atmosphere–wave–sediment transport (COAWST) modeling system. *Ocean Modelling*, **35**, 230–244.
- Warner, J. C., N. Perlin, and E. D. Skyllingstad, 2008: Using the Model Coupling Toolkit to couple earth system models. *Environmental Modelling & Software*, **23**, 1240–1249, doi:10.1016/j.envsoft.2008.03.002.
- Xie, L., B. Liu, H. Liu, and C. GUAN, 2010: Numerical simulation of tropical cyclone intensity using an air-sea-wave coupled prediction system. *Adv. Geosci*, **18**, 19–43.
- Xue, Z., J. Zambon, Z. Yao, Y. Liu, and R. He, 2014: An Integrated Ocean Circulation, Wave, Atmosphere and Marine Ecosystem Prediction System for the South Atlantic Bight and Gulf of Mexico. *Journal of Operational Oceanography*, 1–24.
- Yablonsky, R. M., and I. Ginis, 2009: Limitation of One-Dimensional Ocean Models for Coupled Hurricane–Ocean Model Forecasts. *Mon. Wea. Rev.*, **137**, 4410–4419, doi:10.1175/2009MWR2863.1.
- Zambon, J. B., 2009: An Examination of Tropical Cyclone Dynamics Utilizing the 3-Way Coupled Ocean Atmosphere Wave Sediment Transport (COAWST) Model. Masters Thesis – North Carolina State University, 140pp.
- Zambon, J. B., R. He, and J. C. Warner, 2014a: Investigation of hurricane Ivan using the coupled ocean–atmosphere–wave–sediment transport (COAWST) model. *Ocean Dynamics*, **64**, 1535–1554, doi:10.1007/s10236-014-0777-7.
- Zambon, J. B., R. He, and J. C. Warner, in press: Tropical to extratropical: Marine environmental changes associated with Superstorm Sandy prior to its landfall. *Geophys. Res. Lett.*